Thermoset State Estimation using Infrared Spectroscopy and Predictive Analytics

Vom Promotionsausschuss der
Technischen Universität Hamburg

zur Erlangung des akademischen Grades

Doktor-Ingenieur (Dr.-Ing.)

genehmigte Dissertation

von
Audrius Doblies

aus Girkaliai, Litauen

2023

Vorsitzender des Prüfungsausschusses:	Prof. Dr. rer. nat. Gerold Schneider (Technische Universität Hamburg)
Gutachter:	Prof. Dr.-Ing. habil. Bodo Fiedler (Technische Universität Hamburg) Prof. Daniel Hanoch Wagner (Weizmann Institute of Science, Israel)
Tag der mündlichen Prüfung:	31.08.2022

Technisch-Wissenschaftliche Schriftenreihe

Herausgeber:
Prof. Dr.-Ing. habil. Bodo Fiedler

Anschrift:
Technische Universität Hamburg
Institut für Kunststoffe und Verbundwerkstoffe
Denickestraße 15
21073 Hamburg

Band 43:
Thermoset State Estimation using Infrared Spectroscopy and Predictive Analytics

Name Audrius Doblies
1. Auflage
Hamburg 2023

ISSN 2625-6029

Bibliographische Information der Deutschen Nationalbibliothek: Die deutsche Nationalbibliothek verzeichnet diese Publikation in der Deutschen Nationalbibliothek; detaillierte Informationen sind im Internet über dnb.de abrufbar.

Acknowledgments

I would like to express my deep gratitude to my advisor Prof. Dr.-Ing. Habil. Bodo Fiedler, for his constant support and encouragement throughout my dissertation, while also allowing me the freedom to explore new concepts and pursue my ideas. Your expertise, patience, and willingness to provide constructive feedback and interest to discuss new concepts have been invaluable to the success of this research process.

I would like to express my sincere gratitude to the members of my dissertation committee, particularly to Prof. Daniel Hanoch Wagner, for his invaluable insights, constructive feedback, and thoughtful suggestions, which have significantly enhanced the quality of my dissertation. Additionally, I would like to thank Prof. Dr. rer. nat. Gerold Schneider for chairing the examination board.

I am deeply grateful to my family, friends and colleagues at the Institute of Polymer and Composites for their unwavering support, encouragement, and understanding. Thank you for listening to wild ideas and discussing abstract theories, special thanks to Christina Buggisch, Benjamin Boll, Dennis Gibhardt, Sergej Harder, Johann Körbelin, Sven Drücker, Valea Wisniewski, Tim Würger, and Robert Meißner. Your honest words, patience, and unwavering belief in me have been a source of motivation and inspiration.

Finally, I would like to express my gratitude to all students who took part in this study, especially Eduard Schill, Theresa Kettner, Lennart Braun, Hendrik Wilhelm Rose and Phil Röttger. Without your willingness to support my research and share your experiences, this dissertation would not have been possible. I would like to thank the German Research Foundation (DFG) for funding my research activities in the project “Evaluation and modelling of the fatigue damage behaviour of polymer composites at reversed cyclic loading” (project number 281870175).

Abstract

By design fiber-reinforced plastics (FRP) show extraordinary specific strength and stiffness performance when compared to classic structural materials. Unfortunately, the extraordinary properties come at the price of complexity in design, manufacturing and operation. Most notably, manifold failure modes and complicated detectability of inherent damages represent a challenge for composite engineers until now. Throughout the life-cycle of composites, it is crucial to understand and track the material state in order to prevent premature failure. Due to the high-cost sensitivity of the composites sector implementing material health monitoring systems is usually not practical in application. Instead, non-destructive testing (NDT) methods are usually applied to assure structural integrity and damages within allowed limitations at planned maintenance events. Nonetheless, currently available NDT methods are insufficient to fully cover all possible damage scenarios. In this work a new approach to determine material properties of the epoxy resin component using Fourier-transform infrared spectroscopy (FTIR)-spectroscopy is presented. It is shown that by post-processing the acquired molecular information the material state can be determined and based on this material state inherent material properties such as strength can be predicted. First, starting with the evaluation of manufacturing parameters it is shown that by using classic chemometrics techniques FTIR measurements can be used to quantify the mixing ratio of an epoxy resin fast and reliable. Thereafter, material changes due to mechanical loading in creep are observed and described by applying advanced feature extraction methods. Finally, specimens exposed to thermal loads are analyzed and it is confirmed, that the residual strength can be determined solely by applying FTIR measurements and machine learning algorithms. Furthermore, it is demonstrated, that the method is suitable to reveal the material exposure history. It is shown that an accurate prediction of mechanical properties, as well as the processing and degradation parameters, can be derived from the measurements and significantly improved by applying data processing and machine learning methods.

Kurzfassung

Im Vergleich zu klassischen Konstruktionsmaterialien zeigen faserverstärkte Verbundwerkstoffe hohe spezifische Festigkeiten und Steifigkeiten auf. Als Nachteilig müssen hingegen die komplexen Versagensmechanismen und eine hohe Anfälligkeit für unentdeckte Schäden betrachtet werden die bei diesen Werkstoffen beobachtet werden. Während des gesamten Lebenszyklus von Verbundwerkstoffen ist es daher entscheidend, den Materialzustand einzuschätzen und verfolgen zu können, um ein frühzeitiges Versagen zu verhindern. Aufgrund der hohen Kostensensitivität von Verbundwerkstoffanwendungen ist die Implementierung eines kontinuierlichen Systems zur Bauteilüberwachung in der Regel nicht praktikabel. Vielmehr ist es üblich zerstörungsfreie Prüfungen in regelmäßigen Intervallen auszuführen, um die strukturelle Integrität sicherzustellen. Die derzeit verfügbaren zerstörungsfreie Prüfmethoden reichen jedoch nicht aus, um alle möglichen Schadensszenarien vollständig abzudecken. In dieser Arbeit wird ein neuer Ansatz zur Bestimmung der Materialeigenschaften der Epoxidharzkomponente mittels Fourier-Transformations-Infrarotspektroskopie (FTIR) -Spektroskopie vorgestellt. Durch die Nachbearbeitung der erfassten molekularen Informationen wird der Materialzustand auf Basis abstrakter Parameter modelliert und die inhärente Materialeigenschaften wie Festigkeit berechnet und vorhergesagt. Zunächst wird anhand von Herstellungsparameter gezeigt, dass mithilfe klassischer chemometrischer Methoden und FTIR-Messungen das Mischungsverhältnis eines Epoxidharzes schnell und zuverlässig bestimmt werden kann. In einem zweiten Schritt werden Materialänderungen aufgrund mechanischer Belastung beim Kriechen beobachtet und mit Hilfe des abgeleiteten Zustandvectors beschrieben, wobei fortschrittliche Verfahren zur Merkmalsextraktion angewendet werden. Schließlich werden Proben analysiert, die thermischen Belastungen ausgesetzt wurden, wobei gezeigt werden konnte, dass die Restfestigkeit ausschließlich durch die Anwendung von FTIR-Messungen in Kombination mit Algorithmen des maschinelles Lernen bestimmt werden kann. Weiterhin wird gezeigt, dass gleichzeitig auch eine genaue Beschreibung der Historie der Materialdegrada-

tion aufgedeckt werden kann. Zusammenfassen wird gezeigt, dass eine genaue Vorhersage der mechanischen Eigenschaften sowie der Verarbeitungs- und Schädigungsparameter aus FTIR Messungen erfolgen kann und durch die Anwendung von Datenverarbeitungs- und maschinellen Lernmethoden eine signifikante Verbesserung der Genauigkeit erzielt werden kann.

Contents

List of Abbreviations

ANN	Artificial neural network
AP	Application path
CFRP	Carbon-fibre reinforced polymer
CP	Chemical processes
DMA	Dynamic mechanical analysis
DSC	Differential scanning calorimetry
FE	Feature extraction
FTIR	Fourier-transform infrared spectroscopy
FRP	Fibre-reinforced polymer
LR	Linear regression
MIRS	Mid-field infrared spectroscopy
ML	Machine learning
MP	Modeling path
NC	Non-constricted
NDT	Non-destructive testing
NIRS	Near field infrared spectroscopy
nMAE	Normalized mean absolute error
PC	Principal component
PCA	Principal component analysis
PCR	Principal component regression
PLS	Partial least squares
PP	Pre-processing
PWN	Peak wavenumber
rH	Relative humidity
SAA	Standard Ambient Atmosphere
SHM	Structural health monitoring
SNR	Signal-to-noise ratio
TD	Thermal degradation
Tg	Glass transition temperature
Tga	Thermal gravimetric analysis
TSP	Thermosetting polymers
UTS	Ultimate tensile strength
WAXS	wide angle X-Ray scattering

1 Introduction

1.1 Motivation

The idea of joining different substituents and forming new artificial composite materials is now established for more than 70 years. By utilizing the advantageous individual properties of each substituent and circumventing their drawbacks by tailored design, superior materials have been created in the past. In the area of fiber-reinforced plastics (FRP), this approach is backed by the wide availability of different fibers and polymeric matrices, enabling a wide range of possible characteristics. Hence, it is no surprise that the quantity and variety of composite structures in the industry, especially in the aviation and wind-energy sectors, continuously increased over the past decades.

Design Approach in the Past

In addition to freedom in material choice, composites also opened a new way of considering multiple scales in design. Composites inherently come with multiple length scales, which contributes to higher overall material performance. However, it quickly became evident that the improved performance of the new complex composite material class comes with a price tag. Especially in comparison to single-phase materials, the traceability of the damage evolution and distribution became considerably more complicated. At the same time, accurate prediction of failure and residual load-bearing capability turned out to be more challenging. The reason for this behavior can be mainly seen in the highly interactive multi-dimensional damage evolution processes, which are not yet sufficiently understood.

In the early days of composite applications, it was sufficient to apply simple design methods to achieve substantial performance gains and surpass single-phase materials in terms of performance. Defining conservative load-bearing limits by experience and applying large safety margins based on phenomenological observations yielded reliable and sufficient lightweight structures. Over the last decades, extensive experience in design and manufacturing led to an increase in

knowledge in the composite area. Along with this development, a shift toward more sophisticated statistics-based design methods was performed. The initial phenomenologically defined load-bearing limitations have been replaced by probabilistic models based on statistical material property distributions taking the inherently large scatter into account. Significant efforts in testing have been undertaken in the past to understand and quantify all relevant influence factors, loading conditions and damage interactions to ensure a safe design. In service, past experience has shown that even if a full record of the loading and exposure history is available for a composite component, the ultimate load-bearing capabilities and true safety margins still cannot be determined with high accuracy and certainty. As a consequence, the full potential of composite materials is not yet fully utilized due to safety concerns arising from the lack of true material state knowledge.

Material State Estimation in the Past

A considerable amount of methods were proposed to understand and track material variation in the design phase and operation to cover the shortcomings described in the last section. The methods can be divided into two groups: structural health monitoring (SHM) and non-destructive testing (NDT), which have been proposed to keep track of potential material changes. However, currently available methods are limited to specific damage cases and are costly, time-consuming or not applicable on a large scale. Indeed, tracking and evaluating the material state for a large-scale composite structure based upon unknown damage history is still neither established nor feasible due to the lack of generalization of the methods.

This study builds on the observations that initial damage modes in composites are dominated by polymeric matrices with few exceptions. Due to their extraordinary performance, beneficial costs and ease of manufacturing, thermosetting polymers (TSP) are mainly used as polymeric matrices in high-performance composite applications. Even though TSP's macroscopic behavior is nowadays well understood under a variety of loading and environmental conditions, the underlying physical and chemical processes are not yet fully disclosed. Nonetheless, to explain the origin of the previously described stochastic variation in damage evolution and material property variation, there is a need to understand these processes.

Ideally, the material state, material changes and degradation processes shall be explained based on the evaluation of information from all length scales using ro-

bust data. The downside of currently applied methods to gather information is that they are often based on complex experimental setups with many limitations. As a result, there is little agreement on the broad applicability and validity of data derived in such a manner in practice. The following section presents an approach to resolve all these challenges.

1.2 Aims and Scope

A novel concept to establish a direct link between material state and material properties by using data analytic and machine learning algorithms is introduced in this work. Undoubtedly, macroscopic material properties such as strength and stiffness are linked with the physical and chemical configuration of the material on multiple scales. The main idea of this work is to use advanced data processing tools to derive an abstract material state vector directly from the molecular level using a non-destructive, contact-less technique called Fourier-transform infrared spectroscopy (FTIR). FTIR is well established in science and industry to acquire information on chemical bonds and molecular groups. So far, this method has mainly been used to solve isolated problems where mostly single material parameters have been observed and analyzed.
In this study, the feasibility of obtaining a material state vector that is generalizing and considering all material parameters is evaluated. It builds on the hypothesis that infrared spectral data inherently contains information that has not been considered in the classic infrared spectroscopy data analysis. The discovery and processing of this additional information shall provide a full insight into the material state of the analyzed TSP. It is further assumed that the derived data contains historical material-dependent information, such as manufacturing, ambient exposure, and degradation processes. In this work, mainly material changes in the damage initiation stage on the molecular and microscopic levels are considered. Macroscopic material changes, such as extended fracture regions or delaminations as seen in composites are not considered.
The biggest advantage of this approach over the classic NDT methods lays within the fact that the material state (See Section 2.1.1) is solely derived from the molecular and microscopic structure of the material without the necessity to add information from macroscopic observations.

The alleged limitation that spectral data is acquired on the molecular scale and may not be suitable to derive macroscopic properties is accounted for as follows.

First, in FTIR, large material volumes and numbers of molecules are measured, where a cumulative and averaged data vector is acquired from each analysis. Second, to ensure generalization, time and spatially resolved measurements can be performed to increase the sample size. Hence, by performing multiple measurements, statistically significant sampling is assured for larger specimens or components.

Another advantage of this method is that using this approach, depth profiling of a larger specimen can be performed if cross-sections are extracted and time and specimen thickness-dependent variation can be analyzed. Assuming the TSP can be regarded as isolated from the composite material, smaller specimens can be used in situ to observe material changes and their impact on material properties in real-time with a significant reduction of time and costs. Using the proposed approach also allows for separating the influence factors that affect the performance of TSP and reassembling them as desired. For each influence factor, a correlation between the infrared spectra and material properties can then be established. As a result, material properties such as the mechanical load-bearing capabilities can be predicted by considering all influence factors. Ideally, every possible influence factor and the contribution toward the damage developing shall be identified.

Data Processing and Machine Learning

Early FTIR devices had the limitations that only trained personnel were able to perform measurements, while the size of the devices restricted their use to laboratory environments. Recent developments in the field of Fourier-transform infrared spectrometers led to the wide availability of compact and relatively cheap devices. Nonetheless, these industry grade devices are still only capable of providing relatively low data quality and rather inaccurate measurements. As will be shown later, looking at the molecular bonds responsible for the material state estimation, the spectral variation is relatively small, highly scattered and few research sources are available for accurate identification. To be able to extract accurate material state information, the data has to be further processed, what will be done in this work using learning methods. Different algorithms are evaluated to improve the reliability of the prediction and establish a link between the IR spectra and material properties. One major drawback of machine learning models, especially the artificial neural networks (ANN), is the lack of prediction stability if unexpected influences have an impact on the measurement or the

material state. Therefore, in this work, a new approach is proposed to increase the robustness of the measurement, data processing and prediction quality.
The following data processing modules are used in this work to form the full workflow. First, data pre-processing such as outlier detection, can be performed to increase the spectral data quality, e.g., by detecting and deleting measurements provably containing errors using principal component analysis (PCA) algorithms.
Second, machine learning (ML) methods can be used to identify relevant spectral areas and dependencies between measured spectra and material state parameters. Indeed, this approach allows a statement regarding the feasibility of identifying and extracting underlying correlations. For example, it enables identifying the contribution of each molecular bond toward material parameter variations and defining relevant spectral areas to quantify the observed problem.
Finally, the ultimate goal is to create a robust data pipeline where the disclosed dependencies are implemented into an analytical model connecting the FTIR measurement and desired material property.

Research Objective

This work's objective is to evaluate the feasibility and limits of state estimation of thermosetting polymers by infrared spectroscopy. A link between the material state, its mechanical properties and its infrared spectrum throughout the lifecycle shall be established. To achieve this target, a trade-off study considering testing effort, acquisition techniques and advanced data treatment methods is performed. The core of the thesis is represented in Figure 1.1, while the major four questions of the thesis are stated below:

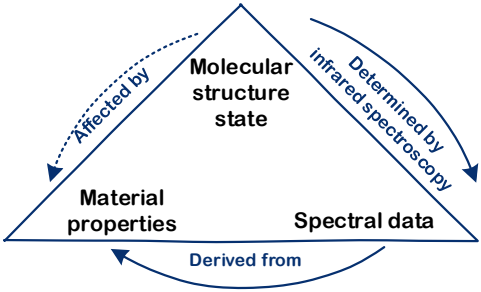

Figure 1.1: Interaction and dependencies information flow chart

Major questions

- Which material state variation can be detected using infrared spectroscopy and what is the sensitivity in each case?
- Is it possible to explain mechanical property changes on the molecular level?
- Is it possible to establish a model to predict mechanical properties based on infrared spectroscopy?
- How can advanced data processing be applied to increase the accuracy of the out-of-sample prediction?

2 Scientific and technological background

In the following section, a brief overview of the most relevant scientific and technological topics is given to provide a solid background for this thesis.A more detailed background and literature review regarding the single scientific content is given at the beginning of each corresponding section. Here, a focus on shared subjects is laid, starting with an explanation of the material state term, followed by the degradation definition and finalized by a brief explanation of the infrared spectroscopy technique.

2.1 Material State

2.1.1 Material State Definition

Depending on the area of research, each scientist may have a different definition and idea of the term material state. Hence an explicit definition of this term is given here to clarify what is meant by this term throughout this work.
The term material state refers to a collection of inner variables characterizing a specific material condition capable of describing the expected material behavior fully. Depending on the model complexity and model goal, a single numerical entry or a numerical vector may represent the material state. In this work, the term material state will be used as substitutional for both of these types. This material state then defines unambiguously the expected material behavior under certain loading conditions. In fact, the material state shall be used to determine macroscopic material properties, such as load-bearing capabilities for specific external inputs. In practice, the material state vector complexity will be limited to the required size. Even though, in the future it is desirable to cover all influence factors with a single material state, the required data to achieve such a representation was not available in this work, highlighting the conceptual nature of this work. Nonetheless, the results from the different sections are regarded as interchangeable and summable.

To obtain material state variables, non-destructive testing (NDT) and mechanical testing are usually carried out. Until now, the challenge remains to choose the correct method and scale to determine all required inner variables to define the material state. As will be shown later, a wide variety of NDT methods is nowadays available to determine isolated inner variables to describe specific TSP properties. However, a single generalizing approach to fully characterize the material state is still unknown. Deriving material states from mechanical testing is usually undesired due to expected statistical scatter, the destructive character of testing and influences from the inhomogeneity of the tested specimen.
In this work, the approach is undertaken to show the capability of infrared spectroscopy to serve as the base to derive a reliable material state. Different shapes and abstraction levels of material states will be implemented throughout the work. Within Section 5, the material state is represented by a measurable numerical value. In Section 6, derived parameters represent the material state. Finally, in Section 7, an abstract concept is used where the material state is represented by a neural network model.

2.1.2 The Origin of Material State Information

The base idea behind using IR for state estimation is to quantify the material state on the molecular scale while tracking the damage evolution on the macroscopic scale. It is well known that a TSP consists of atoms and molecules forming a three-dimensional molecular network. The nature and amount of molecular bonds on the atomic scale govern the molecular arrangement and therefore, the molecular forces. During the damage evolution, the behavior and processes of these molecular forces are currently not well understood and an object of research. However, the macroscopic properties visible on the macroscopic scale are doubtless in a strict relationship with these forces, which can be described using infrared spectroscopy. The absorption signal of the infrared spectroscopy represents an integral value of the single atomic bonds. Hence, even though the IR measurements represent molecular scale data, they give access to the statistical distribution and homogenized material data of these molecular bonds for the considered material volume.

2.2 Degradation

2.2.1 Degradation - Aging – State Variation

A sheer endless number of processes occurring during the life-cycle of composites have an effect on the mechanical properties of the material. The DIN 50035 standard introduces the term “aging” as the umbrella term for all irreversible physical and chemical processes in a material that leads to a variation of the material state [1]. The origin of the variation may be internal, e.g., conditioned by a metastable state or external, caused by influence factors in general. The term aging is used ambiguous but is mainly connected with the decrease in the performance of a material or component. Whereas, according to the standard, the term aging describes a material property variation that may be negative but can also be of positive nature. Therefore, instead of using the word aging, the term state variation is chosen in this thesis to describe changes in properties in general. In fact, the state variation can be of chemical or physical nature, reversible or irreversible, with a positive or negative influence on material properties. The term degradation, on the other hand, is used to describe state variations that lead to a negative impact on material property values. For instance, when a material is stated to degrade, a reduction of strength or stiffness is expected.

2.2.2 Degradation Factors

Usually, the degradation processes themselves are not clearly disclosed, but rather the effects of these processes are detectable and visible. Overall, one can distinguish between fast and continuous processes that have to be analyzed differently. The degradation process can take place almost immediately if a specific condition is met. For example, looking into thermal degradation, a specific temperature may trigger molecular disintegration by bond dissociation. On the contrary, continuous, relatively slow processes may set on from the moment a specific condition is met, where a change in TSP properties evolves continuously over time. One example of such a slow process is the absorption of moisture. Most external and internal influence factors acting on the TSPs are capable of varying the material state and therefore, material properties. The main question, which has to be answered for every material and material combination is the time or intensity-dependent threshold and the severity of the state variation. Therefore, to understand the impact and interaction of a single process, ideally, all influence factors shall be considered. Figure 2.1 shows a brief summary of

the major influence factors acting on a TSP considered exemplary in this work. The severity of the degradation is highly material and material state-dependent. In composites, while the fibers are usually resistant to most external influence factors, the matrix is highly susceptible to undergo a change in the material state and therefore, usually represents the weak link. A review of the impact of the factors shown in Figure 2.1 for the TSPs used in this work will be provided in the literature review of each corresponding Section [2].

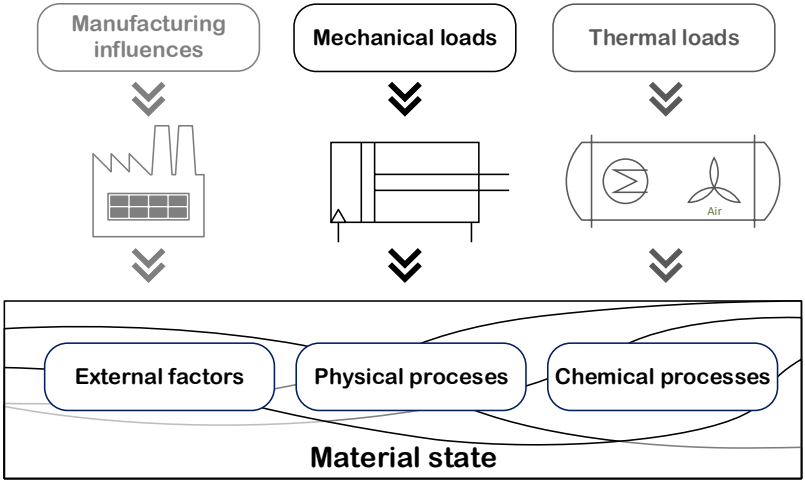

Figure 2.1: Overview of the material state influence factors considered in this work

2.3 Material State Estimation Techniques

Understanding TSP damage evolution and its impact on mechanical properties is the key to further improvement of the durability and performance of composite materials. In order to understand the material degradation evolution, one should ideally observe the changes in the material state as accurately as possible. This is the task of NDT and SHM. The use of SHM is based on continuous anomaly detection and data correlation with previously created material and data models assuring operation within known limitations. While several approaches have been shown in the past to work in a lab environment, there is no known reliable method implemented into a primary structure until now. A key problem remains

the overall low technology readiness level, costs and the transferability of the methods from simple geometries to complex real components. In contrast to the continuous approach, non-destructive testing at discrete points in time represents a valid alternative. Based on the physical principle, the different techniques can be divided into three categories, namely electrical methods, mechanical waves and electromagnetic waves. The latter will be used in this work and will be explained in more detail next. To show the current state of electromagnetic wave techniques, the most important developments and methods will be presented.

2.3.1 Electromagnetic Waves

Depending on the emitting source, electromagnetic waves can be regarded as a stream of light quants at different frequencies, respectively energies. An electromagnetic wave travels with the speed of light in a vacuum and can be considered a coupled electrical and magnetic field. In general, electromagnetic waves ranging from gamma rays to radio waves can be considered for NDT due to the advantage of being capable of propagating independently from the medium. The choice of the electromagnetic band is highly dependent on the desired material interaction. For spectroscopic applications, the wavenumber is used to quantify the energy of the quants and correlate this energy with the interacting processes of the material. The wavenumber is calculated by the number of waves per centimeter and is the reciprocal of the wavelength in cm [3]. For NDT applications, different wavelengths have been used so far. As a general rule, it can be stated that a higher radiation frequency is capable of penetrating a higher depth of material. For applications in the area of TSPs and composites, the highest penetration depth can be achieved using X-Ray waves. This method was used in the past extensively to unveil the structure of a material by transmission or diffraction. Most recently, a study by Trappe has shown that a special X-Ray method called small-angle X-ray scattering (SAXS) can be used to characterize composite structures in terms of inter-fiber failure and microcrack formation [4, 5]. Other studies used wide-angle X-Ray scattering (WAXS) on the atomic scale to quantify the molecular orientation of polymers [6]. Even though these methods are capable of revealing structural information, they are not suitable to be applied as a holistic NDT method in practice due to the limited scope of the results.

In contrast to X-Ray wave-based methods, which can be considered passive methods with respect to material interaction, the infrared band-based methods allow

a characterization by an active interaction of the electromagnetic waves with the material. Another advantage is that a significantly higher information density can be achieved. In the infrared band, two methods that are widely applied are infrared and Raman spectroscopy. Infrared spectroscopy is based on the change of the dipole moment of chemical bonds, while Raman spectroscopy uses the effect of Raman scattering based on polarization [3]. Several studies have shown that both techniques are suitable to answer a variety of questions with respect to polymer characterization [7]. The reason IR spectroscopy was chosen over Raman spectroscopy for this study is its advantage of superior sensitivity, as will be explained next.

2.3.2 Fourier-transform Infrared Spectroscopy

In this section, a brief introduction to the basics of Fourier-transform infrared (FTIR) spectroscopy is given. For more details and information on specific topics, the following two books are highly recommended [3, 8]. A wide variety of topics regarding the practical application of FTIR spectroscopy can also be found in the FTIR talk letters published by Shimadzu [9]. Traditionally, FTIR was used in chemistry and material science to identify and quantify molecular species [10]. It is a sensitive, easy-to-use and fast data acquisition technique widely used in industrial and scientific applications. With rising accuracy and decreasing costs, FTIR became a widely used technique in chemical process control, medicine and material science [11, 12]. The introduction of chemometrics combined with near-infrared (NIR) spectroscopy enabled a variety of new applications by reducing the complexity of utilization [13]. With fast-progressing research in the area of machine learning, great success was achieved in medical diagnosis, e.g., by detection and classification of cancer cells [14–16]. An extensive topic-focused literature review of applications in the area of composites and polymers will be provided in the corresponding sections of this work.

Physical Basics

FTIR is based on the absorption of light at discrete energies by organic material in the infrared region. One can distinguish between the NIR spectral region, which ranges from 0.78 µm to 3 µm and the mid-infrared (MIR) spectral region from 3 to 50 µm [17]. In these regions, infrared radiation is capable of

exciting molecular vibrations by absorption of single light quants of discrete energy. Through the measurement of the absorption intensity in a wide range of the infrared region, the corresponding absorbing molecular bonds can be identified and further analyzed. Infrared spectroscopy is a three-step process based on the emission of broadband electromagnetic radiation in the infrared region, transmission through a medium and measurement by a detector, as shown in Figure 2.2. Based on the molecular composition of the analyzed medium, the FTIR spectrometer measures the difference between the emitted and detected spectrum, quantifies the light quants absorbed by the specimen and calculates its FTIR spectrum.

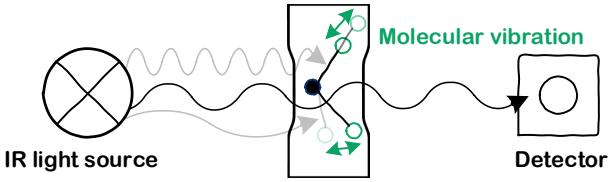

Figure 2.2: Infrared spectroscopy scheme

As a result, the chemical composition is represented by a specific absorption spectrum comprised of different absorption intensities at discrete energies. Generally, the absorption of light quants goes along with the change of the dipole moment of the bonds leading to energetic excitation and a specific vibration or rotation mode depending on the energy level. The time a molecular bond remains in the excited state is usually very short, allowing multiple measurements without influencing material properties [8]. Only discrete amounts of energy represented by different wavelengths can induce the described excitation process. These wavelengths depend on molecular bond properties such as bond stiffness, atomic mass, geometric considerations and interaction between neighboring bonds. The shape of the single peak is governed by the chemical environment of the bonds [3]. Two main classes of excited vibration modes exist, which are stretching vibrations, where the bond length is changed and bending vibrations, where the angle of the bonds is variated. A detailed description of the vibration modes can be found in the literature [3, 8]. In infrared spectroscopy, it was established to

use wavenumbers instead of frequencies. The wavenumber of a specific frequency is defined as the number of waves that can be fitted into 1 cm.

Quantitative FTIR Analysis

Quantitative measurement of the molecular species can be performed by applying the Lambert-Beer-Law. It describes a relationship between the concentration of a molecular bond in the beam path and the absorbance signal at the detector, assuming linear correlation [3]. A maximum thickness limitation is set by non-linearities occurring at absorbance values higher than 0.7 or transmittance values of less than 20 % [3]. These limits are defined based on experience and originate from stray radiation, insufficient resolution or chemical reaction during measurement [8]. To comply with these requirements, the specimen thickness for mid-infrared spectroscopy (MIRS) measurements with current devices is usually ranging between 5 and 50 µm dependent on the analyzed material and the wavenumber which is studied. For near-infrared spectroscopy (NIRS), the specimen thickness is usually found to be 0.1 to 5 mm. The thickness requirements are set by the intensity of the signal and the signal-to-noise ratio (SNR). Hence, the specimen has to be thick enough to generate a signal of sufficient intensity with low noise while allowing sufficient penetration by not absorbing the full intensity. In practice, the choice of the method between MIR and NIR spectroscopy is represented by a trade-off between specimen preparation effort and feasibility and information density. While NIRS specimens require less specimen preparation, their measurements yield lower information density. The second trade-off in infrared spectroscopy is represented by SNR, spectral resolution and measuring time. The signal-to-noise ratio depends on several parameters, such as light source intensity, sensor detectivity and the velocity of the mirror of the interferometer [8]. The spectral resolution determines the number of discrete values which form the single peaks. A higher resolution generally leads to sharper spectra but also a lower SNR ratio and higher acquisition times. Temperature and moisture usually have a high impact on FTIR measurements. Nonetheless, in this work, the influence of moisture and temperature was avoided by storing the specimens for at least 14 days, as well as performing the tests under a standard atmosphere at 23 °C and 50 % relative humidity.

3 Materials and Methods

The materials and methods used in this work are introduced in the present section. First, both TSPs and their components are presented, followed by the corresponding manufacturing processes. In the second part, the methods used throughout this work to acquire data for the analysis are given. For each technique, the data acquisition process is explained and basic material characterization is performed where the base material properties are given for the reference material state.

3.1 Materials and processes

3.1.1 Used Thermoset Systems

The analyzed TSPs are formed by the reaction of an epoxy resin which contains reactive epoxy groups with a curing agent component leading to a chemical reaction and formation of a three-dimensional cross-linked network.

The base component of the TSPs is usually based on di-glycidyl ether of bisphenol-A (See Fig. 3.1). The molecular weight parameter n is usually varied in terms of magnitude and distribution to set the desired viscosity for optimized processability and polymer network density. The choice of the curing agent represents the second setscrew. To conduct most experiments, mainly an amine-based curing agent is used in this work. For comparison reasons, a second anhydride-based curing agent is introduced in several sections where a curing agent variation plays a major role in the experimental setup.

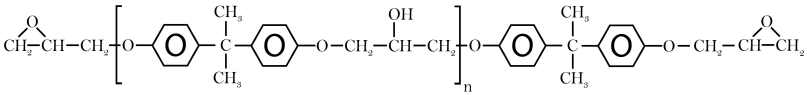

Figure 3.1: Di-glycidyl ether of bisphenol-A

The two-component amine-cured system consisting of RIMR135^{TM} /RIMH137^{TM} is a low-viscosity resin system designed for wind energy applications curing at ambient conditions. This thermosetting polymer based on the amine-cured epoxy system will be called RIM or RIM-system throughout the work. It mainly consists of a standard di-glycidyl ether of bisphenol-A (DGEBA) type epoxy resin and a reactive diluent 1,6-bis(2,3-epoxypropoxy)hexane and has an epoxide equivalent weight (EEW) of 166-185 g/eq. (RIMR135^{TM} - Hexion, International: USA/Europe). The curing agent consists of aliphatic amines, such as poly(propylether amine) (AHEW = 52 g mol-1) and isophorone diamine (RIMH137^{TM} - Hexion, International: USA/Europe). In compliance with the technical data sheet, a mixing ratio of (RIMR135/RIMH137) 100:30 was applied.

The three-component anhydride-cured system consisting of LY556/HY917/DY070 is a low-viscosity, long pot life resin system designed for filament winding or pultrusion cured at elevated temperatures. This thermosetting polymer based on the anhydride cured epoxy system will be called LY or LY-system throughout the work. It consists of a standard di-glycidyl ether of bisphenol-A (DGEBA) type epoxy resin (Araldite LY 556 (Huntsman Advanced Materials, Belgium)) with an epoxide equivalent weight (EEW) of 183-192 g/eq. The curing agent is a tetra functional anhydride curing agent with an anhydride equivalent weight of 166 g/eq supplied by Huntsman Advanced Materials, Belgium. In addition, an imidazole accelerator DY070 (Huntsman Advanced Materials, Belgium) is added. According to the datasheet, the standard mixing ratio of (LY556/HY917/DY070) 100:90:1 was used. The chemical structure of the major components of both epoxy systems can be found in [18].

3.1.2 Curing and Post-curing

All manufacturing and analysis tasks have been performed in the labs of the Hamburg University of Technology (TUHH) at the Institute of Polymers and Composites. For both epoxy systems, a standard manufacturing RTM process was applied.

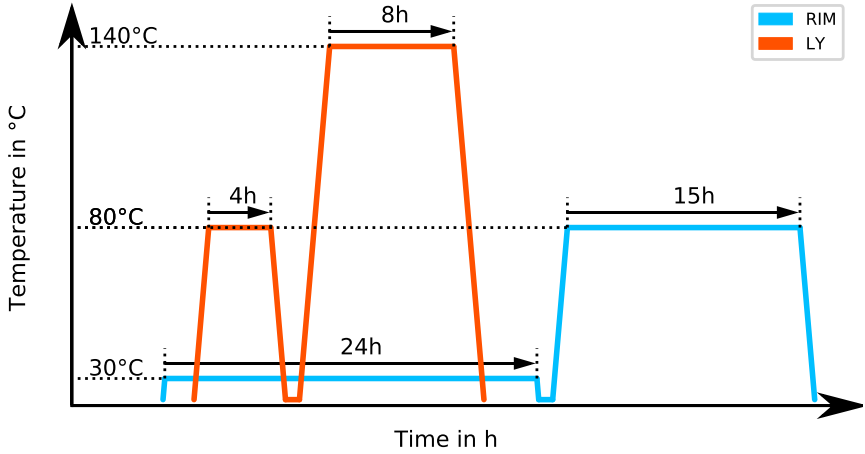

Figure 3.2: Curing cycles for the LY-system in orange and RIM-system in blue

The components were mixed and degassed in a vacuum stirrer, followed by a vacuum infusion process. The RIM-system was cured at 30 °C for 24 h and post-cured for 15 h at 80 °C in compliance with the datasheet. The LY-system was cured at 80 °C for 4 h and post-cured for 8 h at 140 °C. The post-curing process took place after demolding from the RTM mold according to industry standards in a temperature-controlled convection oven. All cooldown processes have been performed at a cooling rate of 0.5 °C / min or less for both configurations. The manufacturing processes for the RIM-system and LY-system are illustrated in Figure 3.2.

3.1.3 Specimen Preparation

The manufacturing process yielded a high surface quality 300 mm * 600 mm * 0.5 mm rectangular-shaped panel that was further processed to extract the test specimens. The final specimen geometry used in this work was derived from the DIN EN ISO 527-1 technical standard by adapting the size (See Figure 3.3) to fit into the test machines presented in Section 3.2.3. The constant cross-section test area was 8 (± 0.1) mm long, 6 (± 0.1) mm wide and had a thickness of 500 (± 100) µm.

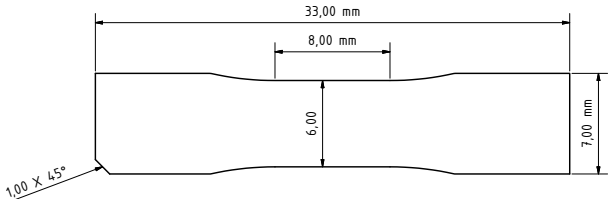

Figure 3.3: Geometry of the neat resin specimen

After curing and post-curing, a EuroMod CNC-milling machine equipped with a milling frame was used to machine the dogbone-shaped geometry, as shown in Figure 3.3. After machining, the cut surfaces were manually polished using 600 / 1000 / 2500 abrasive paper manufactured by Starcke GmbH & Co. KG.

3.1.4 Specimen Conditioning

Before testing, all specimens are stored at 23 (± 2) °C and 50 (± 10) % relative humidity (RH) for at least 96 hours and until weight equilibrium is reached to achieve the "as produced" moisture content (Specified as reference state and ambient conditions). If not otherwise specified, the exposed and tested specimens are also stored at ambient conditions prior to further analysis and testing.

3.2 Analysis Methods and Basic Characterization

The second part of the materials and methods section gives an insight into the data collection process. For each method used in this work, details of the equipment and applied techniques are given, along with the acquisition parameters. In addition, a basic characterization of the material using these methods in the reference state is provided. For the Fourier-transformed infrared spectroscopy (FTIR), a more detailed description of the acquisition process is provided since it is the major analysis method in this work. For the other well-established methods, such as mechanical testing, differential scanning calorimetry (DSC) and thermal gravimetric analysis (TGA), a basic description is given. Further information can be found in [19].

3.2.1 FTIR Acquisition Techniques

Several methods to acquire FTIR data have been developed and applied in the past [3]. The two widely used methods are based on transmission (TRS) and attenuated total reflection (ATR), as shown in Figure 3.4. Both techniques are characterized by easy application and high signal quality.

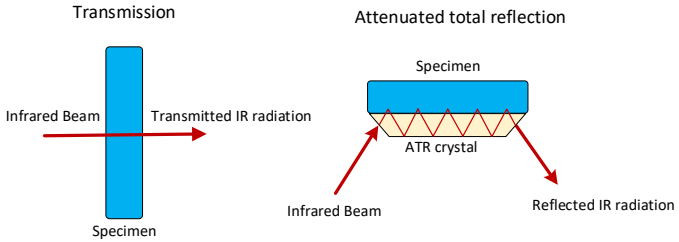

Figure 3.4: FTIR acquisition modes: transmission (left) and reflection (right)

TRS spectroscopy represents a contactless FTIR acquisition technique mainly used for quantitative measurements. It is advantageous due to a high signal-to-noise ratio and is, therefore, less susceptible to scatter compared to other sampling techniques. However, this method has a number of limitations, in particular in regard to thickness dependency and measurable infrared bands. Hence, dependent on the material and thickness of the specimen, the transmissivity may also be low and TRS may not be applied at all. On the other hand, TRS acquires an integral value along the measuring path giving information about the bulk chemical composition of the specimen and allows easy quantification. The second applied sampling technique is the ATR, where the specimen is in contact with a crystal made of highly refractive material. This technique is mainly applied because of its easy sampling procedure and the ability to measure highly absorbing materials. However, it shows a low reproducibility due to its low penetration depth and high sensitivity to the applied pressure of the crystal on the specimen. Furthermore, ATR only analyzes the surface of the specimen while penetrating 2 – 10 µm. Also, the acquisition depth is highly dependent on the wavenumber. Further details on different FTIR acquisition modes can be found in the following excellent sources by Griffiths and Koenig [3, 8].

3.2.2 FTIR Spectral Band Considerations

A trade-off between signal quality and wavenumber limitation has to be performed when measuring infrared spectra. The penetration depth of ATR measurements is highly wavenumber dependent. While wave numbers around 3500 cm^{-1} show penetration depths up to 0.5 µm, higher values can be achieved when using lower wavenumbers yielding depths up to 8 µm [20]. For transmission measurements, the thickness consideration reverses. With rising specimen thickness, the probability of absorption rises, reducing the transitivity. In order to achieve high-quality spectra, the transmitivity range between the baseline and the signal should be chosen as big as possible. However, non-linearity limits the minimal transmission values and has to be considered for transmission values below 30 %. Furthermore, very thin specimens tend to generate interference fringes through in-specimen reflection, which can be seen for the 0.03 mm specimen, making a rough surface necessary [3]. The assignment of the spectral bands was performed according to previously published literature and publications [21, 22].

Mid Infrared Region (MIR)

The MIR region ranges from 500 cm^{-1} to 4000 cm^{-1} and is characterized by a high information density. Figure 3.5 shows the FT-IR spectrum for the reference spectra for the RIM-system, where the absorption is plotted against the wavenumber in cm^{-1}. On the most right side of the MIR spectrum, the so-called fingerprint region (500 cm^{-1} to 1800 cm^{-1}) is found. This region is characterized by highly overlapping fundamental vibration modes, allowing the identification of a specific material. Additional isolated bonds can be found in the area from 2800 to 4000 cm^{-1} [8].

Reference MIR Spectroscopy Measurements

To obtain transmission spectra, a Bruker Tensor 2 FTIR spectrometer equipped with a transmission cell was used. The spectrometer is equipped with a globar MIR source, a KBr beam splitter and a RT-DLaTGS Detector. The applied spectral range for transmission measurements was 500 cm^{-1} to 6500 cm^{-1}. Before measuring each specimen, a 40-scan averaged background signal was acquired to eliminate the influence of fluctuating ambient conditions on the measurements. Each FTIR data vector consisted of an average of 8 specimen scans using a resolution of 2 cm^{-1}. The Blackman-Harris 3-term apodization was used for FTIR data collection. In the end, the IR-spectra were exported as DPT files for further data processing without internal pre-processing (PP).

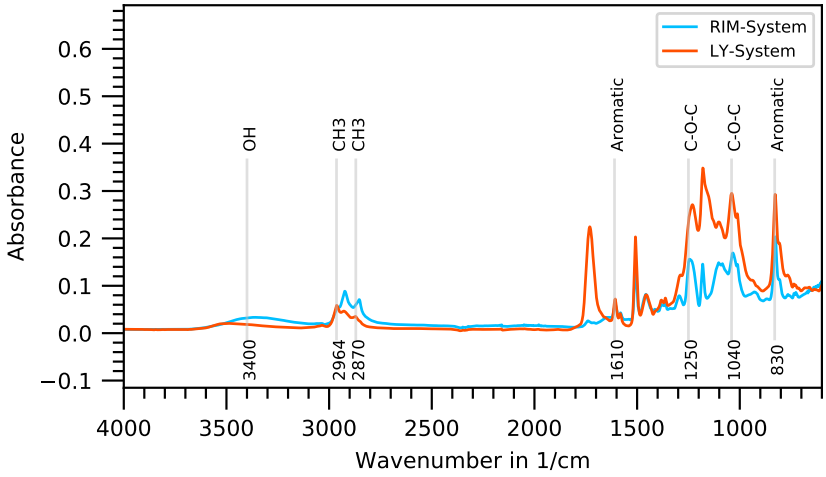

Figure 3.5: Reference spectra for the RIM-System and LY-System in the mid-infrared region acquired by using film specimens of 25 (± 10) µm thickness measured in transmission mode

Near Infrared Region (NIR)

The intensity of the absorption generally decreases with rising wavenumber. This effect is a result of a reduced probability of excitation with the increase of the order of the overtone. Therefore, the second infrared region ranging from 4000 cm^{-1} to 12500 cm^{-1} usually shows a lower intensity. It consists of combination vibrations of the fundamental vibrations and overtone regions. The NIR region shows a significantly lower information density in comparison to the MIR region but allows higher penetration depths and yields lower overlapping.

Reference NIR Spectroscopy Measurements

The Bruker Tensor 2 device is capable of acquiring FTIR data up to 6500 cm^{-1}. However, with increasing wavenumber, the SNR ratio decreases due to lower detector detectivity and the lower intensity of the infrared source in this region. Exemplary, Figure 3.6 shows the reference spectra of both epoxy systems in the NIR region acquired with the Bruker Tensor 2 instrument using the same instrument setup as for the MIR region. Clearly, the IR intensities are lower and the single peaks are broader and less sharp.

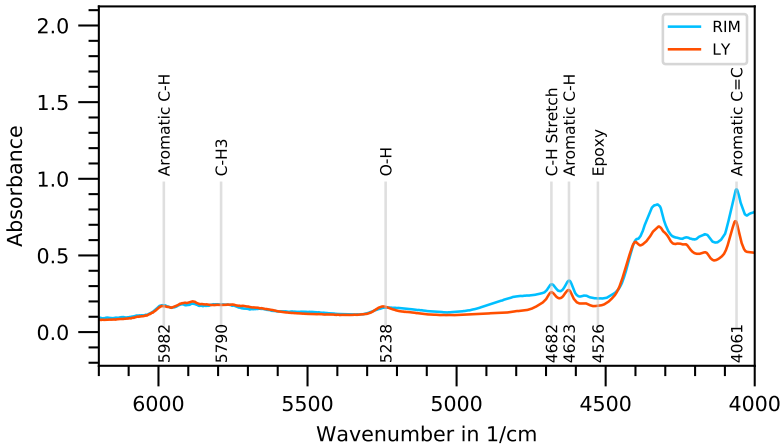

Figure 3.6: Reference spectra for RIM-system and LY-System in the near-infrared region acquired by using dogbone specimens of 500 (± 100) µm thickness measured in transmission mode

3.2.3 Mechanical Testing

Mechanical testing is performed to analyze the elastic, visco-elastic and plastic response of the specimen due to load application. The tests provide information on the load-bearing capabilities of the material and are the major approach to determining load limits.

Reference Tensile Tests

In this work, two different experimental setups have been used to perform static and dynamic tensile tests. To determine time-dependent material behavior, the Dynamic-Mechanical Thermal Analysis (DMTA) device (Gabo Eplexor 500 N) was used due to its capabilities of fast loading and accurate force application. For static tensile tests, the DEBEN microtest - 200N tensile stage was used. Figure 3.7 shows representative stress-strain curves for both epoxy resin systems in the reference state. The average maximum stress of the LY specimens is 84,8 MPa, while the RIM specimens achieve 63 MPa (at 1mm/min). Both values are on the lower end of the strength specified in the datasheet (RIM 60 - 75 MPa, LY 83-93 MPa). The elongation at break is found to be at 9.9 % for the RIM specimens (Datasheet 8 - 16 %) and at 9.1 % for the LY specimens (DS 5 - 7 %). The modulus is found to be 2.93 GPa for LY- (DS: 3.1 – 3.3 GPa) and 2.63 GPa (DS 2.7 – 3.2 GPa) for the RIM-system. The deviation between measured and TDS values is connected with the non-standard specimen geometry, the specific curing conditions and pre-conditioning at a standard atmosphere before testing.

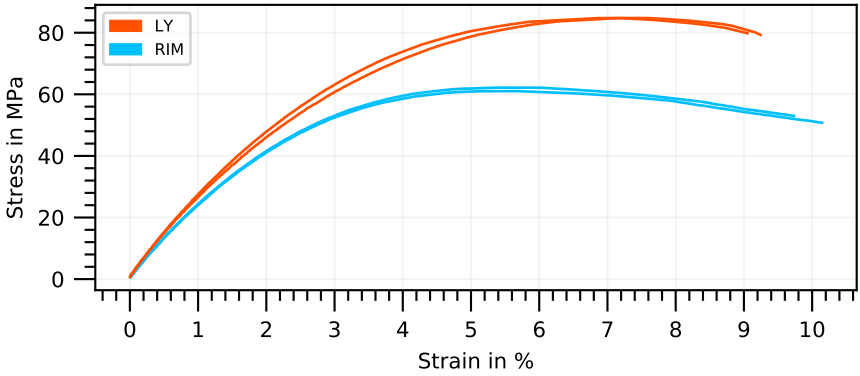

Figure 3.7: Reference stress-strain curves for the RIM-System (blue) and LY-System (orange) dogbone specimens

3.2.4 Differential scanning calorimetry (DSC)

The DSC is applied to measure the quantity of heat exchanged during a temperature variation of a substance. Based on the heat flow, the specimen absorbs or releases energy along with a change of internal energy. Generally, DSC is capable of detecting physical changes as well as chemical reactions such as crystallization, melting, glass-transitions or curing [19]. In this work, DSC was used to gain information about the curing state and the glass-transition temperature of the epoxy specimens. Furthermore, relaxation processes will be studied by observing the mobility of polymeric chains for different energetic states.

Reference DSC Measurements

In this work, the measurements were performed using a Netzsch DSC 204 F1 Phoenix device, applying a heating rate of 20 K/min in the range of 23 °C to 250 °C. The standard DSC curves of reference specimens are displayed in Figure 3.8, showing the glass-transition region. The onset of the glass transition temperature for the LY system was found to be at 127.68 °C, slightly below the datasheet specifications, while the RIM system Tg onset value was measured at 87.1 °C within the datasheet specification.

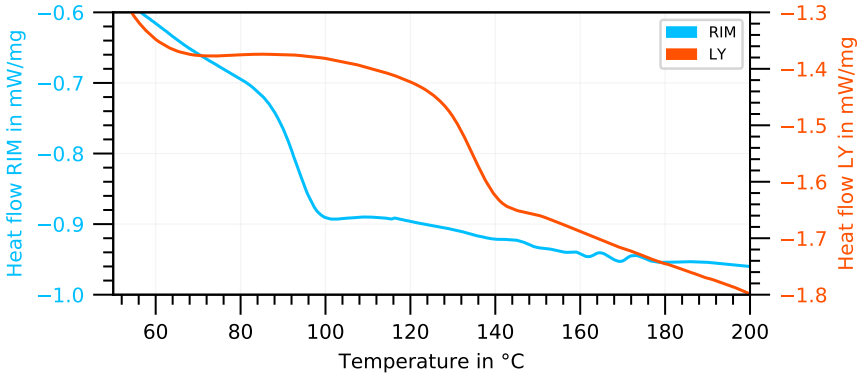

Figure 3.8: Reference DSC curves for specimens made of the RIM-System (blue) and LY-System (orange)

3.2.5 Thermal gravimetric analysis (TGA)

TGA is applied to determine the mass change of substances under variation of time and temperature within different atmospheres [19]. The analysis allows a statement about chemical and physical processes occurring in the specimen, such as the decomposition or evaporation of volatile components. In this work, TGA is mainly applied to determine suitable testing temperatures for thermal degradation and the onset temperatures for the water desorption process.

Reference TGA Measurements

The experiments were performed under a nitrogen atmosphere using the Q500 TGA device manufactured by TA Instruments at a heating rate of 10 °C/min. As can be seen in Figure 3.9, the relative mass decreases after reaching the decomposition onset temperature. The amine-based RIM system shows a lower thermal onset temperature at 330 °C, while the anhydride-based LY system undergoes a two-step thermal decomposition initiating at 200 °C and 389 °C. This observation indicates different chemical or physical processes responsible for the weight changes. The expected initial weight drop due to moisture desorption is almost invisible in the present graph due to scaling.

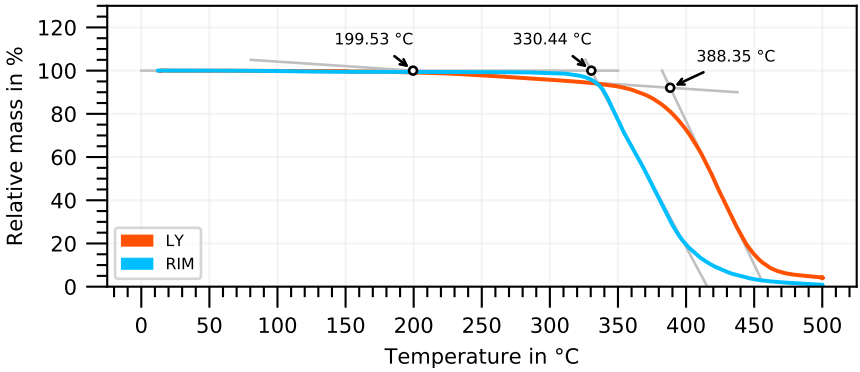

Figure 3.9: Reference TGA measurements for specimens made of the RIM-System (blue) and LY-System (orange)

4 Data Handling and Analysis Methods

4.1 Introduction

In the previous section, methods to acquire material data from different sources have been presented. In this section, the data flow and the main building blocks are introduced. The processing and analysis process's key aim is to create an accurate and reliable link between measured raw input data and unknown material properties.

4.2 Data pipeline and model

In data science, the composition of algorithms to transform raw data into meaningful values is called a data processing pipeline (DPP). In general, a DPP can include linear and non-linear connections and complex dataflow with feedback, interconnection, and temporary storage. The DPP used in this work contains two pipeline paths that partly use the same building blocks. These are the modeling path (MP), where the predictive model is created and the application path (AP), where the model is applied. For the AP, only new spectral data is required, while the material properties are calculated using the predictive model. Both paths are depicted in Figure 4.1 using red (AP) and blue (MP) colors consisting of pre-processing (PP), feature extraction (FE) and modeling, respectively, model application. In the following sections, the details of the building blocks will be described and explained.

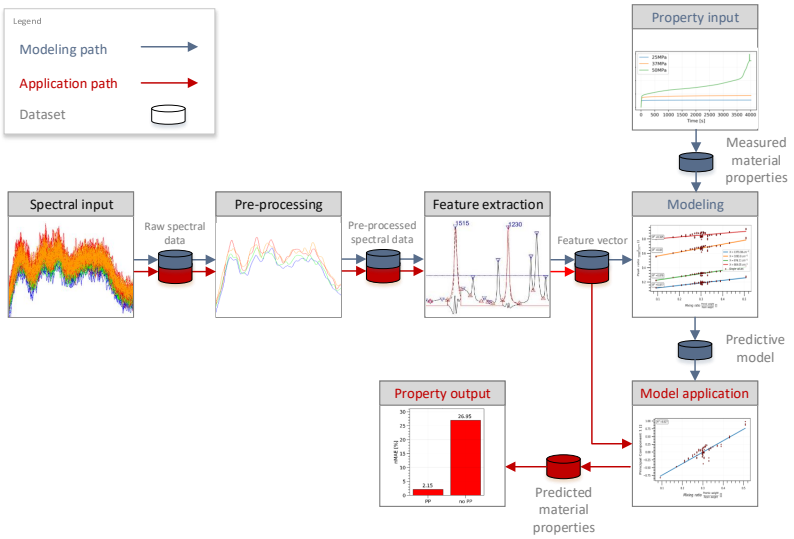

Figure 4.1: Overview of the data processing pipeline

The main difference between MP (blue symbols) and AP (red symbols) lays within the input and output data. The MP is used to create a validated predictive model with set accuracy requirements as output, whereas spectral data, as well as measured material properties are used as input. As shown in Figure 4.1, the creation of the MP includes an iterative approach of combining and evaluating different pre-processing and feature extraction algorithms. Once the MP achieves the required performance and is validated, the PP and FE algorithms are fixed and the predictive model is released to be used on new data in the AP.

4.2.1 Data Handling Software Environment

In this section, a short introduction to the software environment's capabilities is given. The data analysis is performed using Python programing language and Jupyter Notebooks, a highly interactive browser-based environment combining Text, Code and Visualization [23, 24]. In addition to standard Python code, the Numpy, Scipy, Matplotlib and Scikitlearn libraries are used [25–28]. The base for all data handling steps is laid by the Python Pandas library providing data

management comparable to the functionality of databases. As part of the Python ecosystem, it provides easy integration and combination with other packages and functions [29].

4.3 Data Processing

In this section, an explanation of the single DPP building blocks, as shown in Figure 4.1, with a focus on the spectral data, is given. A brief introduction to data pre-processing is given first to explain the origins of undesired variation and how these challenges have been met, followed by feature extraction and modeling.

4.3.1 Spectral Data Considerations

In theory, the observation of a single IR band representing a specific molecular configuration of a particular material should allow the establishment of a direct link between the measured IR signal and a physical or chemical variation. However, a clear single peak is the exception rather than the rule due to natural statistical scatter, measurement errors, overlapping spectral bands, and chemical end groups' interactions. Therefore, the major challenge in this work is to find relevant patterns for all investigated phenomena and identify the origin of the changes.

4.3.2 Pre-processing

Next, the concept behind the single data pre-processing steps is given. Data pre-processing is justified by the fact that spectral deviations originating from errors connected with specimen preparation and the acquisition process do not contain information concerning the physical and chemical phenomena. This work focuses on understanding the origin of data deviation and choosing the correct data pre-processing steps accordingly. Therefore, the potential errors from the data acquisition process were analyzed. Scatter originating from handling errors such as picking a faulty background, detector noise, and specimen thickness variation have been taken into account. Where possible, automated pre-processing is performed to exclude personal judgment from the process to prevent bias. The approach to pre-process raw spectral data is provided with the aim and complies with the overall target of increasing the prediction accuracy.

4.3.3 Handling Error Detection

First, data cleaning is performed to exclude obvious handling errors by detecting and deleting incomplete or faulty data, e.g., faulty background measurements. If a linear pattern of the signal variation is expected, obvious outliers are detected and excluded from further analysis by applying a principal component analysis. However, a certain amount of variation is expected in the spectral data of a TSP due to the statistical nature of FTIR measurements. It is important to remember that the acquired spectral value represents the average value for the analyzed penetrated path and molecular state.

4.3.4 Signal-to-Noise Ratio

This statistical scatter can be reduced by increasing the signal-to-noise ratio (SNR) by choosing appropriate sampling parameters. Generally, it can be said that a trade-off between acquisition time, spectral resolution and SNR has to be performed. Detector noise is known to be stochastically distributed and depends on detector material and therefore, also on the spectral region. Detectors used for NIR usually show a significantly lower SNR and a higher detectivity when compared to MIR detectors. In order to achieve good quality spectra for single measurements, the single measurements are binned into a single resulting spectrum. Usually, the combination encompasses 8 to 64 single measurements combined by averaging. For dynamic measurements, a smoothing of the resulting spectra is performed using a moving averaging filter introduced by Abraham Savitzky and Marcel Golay, where a polynomial function approximates the data [30].

4.3.5 Specimen Thickness, Reflection and Scatter

The spectral intensity for a given material depends directly on the length of the penetrated path. Using the Lambert-Beer-Law previously presented, a correction for thickness variation can be established. In order to scale the spectra into a similar range, a baseline correction and normalization were applied. For the normalization, the whole spectrum was linearly scaled according to the intensity of the reference bands. Therefore, the reference bands of aromatic ring bonds (C-C stretch at $1509\,\mathrm{cm}^{-1}$, C=C stretch at $1608\,\mathrm{cm}^{-1}$, or C-H stretch at $4066\,\mathrm{cm}^{-1}$ or $4623\,\mathrm{cm}^{-1}$) have been used depending on specimen thickness and analyzed spectral band. Previous studies showed that aromatic bonds were suitable for

normalization at moderate temperature since they possess the highest chemical stability of the bonds within the epoxy resin network, as will be shown in Section 7.1.3.

4.4 Dimension Reduction

Dimensionality reduction is applied to convert the pre-processed spectral vector to feature vectors by deriving non-redundant information important for the desired observation. In this work, this approach is mainly used to reduce the size of the spectral vectors while maintaining the inherent content of the physical and chemical information. Using feature vectors instead of raw data vectors reduces the risk of overfitting while increasing the speed of model training for machine learning algorithms [8]. A special form of dimensionality reduction is feature extraction. For spectral data, instead of using the single data points describing a peak shape, general peak properties are derived and processed to a feature vector. Two categories of features are defined and will be covered in this work. Inherent features are directly measurable and calculated by considering a subset, e.g., a specific wavelength of the data. Derived features are defined as dislocated properties (not connected to a specific wavenumber) that need an algorithmic processing step to be revealed, e.g., the calculation of a peak position based on the weighted averaging and smoothing of spectral vectors.

4.4.1 Inherent Features

The simplest way to extract a feature vector can be performed by choosing the maximum value for a specific wavenumber. The accuracy of this approach can be improved by considering the discrete nature of spectral data and obtaining the maximum value by interpolation. A special form of interpolation is represented by the approximation using a Gaussian profile. It can be used to describe the spectral shape of solids, which is also true for cured TSP [8]. The lmfit Python library was used in this work to perform the peak fitting operation [31], as shown in Figure 4.2.

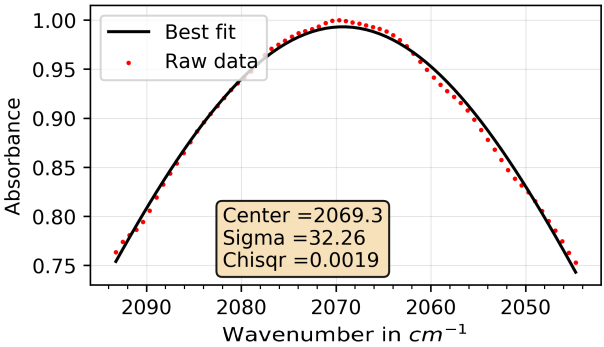

Figure 4.2: Gaussian profile fitted to highly scattered spectral IR data in the range

Another feature is represented by the integral value, which can be calculated using different methods and boundaries.

4.4.2 Principal Component Analysis

Principal component analysis (PCA) is based on the assumption of information redundancy in data. It is assumed that a high-dimensional vector can be reduced to a smaller number of derived features without losing a significant amount of information. The calculation of the explained variance value after PCA allows the estimation of the percentage of lost information. A detailed explanation of the PCA method can be found in the literature and is not within the scope of this work. A good introduction to the application of PCA for FTIR data can be found in [32]. In this work, PCA is applied in three different ways. First, the PCA approach is used to reduce scatter from the data acquisition process by deleting high-order principal components and reconstructing the spectral data. Second, by applying clustering algorithms on the first and second principal components, outliers can be effectively identified and deleted. Third, the PCA will be used as a feature extraction method to reduce the input vector for further analysis, e.g., by reducing the length of the FTIR data vector.

4.5 Modeling

4.5.1 Modeling complexity

Depending on the complexity of the expected underlying physical and chemical observations in the experiment, a suitable model has to be chosen to describe the dependence (See Figure 4.3). Application of the DPP in Sections 5 to 7 starts with a simple model and increases the model complexity as required by the application. If a simple linear dependence with known influenced spectral bands is present, a simple vector entry-based linear regression (LR) model can be chosen. If the dependence is linear but hidden throughout the spectrum or feature vector, the dependence can be uncovered using principal component regression (PCR). Finally, if the link between data and information vector is neither known nor linear artificial neural networks (ANN) can be applied to establish a model to describe the interconnection. It is important to understand that for linear problems, the performance of ANNs is expected to be lower compared to PCR/LR, with significantly higher computation costs. Overall, the complexity of the model should be as low as possible due to the limitation of available data or specimens and the dimensionality of the underlying pattern to prevent overfitting. Therefore, the key to a good model is to cover the core of the problem by generalizing the underlying dependencies and excluding unimportant features and data variation sources. Only a brief introduction to the concepts is provided next, while details and information regarding implementation can be found in [33].

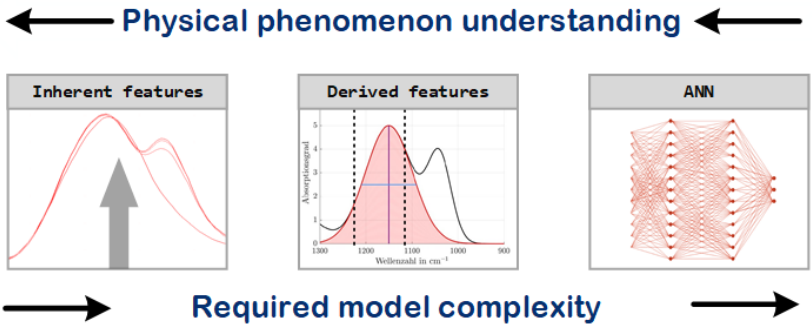

Figure 4.3: The relation of physical insight depth in comparison to the required model complexity

4.5.2 Machine learning

A very simple but accurate definition of the term "Machine Learning" can be found in the following quote written by Cassie Kozyrkov [34].

"Instead of giving explicit instructions, you program with examples and the machine learning algorithm finds patterns in your data and turns them into those instructions you couldn't write yourself."

Hence, in comparison to the previously presented analytical approaches, where rules and code have to be implemented directly, machine learning describes an approach where automated pattern detection in data takes place. This is particularly useful if the underlying processes are unknown, not well understood and a reduction of the complexity would lead to an oversimplification of the problem. Artificial neural networks (ANN) represent a set of algorithms where simple processing units called neurons form an interconnected network to process data between an input and an output, as can be seen in Figure 4.4. While the number and complexity of the hidden and output layers can be chosen arbitrarily and task-dependent, the size of the input layer is determined by the length of the data input vector. The single neurons are fed from the input or previous layer with scalar values. The data is then processed by a so-called activation function, which sums up the inputs according to the weights and outputs a single scalar value. The weights and the activation function are responsible for the transmission of information to the next layer while the weights are changed and optimized during the training process until convergence is reached. Using spectral data, each wavenumber data point has its own input neuron. If a feature vector is used as input, the input layer is reduced accordingly.

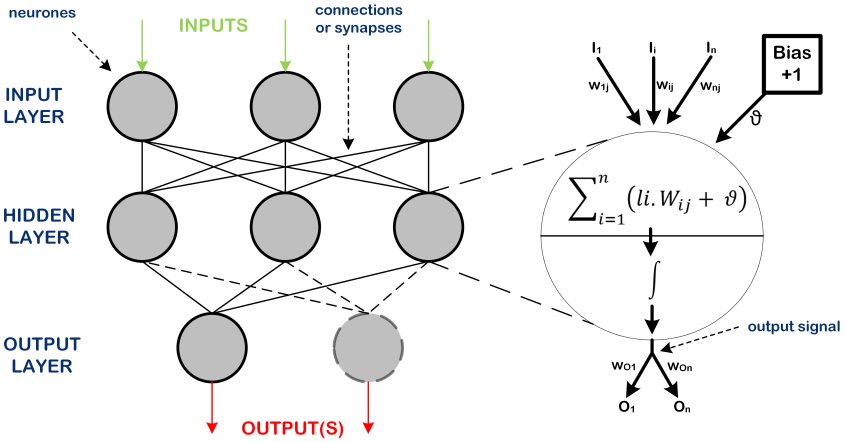

Figure 4.4: General artificial neural network design, adapted from [35]

4.5.3 Training Set, Test Set and Cross-Validation

Once a pattern is identified and described by a model, the question of model accuracy arises. As the training and optimization of model parameters go on, continually improved accuracy is assessed using validation. The aim of the training is to create a model which shows comparable performance between new unseen data and data used for training. If such a model is found, it is stated to generalize. Therefore, instead of using the full dataset for training, the available data has to be split into three parts, the training, validation and test set with specific functionality, as shown in Figure 4.5.

Figure 4.5: Overview of the data sets during training and cross-validation

The size of the training set depends on the complexity of the model and the amount of available data. Generally, complex models such as the ANN require a significantly larger training set than simple linear regression models. If the final test set achieves a significantly lower accuracy compared to the validation

set the model is probably reproducing the scatter pattern in the training set. In this case, the model is stated to be overfitted and a reevaluation of the model complexity and the size of the dataset for training should be considered.

5 Mixing ratio estimation

5.1 Introduction

5.1.1 Motivation

A robust and fast way to accurately determine production variation prior to, during and after the manufacturing process is crucial to ensure high-quality production when using thermosetting polymers. Regarding the overall goal of this thesis to estimate the material state, the following section presents a first, simple model to evaluate the feasibility of the approach of creating a single parameter model. In general, the robustness and dimensionality of the model can be extended by adding influence factors and/or increasing the range and number of conducted experiments. Figure 5.1 shows exemplary important external factors when dealing with the manufacturing of TSPs. However, this list is not exhaustive and is highly application-dependent.

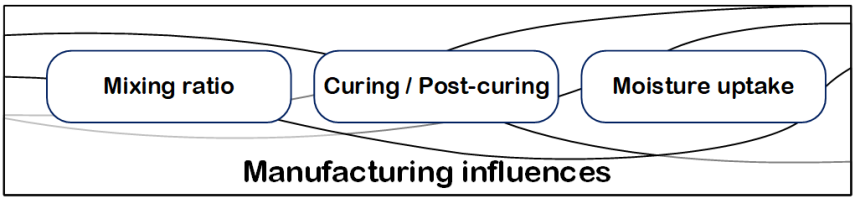

Figure 5.1: Overview of the major external processes having an influence on the material state during manufacturing

As a proof of concept, in this work, the mixing ratio is chosen and analyzed. However, in general, each external influence factor acting on a polymer during manufacturing could be regarded respectively. An additional focus in this section lays on the introduction of methods for the evaluation, choice and application of spectral pre-processing.

5.1.2 Section Outline

First, the extraction process and assessment of useful information from a given spectral dataset are performed. Next, basic features representing the single subcomponents are extracted and processed. An optimal set of pre-processing steps is developed by illustrating the impact of the different methods on the results. Finally, the prediction precision is assured by determining and eliminating noise sources. As a result, the model can be used to identify production-driven deviations and initiate corrective actions during the manufacturing process. Throughout the study, a linear correlation between the mixture ratio and the spectral data is assumed based on Lambert-Beer-Law. The task of estimating the mixture ratio is known to be a linear problem and can be best solved by tools designed for this kind of task. Therefore, linear regression and principal component analysis are mainly considered.

5.1.3 Literature Review

The first step of the manufacturing process of composites is represented by the mixing of the epoxy resin, the curing agent and if applicable, an accelerator. Ensuring the correct mixture ratio during the manufacturing process is essential to achieve the desired physical and chemical properties of the polymer. Currently used techniques to determine the mixing ratio are time-consuming, cost-intensive and usually presuppose a technical background of the personnel performing this task. The optimal mixing ratio for thermosetting polymers is defined by the stoichiometric ratio given by the number of epoxy groups and reactive groups of the curing agent. Using the epoxy equivalent weight and the anhydride, respectively, amine equivalent weight, the stoichiometric ratio can be defined for the present systems. Usually, these values are provided with the delivery documents of the epoxy components. An offset of the mixing ratio leads to a variation of the mechanical properties, e.g., the strength and modulus decrease and the elongation at break increases [36]. Besides, a lower glass-transition temperature is usually observed [36]. The variation of mechanical properties was extensively studied in the past and is not the subject of the investigation.

5.1.4 Data Acquisition Process

Two different epoxy resin systems have been used to illustrate the different challenges arising from the single components. For each epoxy resin system, a set of

specimens with a variation of the predefined mixing ratio have been manufactured. The extent of the weight variation of the curing agent was defined to be limited by 10 % plus and minus. The single steps of the process are shown in Figure 5.2, where the components are added first, then weighed and subsequently mixed and finally, the FTIR spectral data is acquired.

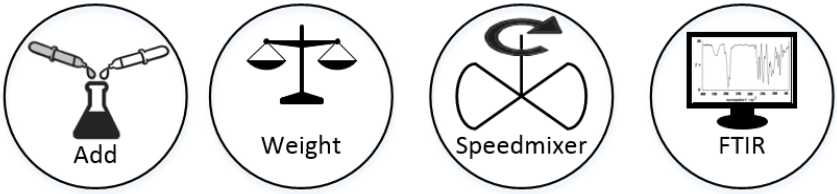

Figure 5.2: Data acquisition approach for the mixture ratio data sets

In the case of the LY-system, the accelerator and the curing agent have been premixed in a ratio of 90:1, according to the datasheet. This approach complies with the datasheet and excludes the ratio between the curing agent and accelerator from the analysis while simplifying an accurate mixing for the anhydride-cured epoxy resin system. For the RIM-system, both components were processed according to the datasheet simultaneously. Cups of the size of 10 ml have been used for the mixing process. The resin was added first, followed by the premix, respectively, curing agent component. A difference between the desired mixing ratio and the achieved mixing ratio cannot be prevented, as can be seen in Fig 5.3 and 5.11. However, this circumstance only leads to a shift of the single measurement point along the calibration curve but has no impact on the calibration itself. The weight was measured using a Sartorius CPA26P Microbalance with a 10 ţg readability (linearity 8 µg, repeatability 4 µg). All specimens have been manufactured by mixing the components using a SpeedMixer DAC 150 device for 30 s at 3000 RPM. The spectral data is acquired in ATR mode using a diamond ATR crystal which is cleaned with isopropanol first. After 30 s solvent flash-off time, a background spectrum is acquired using 40 co-added spectra. The specimens are measured in the liquid state within 10 minutes after the end of the mixing process. The FTIR spectra are recorded using 16 co-added scans at a spectral resolution of 2 cm^{-1}. A single drop fully covering the ATR crystal of the mixed epoxy resin is measured for each data point. In addition, data was also acquired in the cured state after curing according to the curing process

specified in Section 3.1.2. The finally achieved mixing ratios were recalculated once the add process was completed using a precision scale to determine the true mixing ratio.

5.2 Results and Discussion - LY System

An overview of the LY epoxy resin systems dataset used in this section is shown in Figure 5.3. As can be seen, the small calibration dataset (Series 1) contains 11 single specimens with single FTIR spectra. The second dataset (Series 2) contains 15 specimens, each measured five times using the FTIR. For the Series 1 dataset, a mixing ratio (premix:resin) range of 95:100 to 85:100 was used, while the Series 2 dataset ranges from 82:100 to 100:100. The general idea is to perform the calibration of the model using the small accurate dataset and validate the calibration curve using the results of a bigger less accurate dataset with a wider mixing ratio range.

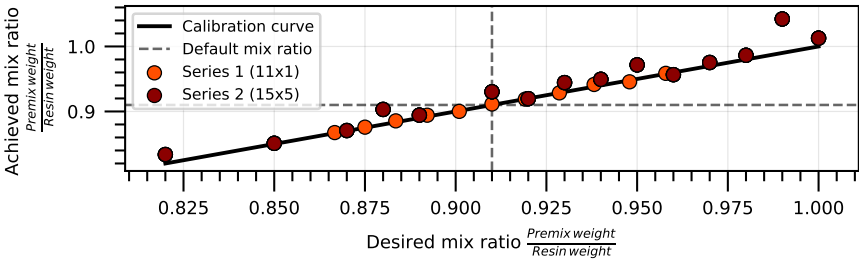

Figure 5.3: Dataset overview for the LY epoxy resin system mixing analysis

The basic spectra for the LY epoxy resin systems and their pure components are shown in Figure 5.4. Clear differentiation between the epoxy resin and the curing agent can be done. The epoxy resin shows high absorbance at the aromatic bands at 830 cm^{-1}, 1508 cm^{-1} and 1608 cm^{-1} and a characteristic absorbance at the oxirane band at 915 cm^{-1}. The spectrum of the curing agent shows a unique carbonyl band at 1772 cm^{-1}. The spectral properties of the accelerator, on the other hand, highly overlap with the epoxy resin and potentially have the ability to be a source of scattering. A more detailed analysis of the single spectra is performed next.

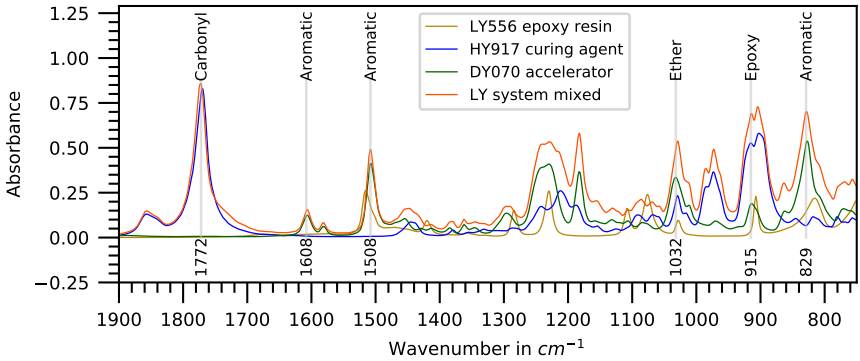

Figure 5.4: Components of the LY epoxy resin system, LY 556 resin (gold), HY 917 curing agent (blue) and the accelerator DY 070 (green). The mixed LY epoxy resin system in orange.

5.2.1 Spectral Band Allocation

In Figure 5.5, spectral information of the Series 1 dataset is presented. All 11 infrared spectra of the calibration set are displayed in blue. Due to the low overall variation, the difference between the spectra is hardly noticeable. Therefore, the variance is calculated for each wavenumber along the specimen axis displayed as a red line. Besides the spectral contributions of the single components, assuming linearity with the pure component spectra, are displayed in the background. First, the maxima of the variance curve are chosen, and the spectral contribution at the closest spectral peak position is calculated (See Table 5.1).

Table 5.1: Spectral contribution of the single components of the LY-System at discrete wavenumbers

		Wavenumber in cm^{-1}				
		1772	1508	1182	904	828
LY 556	[%]	0.24	95.31	6.18	23.87	68.88
HY 917	[%]	99.75	2.48	91.37	75.92	28.64
DY 070	[%]	0.01	2.21	2.46	0.21	2.49

Based on this analysis and with the knowledge from Figure 5.4, the carbonyl band of the curing agent located at 1772 cm^{-1} represents a good choice to quantify this component. A spectral contribution value of 99.75 % of the spectral absorbance at 1772 cm^{-1} confirms this choice, especially if the spectral contribution of the accelerator with 0.01 % and the epoxy resin with 0.24 % is considered. The same approach is performed for the choice of the spectral band representing the epoxy resin. In fact, both aromatic bands at 1508 cm^{-1} and 829 cm^{-1} show high spectral contribution. Though, due to the higher value at 1508 cm^{-1}, this peak is chosen to represent the epoxy resin. Even though the pure spectra of the epoxy resin showed high overlap with the accelerator, the contribution toward the mix signal only accounts for 2.48 % of the signal. This choice is also beneficial considering measurement path length variation since the proximity of evaluation peaks minimizes deviations from penetration depth variation.

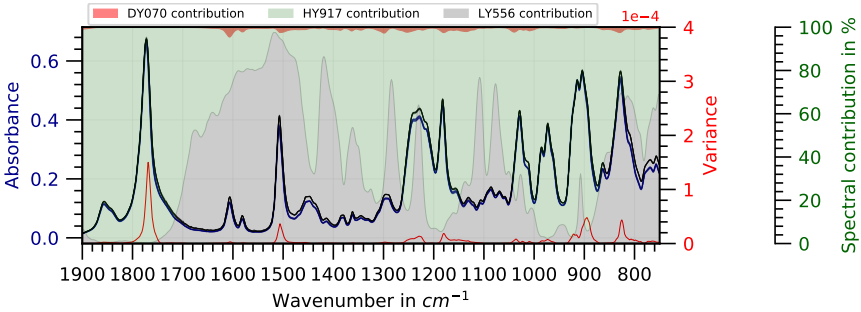

Figure 5.5: Spectral data overview, showing the variance, the absorbance of the single spectra and the spectral contribution from different components.

5.2.2 Dataset Dimensionality and Structure

Using the PCA, the underlying structure of the raw data can be analyzed to discover the dimensionality of the data. Figure 5.6 shows the principal component weights over the achieved mixing ratio for the first two principal components for the Series 1 dataset. Clearly, the variation of the mixing ratio leads to a linear dependence which accounts for 97 % of the explained variation. The second principal component does not show a clear structure and therefore, it can be assumed that the values of the PC 2 are randomly distributed and not relevant for further analysis. As a result, a linear model can be used to establish a link

between the mixture ratio and the data. This result is not surprising considering the Lambert-Beer-Law where the concentrations of a two-component system add linearly. Though, additional effects, such as chemical reactions, may occur and have to be excluded when performing this analysis.

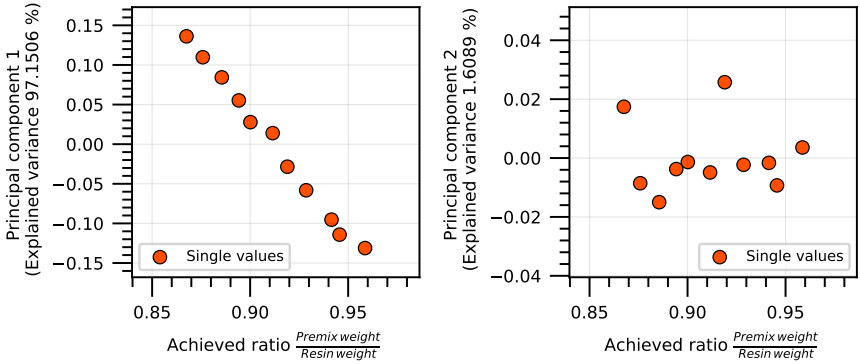

Figure 5.6: PCA of the raw data for the LY epoxy resin system mix dataset showing principal component 1 (left) and principal component 2 (right)

5.2.3 Pre-processing and Feature Extraction

Now that a deeper insight into the dataset has been acquired, several pre-processing (PP) and feature extraction (FE) steps are evaluated to generate different models and test them for accuracy. In the end, the best set of steps is chosen to generate a model for application in order to predict the mixing ratio. Several pre-processing steps and feature extraction models have been used on the calibration dataset and compared with the aim of maximizing the coefficient of determination R^2. The best results could be achieved with the normalization step using the aromatic peak at 1508 cm^{-1}. Furthermore, a Sawitzky-Golay filter using a window length of 7 and a function order of three also produced promising results. Both pre-processing steps will be used in combination with three different feature extraction steps. They are the raw peak value, the cubic peak approximation and integral ratios.

5.2.4 Linear Model Calibration Set

Next, the PP and FE steps are applied on the calibration set to choose the wavenumber with the lowest deviation. The results are presented in Figure

5.7, where the normalization PP step with the cubic peak approximation was used. As can be seen, the peak absorbance value for the carbonyl band at 1772 cm^{-1} yields the best results achieving a coefficient of determination of 9.94. The other two bands showed higher scatter, which is reasonable, recalling the lower variance compared to the carbonyl band. Hence the carbonyl band will be used for further analysis.

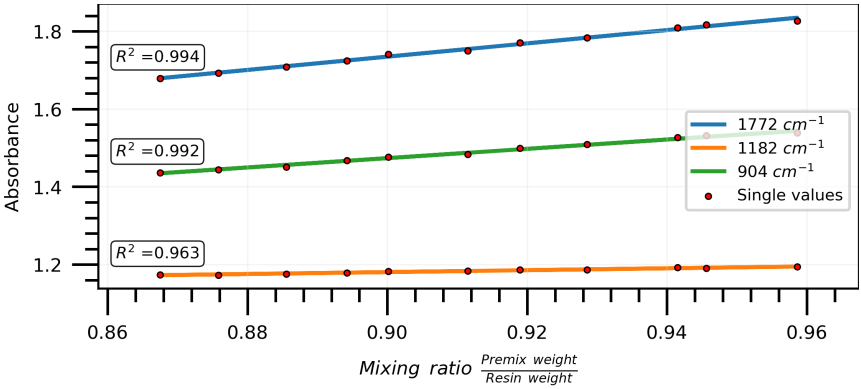

Figure 5.7: Calibration model for the mixing ratio for the LY epoxy resin system

After the selection of the spectral band which will be used for the analysis, the pre-processing steps and the FE methods are further analyzed. As can be seen, by using the raw peak values after normalization, the best-combined results can be achieved. The coefficient of determination is equal for the cubic peak and the raw peak in combination with smoothing and normalization when used on the calibration dataset. However, comparing these values on the validation dataset clearly shows that choosing the raw peak value in combination with data normalization yields the best results achieving an R^2 value of 0.656 and an MSE of 0.0026. It was shown that the use of integral values does not lead to higher accuracy when compared with the peak extraction method. Though, it has to be considered that the peak value is highly spectral resolution-dependent and the integration method may be beneficial if a spectral resolution variation is expected between datasets.

Figure 5.8 illustrates the results of the calibration model and the validation set. Generally, a clear correlation between a rising absorbance and an increasing

Table 5.2: Influence of pre-processing and feature extraction on model accuracy using the carbonyl peak (1772 cm^{-1})

	R^2 calibration set			R^2 validation set			MSE validation set		
Normalized	o	x	x	o	x	x	o	x	x
Smoothed	o	o	x	o	o	x	o	o	x
Raw peak value	0.983	0.994	0.994	-1.793	0.656	0.625	0.001	0.0026	0.0028
Cubic peak approx.	0.983	0.994	0.994	-1.719	0.649	0.625	0.001	0.0027	0.0028
Integral ratio	0.991	0.991	0.992	-0.64	-0.640	-0.573	0.0126	0.0126	0.0111

mixing ratio can be seen. The scatter of the validation dataset is significantly higher compared to the calibration dataset from Figure 5.7. The reason for this observation lays within the lower SNR ratio achieved in the validation set due to a lower FTIR signal amplitude. Furthermore, it was found that the standard deviation of the weight measurements was significantly higher for the validation set.

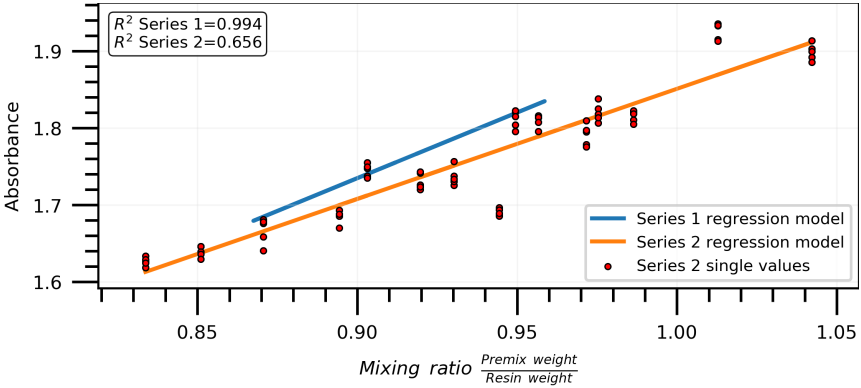

Figure 5.8: Application of the calibration model on the Series 2 dataset

5.2.5 Influence of the Curing State

Another explanation for the deviation of the regression models may be found in the curing of the epoxy resin. One can see that the deviation of the model increases with the share of the curing agent. It is expected that with a rising curing agent and accelerator content, the curing reaction sets on faster and it may have an influence on the mixing ratio determination. Due to the fact that the carbonyl band is consumed during the curing reaction, the model is highly time-critical, especially if the curing temperature was reached during the

manufacturing process. Since the LY epoxy resin system is a hot curing system, the reaction initiation at room temperature can be neglected if the time between mixing and the measurement is kept small. Hence the presented calibration approach is considered valid. As shown in Figure 5.9, this is not true for longer time durations and especially, not true if the polymer is in the cured and post-cured state. With progressing curing, the carbonyl band at 1772 cm^{-1} and the oxirane band at 915 cm^{-1} disappears.

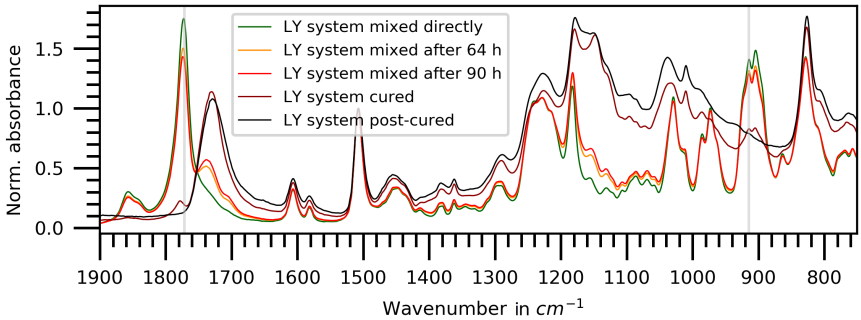

Figure 5.9: LY system at different curing states

As an indication of the effect, Figure 5.10 shows the derived spectral features for the calibration set in the cured state. Clearly, the model is no longer applicable due to a linear shift and higher scatter. Nonetheless, the slope of the model is comparable to the slope of the single values. This effect and additional influence factors have to be further evaluated prior to the application of this model.

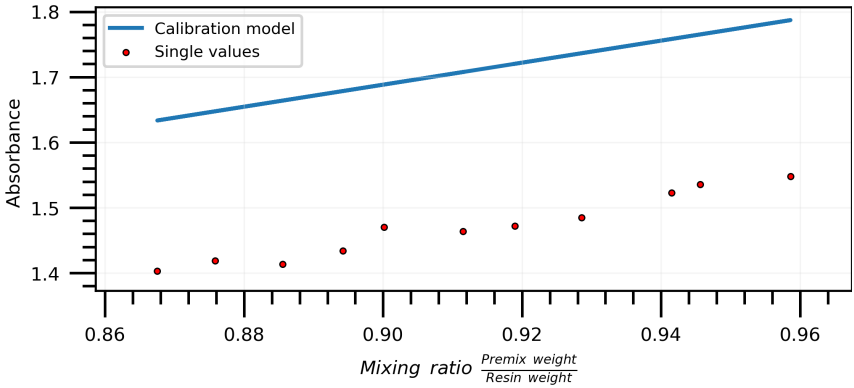

Figure 5.10: Application of the calibration model on the cured specimens of the Series 1 dataset

In this section, the general approach to develop a calibration model for the mixing ratio was presented for an anhydride-cured epoxy resin system. The limitations of a linear model based on single features have been presented and explained. In the next section, the model will be extended using a more sophisticated data analysis using an amine-curing agent-based epoxy resin system.

5.3 Results and Discussion - RIM system

The previous section showed how a linear calibration model could be established using pre-processing and feature extraction methods. In this section, the acquired knowledge will be used and the normalization step and the peak values are set as the default method for the extraction of spectral features. In addition, an approach to cope with highly overlapping peaks and more scattered data is presented. A dataset consisting of 39 specimens representing a variation of the mixing ratio of the RIM epoxy resin system is used. The dataset consists of two different measurement series performed on two different dates. Each specimen was measured three times, totaling a number of 117 single spectra underlying a distribution around the default mixing ratio, as shown in Figure 5.11.

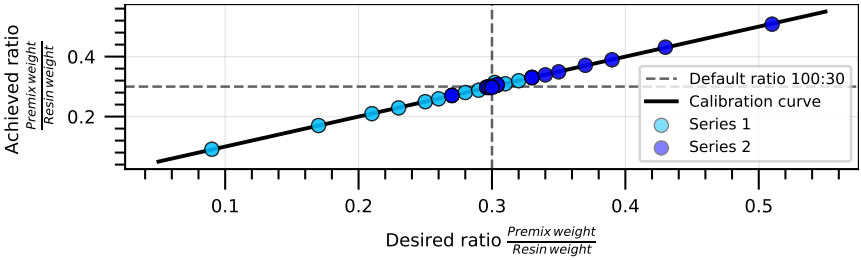

Figure 5.11: Single measurements of the RIM epoxy resin system dataset

5.3.1 Single Components of the RIM System

The single FTIR spectra of the components of the amine-based epoxy resin system (blue) composed of the RIMR 135 resin (gold) and the RIMH 137 curing agent (red) are shown in Figure 5.12. As stated in Section 5.1.1, the single components do not consist of a single molecular species but are rather composed of several subcomponents which are partly of unknown share. Therefore, an accurate assignment of single molecular species with spectral bonds is not always possible. As seen before, the resin can be identified using aromatic bands, especially the one at 1508 cm^{-1}. The other aromatic band of the resin at 829 cm^{-1} highly overlaps with the molecular band of the curing agent.

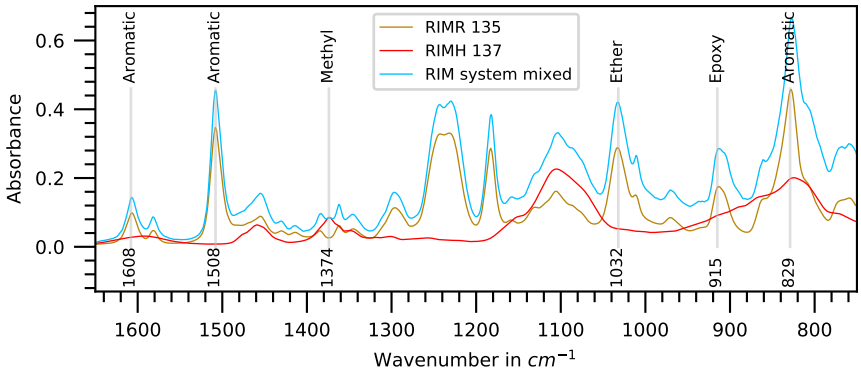

Figure 5.12: Single components of the RIM epoxy resin system and the mixed epoxy resin system

Overall, the curing agent does not produce isolated infrared bands in this epoxy resin system but has a strong peak at 1105 cm^{-1}. For the next steps, the dataset is divided into a test and a validation dataset, while 80 % (93 spectra) of the specimens are used for the model development, 20 % (24 spectra) of the specimens are kept for validation and the model accuracy evaluation. A separate test and validation set is unnecessary since the model uses a validation step during training.

5.3.2 Pre-processing and Outlier Detection

Based on the knowledge from the previous section, all spectra have been normalized at the 1508 cm^{-1} aromatic peak prior to further processing. Single specimens with high deviation may have a big impact on the calibration model and if possible, outliers should be deleted or marked. Several pre-processing steps have been evaluated to reduce the scatter of the data. Figure 5.13 shows the accumulated absorbance intensity distribution prior to (left) and after the pre-processing steps (right). The accumulated absorbance intensity is represented by the summation of all spectral intensities for the regarded spectral range. Clearly, the normalization process has led to a homogenization of the dataset, while the impact of the variation between the two different datasets could be reduced.

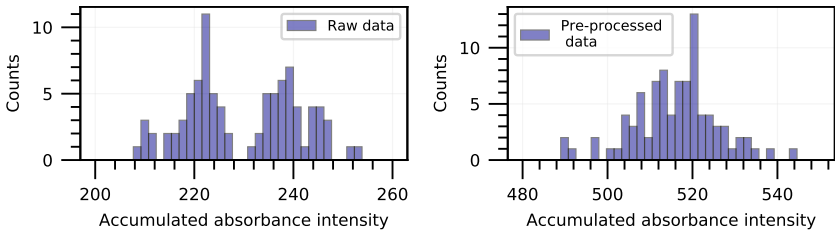

Figure 5.13: Histograms of accumulated absorbance intensity prior to the pre-processing (left) and after the pre-processing step (right)

In the second step, the signal-to-noise ratio (SNR) for an area without significant peaks was calculated. The results are presented in Figure 5.14, where the SNR is plotted versus the total counts in a histogram along with the normal distribution.

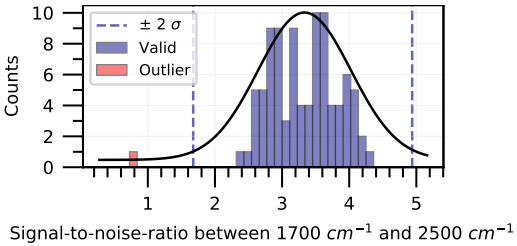

Figure 5.14: Outlier detection by analysis of the SNR

Therefore, the standard deviation was calculated in the spectral range between 1700 cm^{-1} and 2500 cm^{-1} and was divided by the corresponding spectral mean values. This approach also covers a possible deviation from CO_2 variation and excludes highly influenced specimens from further analysis. One single outlier specimen was identified in the training set and was excluded from further analysis, as can be seen in Figure 5.14.

5.3.3 Spectral Band Allocation

Equivalent to the approach used in Figure 5.5, the variation of the data is analyzed by observing the variance and spectral contribution of the single components using Figure 5.15. The highest variance can be found at a region ranging from 1090 cm^{-1} to 1110 cm^{-1}. Instead of a clear peak, an overlapped region of different features can be seen. The same observation can be made for the band around 1373 cm^{-1}. As a result, instead of peak values, single wavenumbers are chosen for further analysis.

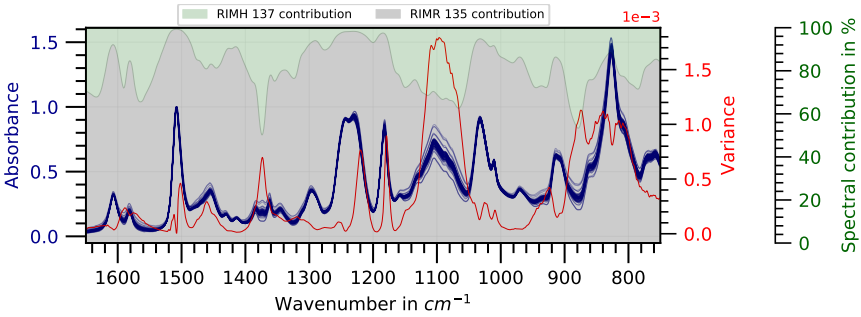

Figure 5.15: RIM-system mix and the corresponding variance in specimen direction

Figure 5-16 shows the method to extract the wavenumbers which will be used for the model. Therefore, the spectral contribution of the curing agent was multiplicated with the variance yielding a new vector that shows regions highly influenced by the curing agent component.

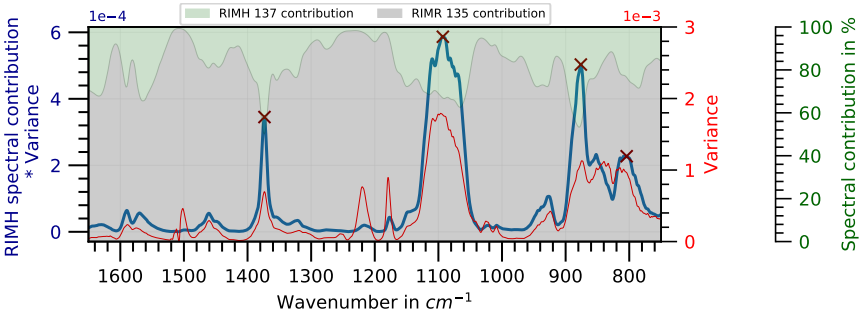

Figure 5.16: Relative variance, influenced regions by the curing agent variation

For the extraction, the resulting vector was smoothed using a Sawitzky-Golay filter with a window width of 7 and a third-order function. In addition, the peak values have been extracted by applying a threshold value of $2 \cdot 10^{-4}$ and a minimum distance between the peaks of 50 data points. The initial guess of using the bands around 1373 cm^{-1} and 1105 cm^{-1} could be confirmed by this calculation.

5.3.4 Peak-Based Linear Model

Based on the analysis in the previous section, four different wavenumber candidates were identified and the corresponding R^2 values for the linear regression models were calculated, as shown in Table 5.3.

Table 5.3: Identified spectral bands for RIM epoxy resin system mixing ratio estimation

Wavenumber [cm-1]	1373.38	1093	876.11	804.05
R^2 value	0.877	0.83	0.878	0.325

Figure 5.17 shows the results of the analysis, where the R^2 values range from 0.325 for the 804 cm^{-1} band to 0.878 for the 1373 cm^{-1} band. It can be seen that wavenumbers with a higher spectral contribution from the curing agent, such as 876 cm^{-1} and 1373 cm^{-1}, yield a higher overall correlation. Comparing the coefficient of determination of this analysis with the results of the calibration model previously presented for the LY epoxy resin system, one can see that overall, a lower coefficient of determination is observed.

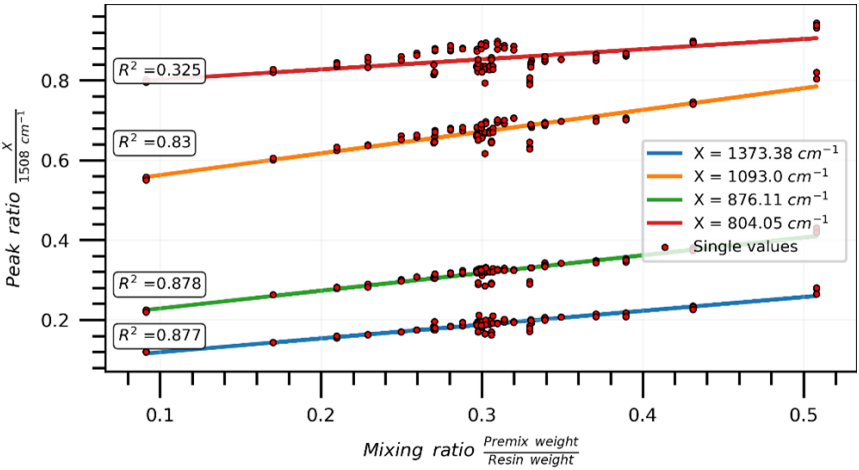

Figure 5.17: Linear model using peak value approximation by cubic function representing the major variation in the mixing spectra

5.3.5 PCA analysis

As shown in Figure 5.6, the structure of the dataset can be analyzed using PCA. This approach is applied next to further improve the model by considering the dimensionality of the data and evaluating the necessary model depth required to cover the observed variation.

Data structure

Figure 5.18 shows the principal component weights over the achieved mixing ratio for the first two principal components of the RIM epoxy resin system. Considering the first PC, the variation of the mixing ratio leads to a linear dependence which accounts for 83 % of the explained variance. In comparison, the second component clearly shows the different datasets and accounts for 12.1 % of the variance. PC 3 and PC 4 are not shown here since they do not posses any structure.

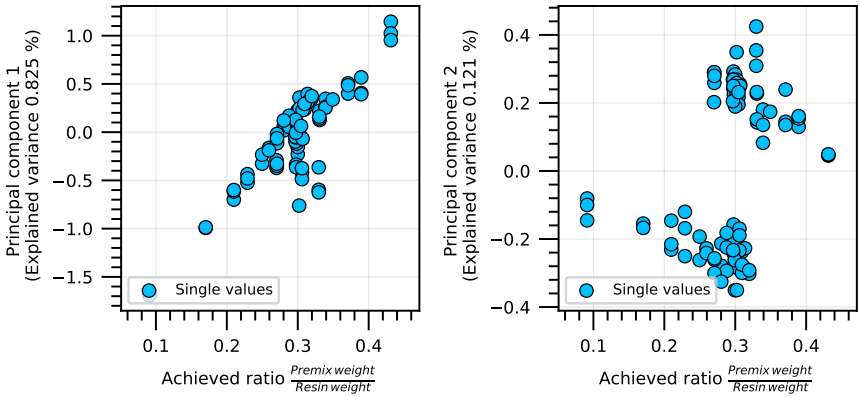

Figure 5.18: PCA of the raw data for the RIM epoxy resin system mix dataset

Based on this analysis, the first PC will be used to establish a correlation between the mixing ratio and the spectral data by applying regression analysis.

Principal component regression

In the last section, it was shown that by choosing specific spectral features, a linear model could be obtained to estimate the mixing ratio. Unfortunately, this

approach presupposes knowledge of the underlying processes and the effect on the spectral data. Using PCA, these prerequisites can be skipped by creating a solely data-based model. PCA can be seen as a multivariate extension of the feature extraction-based approach and operates on a larger set of input parameters. Figure 5.19 shows the results of the principal component regression using the first principal component.

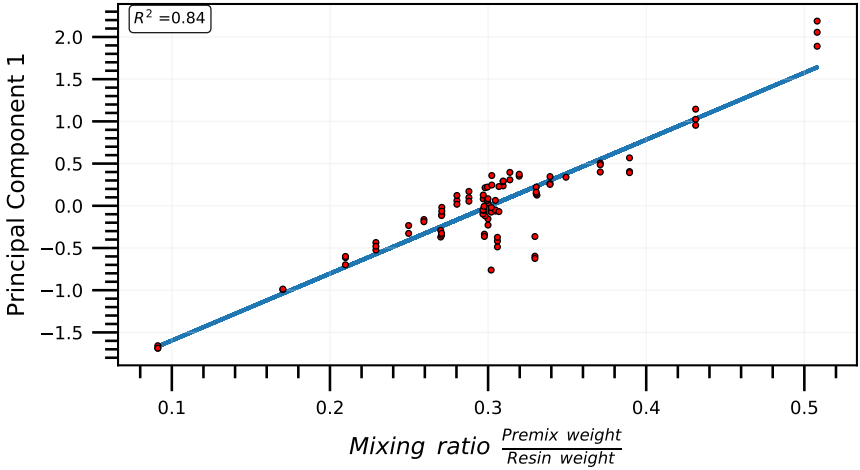

Figure 5.19: PCA-based estimation of the mixing ratio for the RIM epoxy resin system

The analysis yields a coefficient of determination of 0.84 and therefore, a lower value by comparing it to the pure analytical and feature extraction approach as presented in Section 5.3.4. The reason for the lower correlation lays within the fact that the PCA considers a significantly higher amount of spectral entries for the calculation and weights them automatically. Hence it can be concluded that the application of the PCA method does not increase the accuracy of the model but may lead to an improvement in the robustness of the prediction by being less susceptible to noise in the spectra. In general, it was shown that using PCA does not require additional pre-processing of the spectral data but also comes with lower accuracy and higher computational efforts.

6 Mechanical degradation

6.1 Introduction

6.1.1 Motivation

The mechanical behavior of thermosetting polymers and composites is well understood on the macroscopic level [37, 38]. Currently used techniques to determine the damage state after mechanical loading are based on macroscopic phenomenological observation and homogenization approaches. For engineering applications, the micromechanical structure is usually ignored since no quantification method for the stress and strain of the polymeric matrix or fibers is known to date. Nevertheless, the existing material models based on these simplifications deliver good results for the design and dimensioning of components encountered the issues using probabilistic design and intense testing. In the last section, the process of connecting spectral data with manufacturing-related metrics was introduced by creating a simple linear model. Next, a further step toward the major aim of this thesis to establish a direct connection between spectral data and mechanical properties, as described in Section 1.2, is taken. By observing the change of the material state vector under different loads, the damage evolution is tracked while identifying the dominant processes and the major underlying physical processes. In this section, the physical processes displayed in Figure 6.1 are mainly considered. Partial results of the presented work have been published in Polymer, Volume 221, 2021, Article 123585 [39].

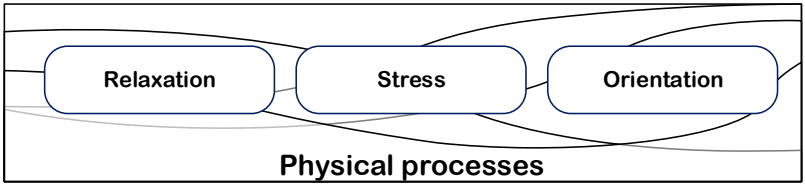

Figure 6.1: Overview of the major external processes having an influence on the material state

6.1.2 Section Outline

First, a literature review concerning molecular aspects of mechanical degradation with an emphasis on molecular relaxation, stress and orientation is provided. Second, the results of static testing and DSC analysis of the specimens are shown. Third, creep testing results and the model to estimate the molecular forces are presented. Third, the results of cyclic testing confirming the model and reversibility of the approach are given.

6.1.3 Literature review

In the following literature review section, the major previous work on the topic of mechanical degradation, plasticity and current approaches to explain these processes on the molecular level are presented.

General Idea for Tracking of Mechanical Degradation

In this section, the micromechanical concepts of state variation due to mechanical loading are introduced. The basis for the section is the observation that mechanical loading can lead to a variation of the material state of a TSP and as a consequence, the residual mechanical properties are changed. It is assumed that these material state and residual mechanical property changes are somehow connected to a change in the underlying molecular structure. If that is the case, it should be measurable using the proposed FTIR approach, assuming sufficient sensitivity can be achieved. Until now, such an approach to derive a quantifiable material state of TSPs has not yet been presented.

Damage Evolution in Thermosets

The deformation behavior of polymers is highly temperature and test condition-dependent. While thermoplastic polymers consist of long molecules forming an entanglement network allowing reversible plastic deformation by chain-slipping mechanisms due to the reduction of the entanglement intensity, this deformation mechanism is not available for TSPs. Since TSPs are made of short molecules cross-linked by covalent bonds forming a three-dimensional polymeric network, extensive chain-slipping processes are not possible. Instead, as a result of the structure, molecular level deformation of TSPs in the elastic and visco-elastic domains is limited to small strains. The underlying physics of elastic thermoset deformation is connected to the mobility of side-groups, rotation of parts of the molecules and a change of bond lengths, respectively angles. These processes limit the elastic straining of the three-dimensional cross-linked network significantly, while overloading leads to the initiation of non-linear and irreversible processes [40]. To which extent the dissolution of bonds takes place during visco-elastic deformation is discussed controversially in the literature [41]. Most authors assume it is either not occurring at all or to a very limited, non-measurable extent.

Plasticity in Thermosetting Polymers

In general, plasticity describes a non-reversible deformation of a material that remains inherent even if the load is removed. The concept of plasticity goes along with bond breaking, local yielding and subsequent chain alignment and orientation, while the dissolution of entanglements plays a minor role [42]. Unfortunately, accurate quantification and explanation of these processes with respect to thermoset-based composite degradation are not yet available. As will be shown later, plasticity in TSP requires very special conditions and geometric configurations. The key to studying the plasticity of TSPs is to prevent brittle fracture by the design of the experiment. The inherent susceptibility of TSPs to fracture at flaws and surface defects makes this task especially difficult. So far, the plasticity of thermosetting polymers in literature has been limited to the concept of plastic process zones at crack tips to explain crack propagation in thermosets [43]. The crack propagation process itself in thermosets was described to underlie a stick/slip process rather than continuous and stable, as observed in thermoplastics [41]. On this scale, the amorphous epoxy resin can

no longer be considered homogeneous but rather show heterogeneous deformation mechanisms [41]. In fact, further examples will be quoted next, showing that plasticity in epoxy resins is not unusual but rather requires specific stress and loading situations. The situation becomes more complex if temperature considerations are in place. If the temperature is approaching the glass transition temperature, the brittle behavior switches toward ductility [44]. According to Kinloch, the crack propagation process in epoxy resins shows a "slip-stick" behavior, while thermoplastic polymers undergo a rather continuous crack propagation [41]. However, statistical flaw distribution and plasticity limited to crack tips represent an oversimplification of the mechanical situation for the micromechanical specimens.

Shear-Yielding

The shear bands represent a special form of plastic deformation where a broad deformation zone can be observed. Shear bands usually develop under an angle of 45° to the loading direction, corresponding to the maximum shear stress direction [42]. In the previous section, the special conditions for epoxy plasticity were presented. In most quoted cases, the plasticity goes along with local stress concentration. At the same time, shear-yielding can be achieved by pure shear loading. A study performed by Fiedler et al. shows that under shear loads, the epoxy strain can achieve values beyond 60 % [45]. On the molecular level, shear bands are reported to be connected with collective molecular alignment and free volume rearrangement [46–48].

The Role of Specimen Size

A significant difference in the behavior of the matrix in composites compared to macroscopic specimens is observed [41]. Previous studies have shown a highly size-dependent brittleness of materials in general [49–52]. This is also true for epoxy-based polymers in case the specimen volume is sufficiently small. In this case, the epoxy resin can undergo significant plastic deformation and yielding even below Tg [6, 53, 54]. This effect is not limited to pure epoxy specimens but can also be observed in fiber and nanoparticle-reinforced plastics. Due to the presence of nanoparticles in epoxy resins, a change in the stress distribution is observed, leading to higher global yielding and significant local plasticity

[55, 56]. Hopmann et al. confirmed this observation for single fiber model specimens, showing that already the presence of single fibers can lead to highly stressed areas inducing significant plastic deformation [57]. A study conducted by Hobbiebrunken analyzing plasticity in small epoxy volumes in fiber-reinforced composites found that these small TSP volumes also undergo comparable plastic deformation when loaded [58]. Hence, one can summarize if fracture events can be delayed by geometry or the absence of flaws, increased local stress concentrations are capable of forcing the epoxy resin to undergo plastic deformation. Classic concepts of thermoset deformation fail to explain such behavior since they cannot explain excessive deformation in a 3D-crosslinked polymer [41].

Molecular Relaxation

Structural relaxation plays an extensive role in the deformation process. Thermosets are manufactured by curing a TSP with a curing agent by chemical reaction, attaining a three-dimensional cross-linked polymer network. The transition from the rubbery state to a glassy state goes along with a cross-linking chemical reaction, continually reducing the distance between the molecules. At the glass transition temperature, the molecular mobility is significantly reduced, leading to a residual free volume and a non-equilibrium amorphous state. While the molecular backbone is almost entirely locked-in, the mobility of side groups and local motions of molecules is still possible [59, 60]. With time and temperature, the TSP tends to further decrease the free volume and excess enthalpy by a relaxation process called physical aging. Physical aging describes a process where the polymeric network converges toward a lower enthalpy and entropy state. As a result, an increase in intermolecular forces due to a reduction of the distance between the polymeric chains occurs [61]. Besides, the brittleness of the polymer increases and the fracture toughness decreases [62]. The process is known to be reversible by resetting the locked-in state with elevated temperatures. The effect can be seen using Differential Scanning Calorimetry (DSC) measurements, where an endothermal peak occurs below the glass transition temperature [63]. During the DSC measurement, energy is consumed in order to restore the corresponding equilibrium state in relation to the temperature. The onset of the resetting process is reported to be found at approximately 20 °C below the Tg [63, 64]. The same effect was observed by analyzing the constricted area of the specimens tested in tensile loading, indicating changes in the polymer's energetic states [6].

Molecular Stress

When a force is applied to a polymer, the external load is distributed among the molecular bonds leading to stress of these bonds. In the early '70s, several authors addressing the load distribution in molecular bonds showed that the backbone molecules of polymers are not uniformly loaded. Instead, the bond load underlies a statistical distribution where single bonds may be overloaded while the majority of the bonds are strained to a lower extent [65–69]. Hence, during extensive plastic deformation of a 3D-crosslinked TSP, the dissociation of these overloaded bonds would be expected. These ruptures in the backbone chain of the polymer enable additional degrees of freedom for the polymeric chains. A previous study by Seitz quantifying bond scission events during fracture revealed that the number of affected bonds usually remains below 1 % [70]. A theoretical approach to quantifying the bond scission events has also been proposed by Zhurkov et al. [71], stating that according to the kinetic concept of fracture, the probability of bond rupture can be estimated from the temperature and stress of the polymer. Two different approaches have been proposed in the past to quantify chain scission events directly during the event or indirectly by measuring residual molecular components. One of the direct methods is represented by electron paramagnetic resonance involving the measurement of free radicals, which exist for a short time after the breaking event [72]. Alternatively, it is possible to measure the residual polymeric components and end groups indirectly by spectroscopy methods [73, 74]. Instead of measuring the number of polymeric chain scissions, several authors have proposed methods to estimate the molecular stress magnitude and distribution. A study by Ferraro et al. revealed a correlation between the variation of atomic bond length and the shift of the vibration frequency measurable by infrared spectroscopy [75]. Tensile stress induces a shift toward lower frequency and therefore, lower wavenumbers due to a change of the force on the atomic bonds, valence angles and internal-rotation angles [65, 76]. These authors also confirmed that the shift is mainly affecting the backbone bonds such as C-C at $975\,\mathrm{cm}^{-1}$ or $1060\,\mathrm{cm}^{-1}$, while side-group bonds usually remain unchanged. Salmen and Bergström further elaborated on these insights, showing that the $C-O-C$ deformation vibration of cellulose located at $1160\,\mathrm{cm}^{-1}$ also undergoes a peak shift upon loading [77]. The intensity of the peak shift highly depends on the polymer orientation since orientated polymers show lower standard deviation and therefore, sharper peaks compared to amorphous polymers. A recent study by Sammon et al. confirms

these observations by atomistic simulations. The majority of the experiments so far have been performed using thin films analyzing the mid-infrared region [78]. Although the information density in the mid-region is higher, the extensive overlapping of the single peaks represents a challenge during analysis. Also, thin layers often show significantly different viscoelastic and plastic behavior when compared to the bulk material, as previously explained. In a previous study, it was confirmed that the NIR spectrum already contains molecular information allowing a prediction of the mechanical performance of a TSP upon thermal exposure [79]. Furthermore, a study performed by Shinzawa and Mizukado confirmed that the chain deformation of polymers could also be detected by looking at the overtones in the near-infrared spectrum by analyzing Nylon 6 films [80]. Until now, accurately resolving and quantifying the peak shift of a single bond or bond angle vibration remains challenging due to the broad character of the relevant peaks, high scattering during the measurement and a low overall shift sensitivity. Therefore, further data processing is inevitable in order to derive a quantitative model.

Molecular Orientation

The application of rheo-optical measurements can determine the orientation of polymeric chains. In amorphous polymers, the backbone chains are randomly oriented in the unloaded case. Upon the application of stress, the orientation of the chains shows a tendency to point toward the main stress direction. By measuring the absorbance of polarized infrared light, one can determine the dichroic ratio R, which indicates the bond direction and, therefore, polymer chains' orientation [81]. The physical background and basics can be found in [52, 82]. Several authors have applied the methodology by simultaneously recording the strain and the polarized absorbance to determine the orientation. Polymers undergoing significant strains, such as rubber or thermoplastics, have been used, showing high variation in the dichroic ratio [83–87]. More recently, Scherzer has published several articles on polarized infrared spectroscopy of thermosetting polymers proving that alignment effects are also measurable on epoxy resin under lower total strains [88–90]. Kataoka et al. showed that this approach could also be used for the backbone bond of cellulose-containing $C-O-C$ bonds at 1160 cm^{-1} [91].

6.1.4 Data Acquisition Process

An experimental setup allowing static and dynamic tensile tests while recording FTIR spectra in situ is used. The specimens are mounted to a DEBEN microtest 200N tensile stage and positioned in the IR beam, as illustrated in Figure 2.2. The IR light is transmitted orthogonally to the specimen surface and at the same time, orthogonal to the load direction. The quasi-static tensile tests were performed using a velocity of 1 mm/s while the creep and cyclic experiments were conducted controlling the force. The FTIR spectra were acquired using a Tensor 2 FTIR spectrometer manufactured by the Bruker Corporation. The spectral data acquisition was performed in transmission mode in the range of 500 cm^{-1} to 6500 cm^{-1} using a spectral resolution of 2 cm^{-1}. To achieve a more accurate tracking of the spectral variation in time, the acquisition sampling number was set to one. Instead of using the OEM integrated data binning function, a moving averaging window data processing step was applied. For all tests, a torque-limited wrench key and mechanical clamping were used. All tests were performed in a temperature-controlled room at 23 ($\pm$ 2) °C and 50 ($\pm$ 10) relative humidity. Specimen quality was controlled by performing optical analysis using an EPSON V850 Pro transmission light scanner and a Gabo Eplexor 500 N DMTA to measure the Tg.

6.2 Quasi-Static Testing

The tensile tests of the initial reference (IRE) specimens showed expected stress-strain curves, while the mechanical properties lay within the range specified in the technical datasheet. During the experiment, the formation of unexpected surface irregularities was observed in the central part of the specimen immediately before fracture. As described in the literature review section, TSP is generally capable of undergoing local yielding due to stress concentration at flaws and defects prior to fracture initiation. However, the observed phenomena did not fall into this category due to a significantly larger affected area in comparison to previous studies. Nonetheless, to minimize surface-driven fracture, the roughness of the specimen side surfaces was significantly reduced by polishing by applying the previously described three-step process, as can be seen in Figure 6.2. To further quantify stress peaks and track the stress distribution during loading, in situ microscopy combined with birefringence measurements has been added to the test configuration.

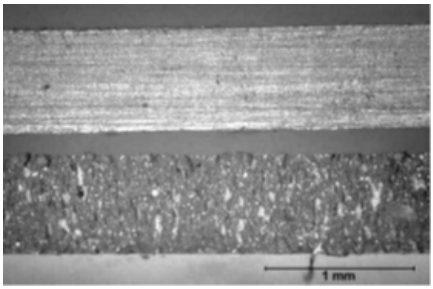

Figure 6.2: Surface comparison between IRE specimen surface (bottom) and specimen side surface after a three-step polishing process (top)

As a result, the resulting stress-strain curves have changed notably, as shown in Figure 6.3, where the black curve represents the IRE specimen. Clearly, polishing leads to a significant increase in the elongation at break value while the ultimate strength is slightly reduced and the modulus remains unchanged.

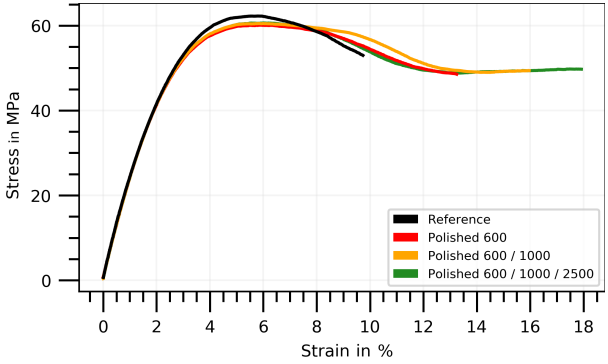

Figure 6.3: Representative stress-strain curves comparing the initial reference (black) and polished specimens (red-orange-green) after different polishing steps

Remarkably, while the IRE specimens fractured without significant cross-section reduction the polished specimens (PS) undergone a cross-section reduction forming a large visible constricted area as displayed in Figure 6.4.

Figure 6.4: Standard specimen showing the constricted area after static loading and subsequent unloading

Also, after unloading, the constricted area remained unchanged, indicating residual plastic deformation. Remarkably, the change in the experimental setup amplified the formation of the previously observed irregularities instead of preventing them. The observations indicate that also the previously observed irregularities can be attributed to extensive shear-yielding zones with shear band formation. The visible deformation is lengthwise limited to the central 20 % of the PS specimen, as can be seen in Figure 6.5.

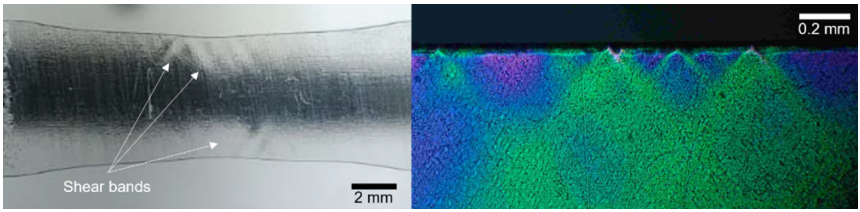

Figure 6.5: Microscopy image of the constricted zone (left) and birefringence image of the unloaded specimen (right) illustrating shear bands

It is concluded that the non-standard geometry and smooth specimen surfaces contribute to the formation of the constricted area. In contrast to previous studies, the observation also shows that the plasticity of TSP is not strictly limited to small volumes but may also occur in larger volumes under certain conditions. To date, a large-scale formation of shear bands has not been reported for TSP and is, therefore, further investigated. To gain more insight into the

structural changes of the constricted area, the energetic state is analyzed next. Therefore, one exemplary PS was unloaded once a strain of 18 % was reached and before the fracture occurred and subsequently analyzed using DSC.

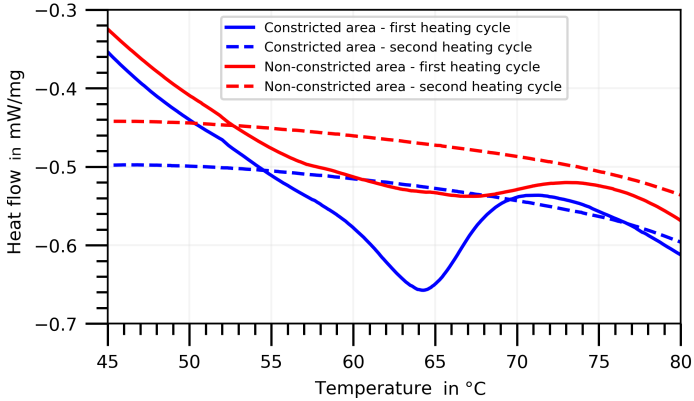

Figure 6.6: Comparison of DSC measurements for the constrained subspecimen in blue color and the non-constrained area in red color. Clearly, a relaxation peak for the constrained subspecimen can be seen, indicating endothermal behavior during heat-up. During the second heating cycle, no further difference is detected between the red and blue curves, indicating equal thermal behavior of both subspecimens

Figure 6.6 shows the resulting DSC curves comparing subspecimens extracted from the constricted areas (blue curves) with subspecimens extracted from non-constricted (NC) area indicated by red curves. For both configurations, the first heating cycle is represented by the solid line, while the dashed lines show the second heating cycle. For both subspecimens an endothermal peak can be observed in the range between 60 °C and 67 °C. While the constricted subspecimen peak shows a high intensity, the NC peak is clearly of lower intensity. Both endothermal peaks disappear during the second heating cycle, indicating a reversible energetic transition during the first cycle. However, even though the energetic analysis indicates reversibility, no recovery of the dimensions was observed if a constricted specimen was exposed to heat using the same heat cycle. One possible explanation for these DSC observations is that during shear band formation, the molecular structure undergoes a weak form of the orientation of the polymeric chains while the free volume is reduced and the intermolecular forces are increased. Above all, the observed substructure shows properties com-

monly associated with semi-crystalline areas of thermoplastic polymers. FTIR spectroscopy is applied to further analyze the chemical structure of the TSP in both areas of the specimen. First, the focus is laid on chain scission events assuming that the extensive deformation of a 3D cross-linked epoxy network has to go along with the rupture of the polymeric backbone chain. This assumption is also backed by the fact that a slightly reduced ultimate tensile strength (UTS) was observed for the PS, which may be connected with a reduction of primary bonds. Unfortunately, a statistically significant increase or decrease in functional groups indicating chain scission could not be observed. Therefore, it is hypothesized that the FTIR measurement's sensitivity is either insufficient or that the number of chain scission events during the formation of constrained areas is very limited. However, a small indication of peak-shift behavior could be found during FTIR testing even though the scatter was very high. As a consequence, a slower deformation process by applying creep tensile testing combined with in situ FTIR measurements is performed next to increase the time-driven resolution of the molecular processes involved. The main question remains why brittle fracture is suppressed by the formation of the constricted area and which role do the intermolecular and intramolecular forces play?

6.3 Creep Loading

The in situ creep testing approach is expected to provide a more in-depth insight into the deformation process by the acquisition of time-dependent mechanical and FTIR data. The spectral data will then be used to derive variables that describe the molecular state based on the peak shift approach. First, three different load levels, at 80 %, 60 % and 40 % of the ultimate tensile stress, were tested to evaluate the feasibility of the approach. As expected, a load level-dependent straining behavior is observed in Figure 6.7. The 50 MPa specimen is showing instability due to a fracture at the end of the creep curve, which is not relevant for further evaluation. Thus, the 80 % ultimate tensile stress level at 50 MPa is chosen for the initial experiments. It allows a good tracking of the molecular processes at a reasonable time frame but comes at the price of higher scatter, as will be seen later.

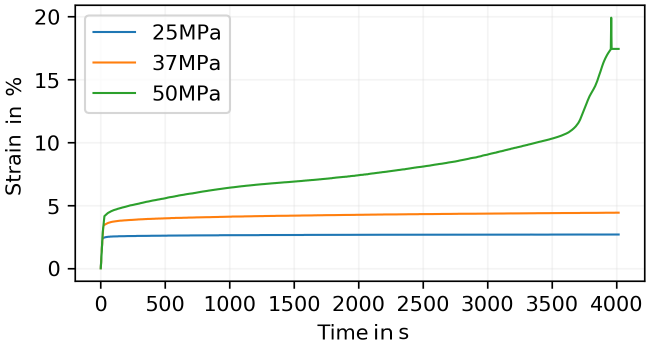

Figure 6.7: Creep loading curves for three different load levels at 25 MPa, 37 MPa and 50 MPa using the standard specimen dimensions

During the initial loading, spontaneous elastic and viscoelastic deformations lead to the straining of the specimen within the first seconds of the experiment. With advancing time, the cross-section is continually reduced due to the application of a constant load. At the same time, the stress in the analyzed area is increased accordingly. In the end, with the formation of the necking, the process is further accelerated, leading to the failure of the specimen. Generally, the observed course of the strain development is expected for TSP. However, as stated before, the necking behavior is unusual for thermosetting polymers. An explanation of this behavior may be accessible through the interpretation of changes in the intramolecular and intermolecular forces. Therefore, an attempt to quantify these forces by FTIR is performed next. First, deformation-sensitive FTIR bands are identified and the dependence on straining is evaluated. Therefore, the previously presented feature extraction process is applied and a data vector is derived. The data vector stores information about the peak positions and integral variations. It was generally found that several peaks show a shift of the derived peak wavenumber (PWN) upon loading to different extents. In fact, a wavenumber-dependent variation with progressing creep time is observed. This enables the evaluation of the connection between the PWN behavior and the molecular forces.

6.3.1 Intra-molecular forces

Observing the infrared absorbance of the ether group (see red highlighted atoms in Figure 6.8 allows an evaluation of the intramolecular forces and the backbone straining. The ether group is found at $1036\,\mathrm{cm}^{-1}$, while the first overtone is located at 2070 cm^{-1} [40].

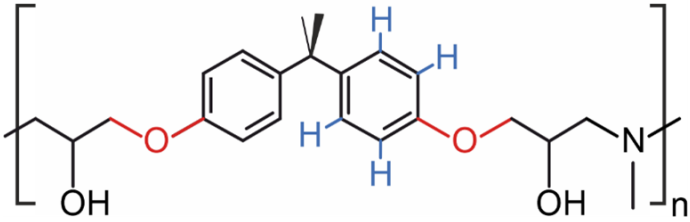

Figure 6.8: Major molecular bonds of the DGEBA polymer. The ether groups are indicated in red, while the $C-H$ bonds of the phenyl ring are shown in blue [94].

The wavenumber of the overtone peak of the ether bond ($C-O-C$) serves as an indicator for the mean molecular strain in the polymer. As a component of the backbone, this bond is directly responsible for force transmission through covalent bonds when the specimen is loaded. While the peak position can be used as a gauge for the average strain, it is expected that analyzing the integral value and the standard deviation gives access to a bond scission count with respect to a molecular stress distribution. However, the focus is put on the mean molecular stress in this work. It is found that with increasing tension on the polymer network, a shift of the ether peak toward lower wavenumbers occurs, indicating an elongation of the ether group bond length confirming previous studies [67, 69]. Figure 6.9 shows the evolution of the center of the distribution of the backbone measured by the peak shift. The peak position observed during the creep experiment illustrates a correlation with typical strain vs. time creep curves. The initial loading leads to an instantaneous drop of the wavenumber, as can be seen in the first seconds of the experiment by looking at the single measurements shown as grey dots. The Sawitzky-Golay filtering algorithm may be misleading for the initial phase of the experiment by over-smoothing the curve and not showing the immediate character of the drop. However, a fixed set of smoothing parameters was chosen, allowing good tracking over the whole experimental time. The following constant phase shows a tendency for constantly

accelerating the reduction of the PWN prior to a final drop at the end of the experiment, starting at approximately 3500 s. With increasing strain, the peak shift accelerates, indicating the development of higher average strain on the molecular bonds and increased distance between involved atoms. In the end, a second drop-like decrease is observed prior to specimen failure. Hence, the molecular strain can be observed in all three creep stages.

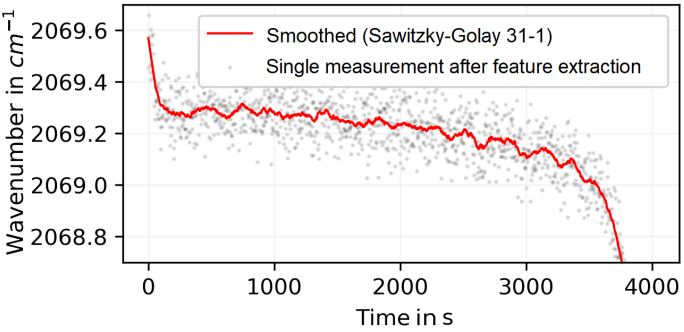

Figure 6.9: Temporal evolution of the ether bond peak shift measured by in situ FTIR spectroscopy during creep loading for 4000 seconds at a tensile stress of 50 MPa

6.3.2 Inter-molecular forces

The second observed infrared band is used to analyze the extent of the inter-molecular forces. The FTIR peak-position of $C-H$ bonds in the aromatic ring (see Figure 6.8, highlighted light blue atoms), which is assumed to be associated with more general van der Waals (vdW) interactions, is calculated and evaluated. Even though these bonds are not directly loaded during a tensile test, they are known to contribute to the load-bearing capability of the polymer. Indeed, the vdW interactions are highly distance-dependent and a small variation of the distance may already lead to a significantly higher load-bearing capacity [95]. Therefore, the location of the spectral peak is assumed not only to be connected with the distance between the chains but may also be used as an indication of the free volume and the intensity of intermolecular forces. Figure 6.10 shows the PWN of the $C-H$ bond in bending vibration at $1885\,\mathrm{cm}^{-1}$. Although the initial behavior is similar to the ether bond, a different progression is observed over time. Looking at the whole experiment, the highest variation of the cor-

responding peak positions is observed during the initial loading and the tertiary creep stage.

It is assumed that the PWN of the hydrogen bond can be seen as a measurement value for the free volume of the polymer. At the same time, it represents the load-bearing share for the polymer. In this case, the initial decrease in the PWN value could be associated with the increase in mobility due to a rising free volume. During the second phase, where a constant strain rate is observed, the PWN remains almost constant due to unchanged free volume. Upon necking, the free volume decreases and leads to a rising PWN and at the same time to a higher contribution of the intermolecular forces toward the load-bearing. This goes along with a shear-yielding phenomenon which leads to a significant reduction of the distances between the polymeric chains and also to a chain alignment. However, chain alignment has not been analyzed here, but previous studies have shown that this effect can also be observed in TSP using rheo-optical infrared spectroscopy [92].

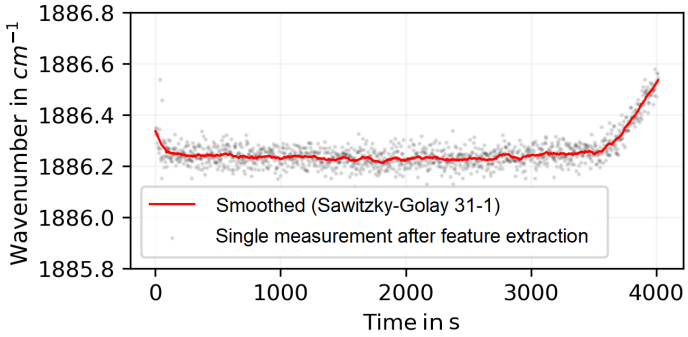

Figure 6.10: The evolution of the hydrogen bond during a creep loading for 4000 seconds at a tensile stress of 50 MPa

Even though additional spectral bands may be suitable for analysis, the choice of these peaks is based on the highest intensity and largest variation during the experiment. However, future studies with more sensitive methods and other spectral bands could contribute to a further understanding of this phenomenon.

6.3.3 Explanation of the Plasticity

Based on these results, a theory to explain the yielding behavior of the thermosetting polymer is proposed. As initially stated, the central question of this study is why a 3-dimensional cross-linked polymer is capable of undergoing extensive plastic deformation without fracture. Based on the previous observations, isolated analysis of the intramolecular and intermolecular forces is carried out while establishing a connection with load-bearing capability. As can be seen in Figure 6.9, once the specimen is loaded, a continual increase in the strain with respect to the stress of the ether bond takes place with the passing of time. Even though the bond scission events could not be quantified, it is further assumed that they take place in general. This has the effect that with increasing straining, the probability and rate of backbone bond scission increases, which would lead to a reduced number of load-bearing backbone bonds. The remaining load would then be distributed on fewer bonds leading to higher strain values and to some extent, to a chain reaction. The behavior of the $C-H$ bonds indicates that they are also subjected to external force when the external force is first applied. Therefore, intermolecular bonds take up part of the load, which also weakens them and causes the peak shift to smaller wavenumbers. The final phase shift to higher wave numbers in the tertiary creep range can be explained by the necking of the material occurring in this phase. Necking is accompanied by an increased alignment of the polymer chains, which brings the individual chains closer together. It was seen that a shear-yielding sets on, leading to reduced mobility of the polymeric groups and an increased load-bearing capability through a reduced chain distance. This alignment results in an increase in the intermolecular forces, which is reflected in the back shifting of the peak. Thus, the peak value of the hydrogen bending bond directly correlates with the distance between the polymeric chains and therefore can be viewed as an indicator of intermolecular forces. Combining the previous observations, an explanation for the yielding behavior is possible. It is suggested that the percentile contribution of the intermolecular forces during the third creep phase increases while the intramolecular forces stay constant or are slightly reduced, leading to an increased load-bearing capability of the TSP. The severity of the single bond scission event is therefore reduced, while on the macroscopic level, the crack growth is suppressed by "intercepting" crack growth and delaying fracture.

6.4 Cyclic loading

In this section, the repeatability and reproducibility of the observation are analyzed. As can be seen in Figure 6.11, the time until the third creep stage is initiated varies for the single experiments from 3500 s to 11000 s.

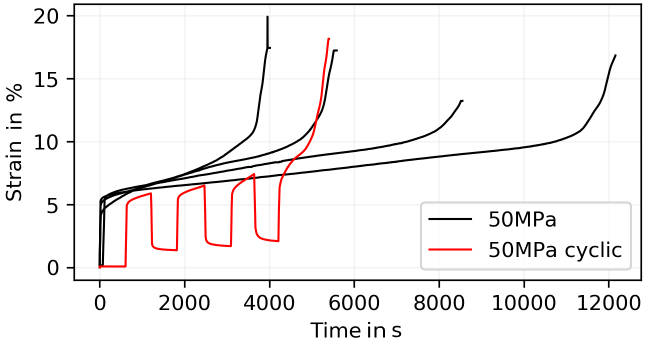

Figure 6.11: Strain evolution for cyclic (between 0 MPa and 50 MPa) tensile loading and constant tensile loading at 50 MPa. Black lines indicate different specimens showing the underlying scatter connected with this experimental setup

A possible explanation for this behavior is the high load level chosen for these experiments. It leads to high susceptibility to inaccuracies in measuring the specimen cross-section, which results in a variation of the true stresses. Furthermore, the question of reversibility may arise from the previous findings. Therefore, cyclic experiments have been performed additionally in order to confirm the observations. Even though a high variation of the time period until fracture or until the instable creep initiates is observed, the critical PWN value, which describes the point of instability initiation, is found to be stable for all experiments. Exemplary, a limit for a critical peak shift is proposed to be located at $2069.15\,\mathrm{cm}^{-1}$, as shown in Figure 6.12.

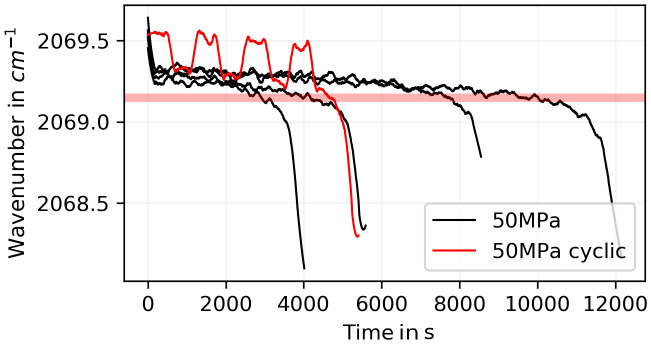

Figure 6.12: Evolution of the central peak position for the ether bond over time for different specimens. The bold light red line indicates a proposed peak value that can be used as an indicator for non-reversible plastic deformation.

Both figures also indicate that the presented method is not only limited to creep specimens but is also applicable in cyclic fatigue experiments.

In the end, the peak shift approach to predict and estimate the current material state is proposed using the peak shift factor derived from the analysis. As was shown, a clear correlation between the peak position and molecular stresses can be established using the proposed methodology. The experiments suggest that a generalization of the observations can be performed covering creep as well as fatigue experiments for epoxy resin. Furthermore, the presented results indicate that the derived value is independent of load level and duration. Therefore, a specific wavenumber can be defined as a limit value indicating the damage state of the polymer. Therefore, a catastrophic fracture event can be prevented by monitoring the development either as an NDT approach or by in situ condition monitoring. A simple model to apply the peak shift methodology of the $C-O-C$ ether stretch to estimate the material state is proposed in Figure 6.12, where a limit value of $2069\,\mathrm{cm}^{-1}$ is proposed. However, extensive further work needs to be conducted to confirm the generalization of this approach and applicability in service under all degradation influences.

7 Thermal degradation

7.1 Introduction

7.1.1 Motivation

In the last section, an approach to quantify the material state based on the intermolecular and intramolecular forces was introduced. It was shown that physical processes could be tracked using infrared spectroscopy and the underlying material properties can be estimated using FTIR data combined with pre-processing and post-processing algorithms.
In terms of the overall goal of this work to establish a holistic method to evaluate the material state of a TSP, this section contributes by focusing on chemical processes. In fact, the feasibility of extending the model to identify and quantify chemical processes is evaluated by using the example of thermal degradation (TD). It is well established in the literature that exposing materials to elevated temperatures can lead to the initiation and acceleration of physical and chemical processes. In fact, these processes usually lead to reduced material durability and therefore, are connected with thermal degradation. The initiation of these processes is usually linked to an activation energy barrier which is attributed to specific temperatures.
Until now, commonly used methods to observe thermal degradation processes rely on phenomenological observations and indirect measurements. A simple and robust method to continuously track material state changes and derive residual material properties after thermal degradation is not yet established. Therefore, to improve the degradation process understanding, a significant need for observation, identification and accurate quantification of the underlying chemical processes is present until now.
In figure 7.1, major chemical processes (CP) which are connected with thermal degradation in TSP are listed. Due to the highly complex nature of TD, this list should not be considered exhaustive but rather represents the CP analyzed in detail in this section. In general, it is barely possible to accurately cover all

chemical processes and interactions which contribute to the final material state using currently existing methods.

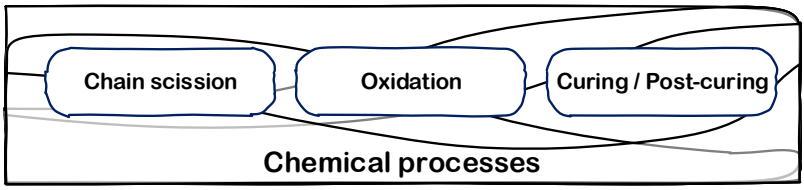

Figure 7.1: Chemical processes governing the thermal degradation

The main goal of this section is to establish a direct link between the material state and the residual mechanical properties after thermal exposure. Therefore, analytical and machine learning-based approaches are considered. Even though both approaches fulfill the same function of connecting FTIR and material property measurements, the structure and complexity of the connection significantly differ.

The analytical approach can be considered robust and computational-simple but comes with lower accuracy. It is based on the direct identification and quantification of the underlying physical and chemical processes through IR intensity measurements. These values are then used to establish a correlation with observed material properties. Additional influences not covered in the model-creation phase, e.g., moisture uptake, cannot be covered in the present application.

The machine learning approach based on artificial neural networks, on the other hand, is highly complex, has a high number of variables and is computational-intensive. However, it is considered holistic, covering all physical and chemical processes represented by FTIR data. As explained in Sections 4.5.2 and 4.5.3 this method is based on algorithms where learning from sample data is performed to derive a pattern to predict material properties. Partial results of the presented work have been published in Polymers 2019, 11(2), 363 [79].

7.1.2 Section Outline

In detail, the section is structured as follows: First, a literature review of thermal degradation in TSP with an emphasis on chemical processes is done to show how

the molecular structure of TSP is impacted in detail. Second, using the methods introduced in Section 3.2, a characterization of temperature-driven physical changes is performed. Third, the major chemical degradation processes are identified and quantified using FTIR spectroscopy, mainly looking into dehydration, chain scission and oxidation processes. Fourth, using the information on the chemical processes from the previous section, a connection with the mechanical properties is established, adding mechanical testing. Also, a preliminary study to combine this information with the Peak-Shift methodology presented in Section 6 is conducted. Finally, an approach is presented where machine learning methods are applied to predict the residual mechanical properties solely based on FTIR spectra.

7.1.3 Literature Review

In the following section, an overview of the literature concerning the thermal degradation of TSP and FTIR spectroscopy-based methods to evaluate thermal degradation is provided. So far, a considerable amount of literature has been published on the topic of the thermal degradation of TSP, separating the underlying processes into physical and chemical degradation [2, 63, 92]. Regarded individually, the physical and chemical processes leading to a change of material properties due to thermal degradation are well understood. The main weakness in state-of-the-art knowledge lays in the poor understanding of the interaction between chemical reactions and physical phenomena. Clearly, this fact can be attributed to a lack of suitable data acquisition techniques to cover all possible aspects of thermal degradation by a single measurement. In addition, the big variation in the velocity of thermal activated physical and chemical processes requires an accurate technique with high sensitivity on the one hand, but also a wide measurement range.

As was shown in Figure 3.9, the onset of the thermal degradation measured by TGA using a temperature ramp is found to be at 330 °C. In no way should this value be considered as an upper limit for operation, but rather the single physical and chemical processes have to be taken into account. For example, if a long-term static temperature exposure is considered, a significantly lower temperature already leads to continuous material property changes. On the other hand, TSP may be able to sustain temperatures above the TGA onset for short times without structural failure accompanied by structural changes in the poly-

meric network. Indeed, the complexity of thermal degradation requires extensive testing and a deep understanding of the underlying processes to determine operational limits. Therefore, in this work, a wide temperature range between up to 400 °C was chosen to account for the most relevant processes.
The impact of physical aging and chain scission on the polymeric network were covered in Section 6. Therefore, the literature review in this section is focused on oxidation and dehydration. In addition, a short overview of previous work in the area of FTIR-based methods for thermal degradation analysis is given.

Oxidation and discoloration

It was conclusively shown that the oxidized surface layer of TSP leads to embrittlement and accelerated crack formation [93]. Several studies made an attempt to quantify the depth of the oxidation-induced surface layer. Most recently, Yang et al. performed a thermal degradation study on anhydride-based epoxy resins using a combined grinding and a KBR-pellet preparation technique [94]. As a result, it was shown that for the specific resin system, oxidation was limited to the surface of the specimen and a thickness of up to 100 µm for the analyzed configuration [94]. A more advanced technique using microtoming of degraded TSP specimens and FTIR micro-spectroscopy was used by Mailhot to acquire depth profiles by extracting cross-sections [95]. The thermally degraded cross-sections revealed linearly increasing carbonyl bonds toward the surface, while an inverse pattern was observed for the ether bond concentration toward the bulk material inside the specimen. The overall depth of the oxide layer was reported to be up to 300 µm depending on exposure conditions [95]. Taking the fraction of the oxide layer into account, the reduction of the observed TSP strength cannot be explained by the presence of the oxide layer alone. Even though the oxide layer significantly contributes toward fracture through the formation of polymer cracks, additional processes in the bulk polymer are present. Studies performing thermal degradation under an inert atmosphere confirmed this by excluding oxygen and preventing surface oxidation, showing thermal degradation beyond oxidation [96]. In addition, a study by Echtermeyer and Krauklis confirmed this observation for the RIMR135/RIMH137 based epoxy system focusing on discoloration. They have shown that thermo-oxidative reactions and the formation of carbonyl groups attributed to the oxidation of TSP only represent one part of the thermal degradation process [97].

Moisture considerations

Undoubtedly, the moisture content has an influence on the molecular structure and the mechanical properties of TSP. Right after manufacturing, epoxy resin begins to absorb ambient moisture once it is demolded. According to the technical datasheet, the cured RIM-system absorbs 0.2 to 0.5 wt-% of water when exposed for seven days at ambient conditions and 23 °C [98]. Even though the water absorption process is simple in general, the molecular changes connected with the absorption and desorption processes have not yet been fully explained. This is especially true for the question of the reversibility of physical properties after drying and is still the subject of controversial discussion and ongoing research [99–102]. Considering mechanical properties, e.g., Rocha et al. have confirmed that with rising moisture content, a reduction of the ultimate tensile strength (UTS), modulus and Tg can be observed [103].
It was shown that using FTIR spectroscopy, the water content of the TSP can be tracked [104]. For the RIM-system, Krauklis et al. have shown that a calibration model can be established to determine the water content of epoxy resin using FTIR spectroscopy [105]. The main limitation of this study is that the approach does not allow a distinction between the type of water bonding. As has been previously shown by Zhou et al., water molecules in TSP can be retained as Type I by single hydrogen bonds or Type II where water molecules form multiple hydrogen bonds and are capable of contributing to the cross-linking of the TSP [102]. The impact of the different types on material properties has not been sufficiently studied yet, while Zhou found indication that Type II bonded water leads to an increase of hydrogen bonds and therefore, to an increase in mechanical performance. A study that conclusively distinguishes between drying (desorption of water molecules absorbed after manufacturing) and dehydrating (desorption of water molecules that are part of the polymeric network) has not been published yet. Also, the differentiation between free and bonded water in TSP is still not fully researched. A method presented by Hintertoisser and Salmen suggested that the broad hydrogen band can be resolved using DMA-FTIR and IR polarization, which may provide access to this question in the future [106]. As a result, the estimation of the moisture content using FTIR by tracking the hydrogen bond alone is considered insufficient to establish a correlation with mechanical properties. In contrast, additional parameters are required to build a robust model.

FTIR approaches to describe thermal degradation

Numerous authors have applied FTIR spectroscopy to establish the link between the mechanical properties of TSP and thermal exposure. Janke et al. evaluated and quantified the mechanical properties of carbon-fiber-reinforced polymers (CFRP) after thermal exposure using diffuse reflectance FTIR-spectroscopy. It was found that a correlation between flexural strength after thermal exposure and FTIR intensities for the carbonyl (1600 - 2000 cm^{-1}) and hydroxyl regions (3000 - 4000 cm^{-1}) can be established [107]. The main weakness of this study is the fact that only material close to the surface is measured and bulk internal material is not taken into account. Rein et al. [108] used an FTIR handheld device to acquire spectra of thermally degraded CFRP specimens and set the spectra in relation to mechanical properties. They extended the analysis by using a toolbox for artificial neural networks using short beam shear mechanical testing to generate labeled data for the calculation. The main limitation of Rein's study was the low resolution of the acquired spectra and the use of classification for thermal degradation, where no continuous prediction values were calculated. But instead, four classes were used to specify degradation severity. Eibl has shown a two-step approach where a model for thermal damage was created first by correlating inter-laminar shear strength of CFRP with FTIR spectra and in the second step, bigger parts can be evaluated by mapping material properties using FTIR spectra acquired in two dimensions [109]. However, this study considered damage severity and residual properties and did not allow a statement regarding the degradation history. In summary, previous studies using FTIR for thermal damage evaluation only used surface-related FTIR techniques and did not sufficiently consider changes in the bulk material.

7.2 Identification and quantification of physical changes

In this section, material changes on the macroscopic level are observed during and after thermal exposure. Therefore, TGA measurements at different temperatures are performed to quantify mass changes in air and nitrogen atmosphere. Then, specimens degraded at different temperatures, times and atmospheric conditions are presented to evaluate the color change.

In Section 7, the RIM system was solely used. It was chosen due to the beneficial peak location of the carbonyl groups indicating oxidation while preventing overlapping with the FTIR peaks from the base spectrum of the TSP.

7.2.1 Weight Variation

The weight variation study is divided into two parts. The temperature range between 50 °C and 90 °C was observed for 10 hours to evaluate the weight behavior in the Tg region and 150 °C to 400 °C to observe high-temperature changes.

Temperature in Tg Range

Prior to testing, all specimens (as shown in Figure 3.3) were conditioned as described in Section 3.1.4. In contrast to the standard time, the conditioning was extended to 10 days until full equilibrium was reached. To determine the true water content, reference specimens were dried for 96 h in a vacuum oven at 50 °C and a pressure of 5 mbar. The results have shown that the reference weight increased by 1.2 % due to moisture uptake after manufacturing and full conditioning. Nonetheless, this value may be inaccurate since it does not account for the possible loss of volatiles during the drying process. Therefore, the true absorbed ambient moisture content of the reference specimens may be lower. In order to reduce the possible impact of lost volatiles and not to create an artificial condition of the specimens, after manufacturing, all tested specimens were only conditioned at standard atmosphere at 23 °C and 50 % RH without previous drying. Next, the mass change over time at moderate temperatures is analyzed using TGA experiments. All experiments were conducted using an initial constant heat-up rate of 10 °C/min starting at a temperature of 23 °C. As expected, Figure 7.2 shows that thermal exposure leads to mass loss over time, while higher temperatures lead to a larger gradient and faster mass loss. Within the 10 hours, convergence toward a relative mass equilibrium is observed for all temperatures and both atmospheres. In the air atmosphere, thermal exposure at 50 °C and 70 °C leads to a weight loss of 0.93 %, respectively, 1.23 %. In the nitrogen atmosphere, the mass loss is within a similar range, with 1.09 % for the 50 °C specimen and 1.19 % for the 70 °C specimen. It is assumed that these weight changes can be attributed to drying and loss of volatiles of the TSP. Remarkably, the weight-loss behavior above Tg is different. Even though for the first 1-2 hours, the specimens at 80 °C and 90 °C showed a higher initial mass loss gradient, as expected, the final values deviated from expectation. It is observed that for both ambient conditions, the mass-loss process is stopped or even reversed. Assuming the dehydration process is ongoing as expected, it is suggested that an additional overlapping mass gain process is in place. Since this effect occurs in the air as well as in the nitrogen atmosphere, this process

is not oxidation-driven, rather, nitrogen seems to promote this process when comparing the 90 °C specimens. This observation needs further investigation once the chemical processes have been fully disclosed.

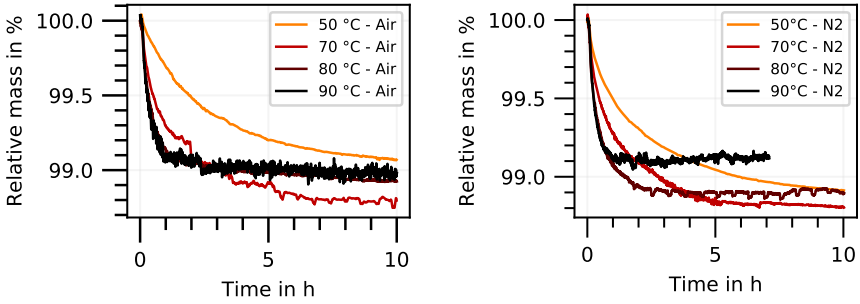

Figure 7.2: Weight changes in the range close to the Tg during thermal exposure for standard (left) and nitrogen (right) atmosphere

Elevated Temperature

In this section, the effect of elevated temperatures on mass loss behavior is analyzed using an exposure time of 2 hours. If the temperature is further increased, the relative mass loss ratio significantly increases, as can be seen in Figure 7.3. It is expected that in addition to the dehydration processes shown in the previous section, new processes set on. While the 150 °C setup leads to changes of a few percent within the experiment time, all specimens at temperatures above 150 °C show rapid weight loss. After the experiment, it was found that all specimens above 250 °C have fully disintegrated for both atmospheric conditions. Hence 350 °C in the air atmosphere and 300 °C in the nitrogen atmosphere lead to the full destruction of TSP. This result is expected taking the mass loss values into account, e.g., the 350 °C specimen in standard atmosphere loses 71.6 % of its weight after 2 hours, while the nitrogen specimen undergoes a mass loss of 85.1 %. As expected, comparing the 250 °C specimen in the standard atmosphere with the 250 °C specimen in the nitrogen atmosphere, it can be seen that an oxidation process sets on, leading to a faster degradation process. However, the total mass loss at 350 °C is higher for the nitrogen atmosphere in comparison to the air atmosphere, which cannot be currently explained. Overall, a variety of physical and chemical processes play a role in the degradation processes, which needs to be further analyzed.

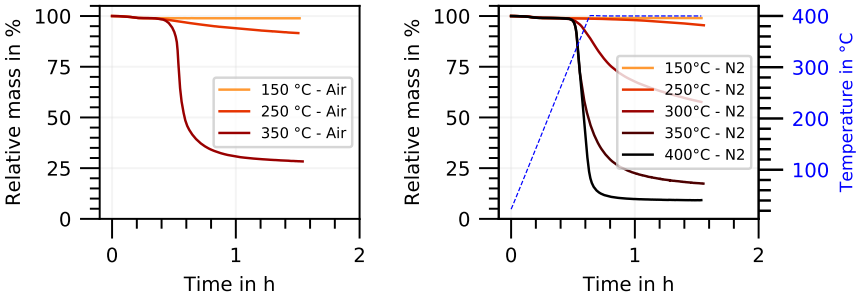

Figure 7.3: Weight change behavior of high temperature exposure for standard (left) and nitrogen (right) atmosphere

7.2.2 Discoloration

In addition to weight variation, thermal exposure leads to a change in the outward appearance of TSP. To analyze this effect, standard specimens have been exposed to elevated temperatures in a range from 50 °C to 150 °C for 24 to 72 hours in a standard air atmosphere. Moreover, additional specimens under vacuum and nitrogen have also been exposed to thermal exposure at 150 °C for 72 hours. A square area was extracted from the pictures of each specimen for comparison. As a result, a change in the color of the specimens can be observed, as illustrated in Figure 7.4. For direct comparison, a circle was added to the center of each specimen using the reference picture. Furthermore, for the 150 °C and 72 h configurations, the 150 °C standard atmosphere specimen coloration was additionally added.

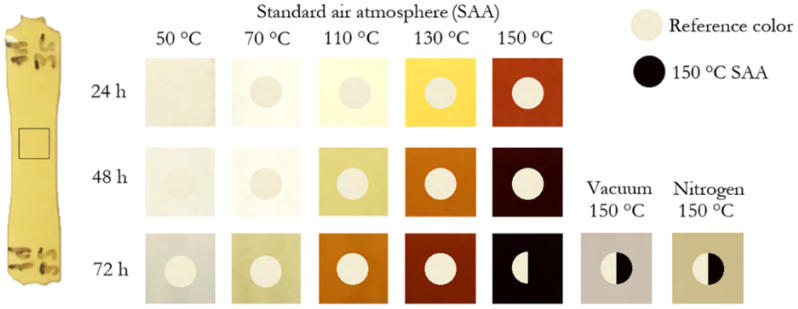

Figure 7.4: The effect of thermal degradation on the color of the RIM-system specimens with rising temperature and time in standard air atmosphere

As expected, in general, with higher temperature and thermal exposure time, the specimens became darker, changing from transparent to yellow, brown and finally to black, as previously reported in the literature [23]. Remarkably, it can be observed that specimens exposed to 70 °C undergo an opposite change of the color first, showing higher transparency for a 24 and 48 h exposure time when compared to 50 °C specimens. This observation confirms the presence of several active processes, as described in the previous section. Looking into the 150 °C specimen, it can be clearly seen that the nitrogen and vacuum atmosphere lead to a reduced change of the color when compared to the standard ambient atmospheric (SAA) conditions. Nonetheless, a shift toward a brown color in comparison to the reference specimen is still observed.
The change in color is known to be connected with a variety of thermo-oxidative processes and mechanisms under the presence of oxygen [99]. In epoxy resin, mainly a carbonyl formation by the separation of the hydrogen atom of the ether bond was suggested [110]. However, the presented results indicate that the change of the color in vacuum and nitrogen atmosphere must be connected with additional mechanisms, e.g., chain scission or internal oxidation, as previously reported [111].

7.3 Identification and quantification of the chemical processes

Now that an overview of the impact of thermal exposure on the physical properties of the RIM-system has been provided, the underlying chemical processes are analyzed by looking into the molecular changes using FTIR. A temperature range between 130 °C and 200 °C is chosen to be able to observe these chemical processes in a reasonable time frame. As explained in the previous section, experiments using a temperature above 250 °C are unreasonable since it leads to very fast degradation and is outside practical application toward the goal of material state estimation. To maximize the accuracy of the analysis, the MIR band and data acquisition in transmission mode were chosen. Hence, the highest possible IR information density and linearity of the absorbance enable precise quantification of the molecular species and their changes. Though, to obtain a fully resolved MIR spectrum, a specimen thickness of 25 to 30 µm has to be used for the RIM-system. Unfortunately, this results in excessive specimen preparation efforts and barely allows mechanical testing due to the extensive susceptibility to fracture through irregularities at the surface and challenges in

clamping. Conducted mechanical testing has shown that the single tensile tests have been of no value due to significant scatter. Therefore, the study in this section is limited to the observation of the variation of molecular species.

An overview of the spectral information obtained by this setup is shown in Figure 7.5. A qualitative FTIR spectrum of the reference specimen after conditioning in the standard atmosphere is displayed in blue, while a thermal degraded (3 h at 200 °C) specimen spectrum is shown in red. To provide a comprehensive overview, the spectra have been normalized using the aromatic peak at 1608 cm^{-1} and have been shifted along the y-axis. As can be seen, thermal exposure leads to a variation of the FTIR spectrum in various spectral regions. Depending on the spectral range, the intensity increases, decreases or remains constant. An increasing absorption intensity is especially found for the carbonyl bonds ($C = O$) located at 1656 cm^{-1} and 1727 cm^{-1}. All aromatic bands located at 830 cm^{-1}, 1510 cm^{-1}, and 1610 cm^{-1} show a comparable behavior and remain widely unchanged. This observation also justifies the usage of these bands as a reference for normalization. In contrast, a reduction in the intensity can be found for several other spectral bands. Between 3000 cm^{-1} and 3600 cm^{-1} the hydroxyl band undergoes an intensity reduction along with a slight shift toward lower wavenumbers. In addition, the decreased intensity was also found for the ether bonds at 1250 cm^{-1} and 1039 cm^{-1} and the triple peak between 2800 and 2960 representing the CH_2 and CH_3 bonds.

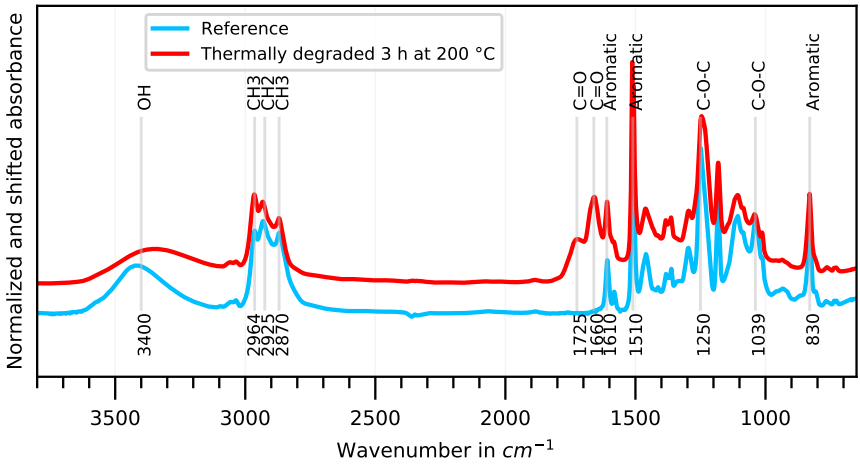

Figure 7.5: Comparison of the MIR spectra of the reference RIM specimen with the degraded specimen after thermal exposure at 200 °C for 3 hours

The quantification of the molecular species is performed using the intensity ratio, as shown in Equation 7.1. The peak ratio is calculated by the extracted observed peak value (e.g., at $1250\,\mathrm{cm}^{-1}$) divided by the closest aromatic reference peak, e.g., at $1610\,\mathrm{cm}^{-1}$ or $830\,\mathrm{cm}^{-1}$.

$$Peakratio = \frac{I_{observed}}{I_{Reference}} = \frac{I_{1250}}{I_{1610}} \tag{7.1}$$

For all following graphs showing the variation of the spectral absorbance, the exposure time in hours is depicted along the x-axis, while the peak ratio, respectively the peak wavenumber, is found along the y-axis. Every peak ratio data point represents an absorbance intensity or a peak ratio value calculated by equation 7.1. A detailed description of the spectral changes of the molecular groups is provided next using the exposure times quoted in Table 7.1. In addition to the quantification of the molecular species, the changes of the PWN are provided, where reasonable, applying the approach presented in Section 6.

Table 7.1: Times and temperatures of thermal exposure for the film specimens

Temperature [°C]	Exposure Times [h]
23 (Reference)	0
130	4, 8, 22, 26, 30
150	1, 2, 3, 4, 8, 22, 26, 30
180	1, 2, 3, 4,
200	1, 2, 3

7.3.1 Carbonyl Group

First, the oxidation process is observed by quantifying the formation of the carbonyl groups represented by the peaks at $1656\,\mathrm{cm}^{-1}$ and $1725\,\mathrm{cm}^{-1}$. The normalized absorbance intensities are displayed in Figure 7.6, where it can be seen that both peaks contain similar information. The reason for this behavior is that they represent the identical underlying molecular bond type. Both spectral bands are known to form due to thermo-oxidative reactions, as described in Section 7.1.3. In order to choose a spectral band for oxidation quantification, a trade-off between SNR and possible interference from overlapping should be taken into account. Comparing both carbonyl peaks, it can be seen that the

1656 cm^{-1} peak undergoes a more intense change leading to the formation of a larger peak area in comparison to the 1727 cm^{-1} peak leading to a higher SNR. However, the close proximity of the 1656 cm^{-1} peak to the reference peak at 1608 cm^{-1} may be a source of interference and may impact a quantitative analysis.

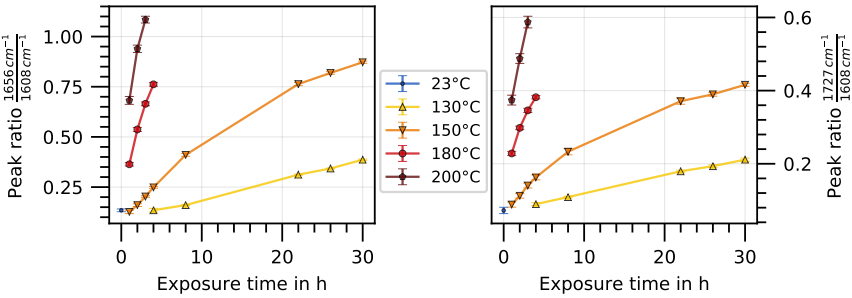

Figure 7.6: Development of the peak ratios for carbonyl bonds at different temperatures and times

Clearly, a strict dependence between the peak ratio and the time and temperature can be found for both carbonyl peaks. The oxidation intensities for 1 hour at 150 °C and 4 hours at 130 °C are comparable with the reference specimen indicating slow oxidation initiation. A weak tendency for convergence and saturation can be seen for all specimens below 150 °C, though it is not reached in the presented time frame. It is expected that due to the high surface-to-volume fraction, significantly faster oxidation of the analyzed specimen takes place, which may not be representative in extent for composites or bulk specimens. As a result, it can be stated that both peaks are suitable for determining the oxidation extent of the surface of the RIM-system and that oxidation initiation starts at least at 130 °C. As reported in the literature, the formation of radicals involved in the oxidation process may also have an effect on the chain scission processes, which should be examined in detail in the future.

7.3.2 Hydroxyl Group

A further major spectral variation can be found at the hydroxyl band around 3400 cm^{-1}. Figure 7.7 shows the peak intensity ratio on the left side and the peak shift on the right side. In general, a reduction of the peak intensity and

a peak shift toward lower wavenumbers are observed after thermal exposure of the specimens. Clearly, the reduced peak ratio indicates a loss of hydrogen bonds in the TSP, indicating a dehydration process due to a loss of bonded water, respectively, a loss of free water. The hydroxyl band is known to overlap with secondary amines located at 3297 cm^{-1}, which may also play a role in the reduction of the peak ratio intensity.

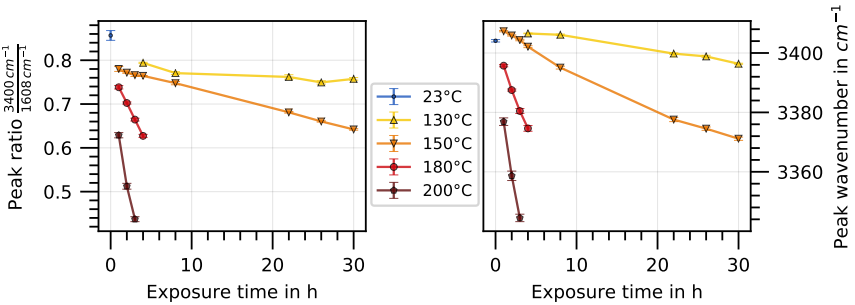

Figure 7.7: Development of the 3400 cm^{-1} bond intensities at different temperatures and times (left) and the peak shift of the corresponding peak

In contrast to the oxidation process, which sets on at higher temperatures and times, a step decrease response of the $O-H$-bond PR sets on directly for all specimens, as can be seen in Figure 7.7 (left). A reduction of the peak ratio when compared to the initial peak ratio of 0.87 can be seen for all tested specimens to at least a value of 0.8. This indicates that the drying process is nearly completed for the 130 °C test condition after 4 hours. Looking into the 130 °C curve, a tendency toward convergence of the peak ratio is found at a PR of 0.77. This indicates that an equilibrium hydrogen bond content of the corresponding temperature was reached. Assuming 130 °C is sufficient to dry the specimen, which is in line with literature where values of 50-60 °C are reported as sufficient, the data of 150 °C, 180 °C and 200 °C indicate that at these temperatures, additional processes are in place which lead to a loss of hydrogen bonds, presumably which are part of the polymeric network and not absorbed water. This also confirms the assumption made in Section 7.2.1 that additional processes have to be in place, which are now identified as the loss of hydrogen bonds.

A peak shift toward lower wavenumbers is observed, indicating reduced mobility of the hydroxyl group and a reduction of the free volume. An exemption can be found for short exposure times and lower temperatures where an increasing

PWN is observed, indicating increasing molecular mobility, which may be connected with the previously described moisture desorption. Another possibility is that the peak shift of the hydrogen bonds is connected with a partial intensity reduction of the broad $O-H$-band or the underlying $N-H$ band. The convergence of the 130 °C peak ratios indicates that further ongoing changes in the molecular structure are also present for the 130 °C specimens. The overlap with the nitrogen bond may influence this evaluation and further studies have to be performed in order to fully understand the peak shift behavior.

7.3.3 Ether Group

To allow a statement regarding the chain scission events, the ether bond located at 1039 cm^{-1} was chosen. As stated in the literature review section, the 1039 cm^{-1} peak is associated with the aromatic ether and is part of the polymeric backbone. A second ether bond located at 1250 cm^{-1} can also be found. However, it is not usable due to intensity-limited non-linear behavior. Figure 7.8 shows the intensity of the 1039 cm^{-1} band on the left side, while the corresponding peak shift is depicted on the right side of the figure. The peak ratio was calculated using the aromatic reference at 1040 cm^{-1}, while no further data processing apart from feature extraction was performed.

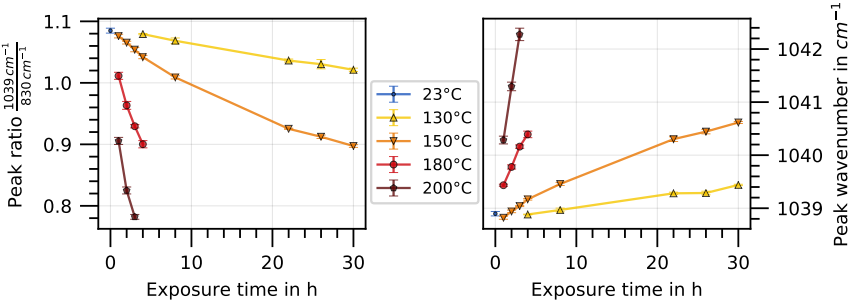

Figure 7.8: Development of the 1039 cm^{-1} ether bond intensities at different temperatures and times (left) and the peak shift of the corresponding peak

As can be seen, the peak intensity ratio is decreasing with rising exposure time and temperature, indicating progressing chain scission. Looking at Figure 7.8 (left), a slight tendency to convergence can be found, though the chosen time frame does not allow a clear statement regarding the final values for time versus

infinity. On the right side of Figure 7.8, the peak shift behavior with exposure time is shown. In Section 6.3.1, it was shown that a decrease in the PWN is associated with increased stress. Here, the opposite effect indicates decreasing mean backbone stress of the polymeric network. Combining these observations, it is concluded that a possible explanation for this behavior is the reduction of cross-linking through chain scission leading to stress reduction of ether bonds. The effect of this observation on the mechanical properties will be analyzed in the next subsection using the corresponding overtone.

7.3.4 Methylene and Ethylene Groups

Looking at the IR band between 2800 cm^{-1} and 2960 cm^{-1} a strict decrease of all three single peaks can be observed. Therefore, a relative comparison of the peak behavior of both CH_2 peaks in comparison to the CH_3 peak was performed, as can be seen in Figure 7.9. While the 2870 cm^{-1} peak ratio shows a decreasing pattern the 2964 cm^{-1} peak increases.

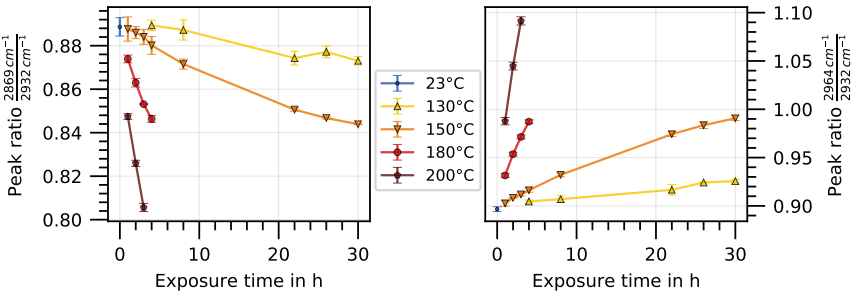

Figure 7.9: Development of the ethylene groups in relation to the methylene peaks at different temperatures for the 2869 cm^{-1} peak (left) and the 2964 cm^{-1} peak

This observation confirms the results from Section 7.3.3, confirming that the bond scission event may also be tracked by CH_2 to CH_3 rearrangement. However, the different behavior of the single CH_3 peaks indicates a different behavior for two different molecular species and needs further research in the future with a wider experimental basis.

7.4 Correlation between mechanical properties and FTIR spectra

7.4.1 Mechanical properties

In the last sections, it was shown that using film specimens, the molecular changes after thermal exposure can be identified and quantified using FTIR spectroscopy. Next, the impact of thermal exposure on mechanical properties is analyzed and correlated with these observations.
Therefore, dogbone-shaped RIM-system specimens, as shown in Figure 3.3, have been prepared using the standard procedure described in Section 3.1.3. Figure 7.9 shows a typical FTIR spectrum of the 0.5 mm thick specimen after thermal exposure for the MIR and NIR region. Due to the thickness of the specimen, the spectral bands used to identify molecular changes, as shown in the previous section, can no longer be used due to the reduced transmissivity of the specimens. Instead, the results will be transferred assuming similarity between both test setups and by using overtone bands. In this section, the FTIR analysis is limited to the MIR window in the range from 1800 to 2200 cm^{-1}, as highlighted and indicated with an arrow in the Figure 7.10 is used in analogy to Section 6.

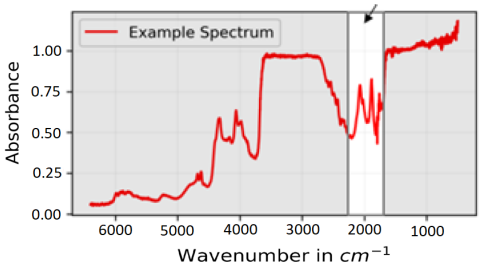

Figure 7.10: Spectral window for FTIR measurements using 0.5 mm thick specimens

After conditioning, the specimens were exposed to different temperatures and times in a convection oven in an air atmosphere. The different test configurations can be found in Table 7.2, where at least three specimens have been tested for each data point. The measurement of the mechanical properties was conducted after cool-down of the specimens and additional conditioning at standard atmosphere for 24 hours. Invalid mechanical testing results, e.g., where

specimens have undergone a slippage at the clamping have been excluded from further analysis. The results of mechanical testing are presented in Figure 7.11, showing the UTS on the left side and the strain at UTS on the right side.

Table 7.2: Times and temperatures of thermal exposure for the dogbone specimens for mechanical test-set

Temperature [°C]	Exposure Times [h]
23 (Reference)	0
70	24, 48, 120, 168
90	24, 72, 168
110	24, 48, 168
130	24, 48, 72
150	24, 48, 72

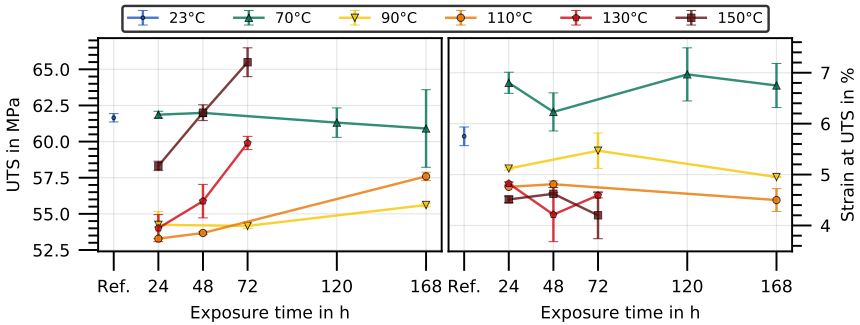

Figure 7.11: UTS (left) and strain at UTS (right) of the dogbone specimens after thermal exposure in air atmosphere

In general, the results show that for short exposure time with rising exposure temperature, a tendency toward a reduction of the UTS and a decrease of the strain at UTS is observed. An inversion of this tendency is observed to set on with a specific temperature with increasing time. These results indicate that at least two different mechanisms are contributing to the change of UTS values in TSP after thermal exposure.

In Figure 7.11 (left), it can be seen that initially, presumably, a time-independent temperature-driven mechanism leads to a decrease in the UTS value. The second time-dependent mechanism is assumed to set on above a specific temperature,

presumably around 100 °C, which significantly influences the UTS with rising temperature and time. Looking at the strain at UTS, an increase of the value is found for all times at 70 °C thermal exposure. A further increase of the temperature, starting with 90 °C leads to a strict decrease of the strain at UTS values. To further evaluate the different mechanical behavior, the stress-strain curves of the specimens are analyzed next. Figure 7.12 shows representative stress-strain curves for three specimens of each configuration after 24 h exposure time. Each stress value was calculated based on the initial cross-section after standard conditioning. In Figure 7.12, the UTS values are indicated using circles with different colors, while the black symbols indicate the corresponding breaking points.

Exemplary the percental changes of the UTS for the 24 h exposure time are shown in Table 7.3. E.g., for the 90 °C thermal exposure the mean UTS decreased by 12 % from 61.65 (σ= 0.29) MPa to 54,24 MPa (σ= 0,93), while the mean strain at UTS decreased by 11 % from 5.75 % (σ= 0.18) to 5,12 % (σ= 0.03).

Table 7.3: UTS reduction for 24 h thermal exposure at elevated temperatures

Temperature [°C]	UTS change	Strain at UTS change
70	0 %	18 %
90	-12 %	-11 %
110	-14 %	-17 %
130	-12 %	-16 %
150	-5 %	-22 %

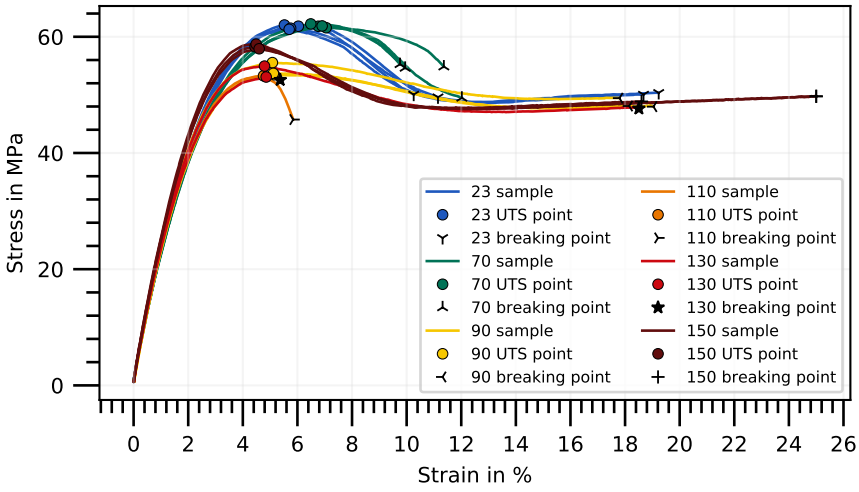

Figure 7.12: Comparison of the reference specimen with the thermally exposed specimen after 24 h exposure time at different temperatures in standard air atmosphere

Several physical and chemical processes may be responsible for this behavior. Using these results, a clear correlation of the specific molecular phenomena with the observed mechanical changes cannot be done yet. Therefore, further analysis is performed with a focus on surface oxidation and intermolecular and intramolecular forces next.

7.4.2 Surface oxidation

An additional dataset is used next to confirm the impact of oxidation on the reduced strain at break values observed in the previous section, as presented in the literature review section by several authors. Therefore standard specimens have been exposed to an elevated temperature at 150 °C in ambient air, nitrogen atmosphere and in vacuum conditions at one mbar using a Memmert VO 400 vacuum chamber. To increase the impact of oxidation and the variation between the datasets, the specimens have not been polished but instead have been exposed to elevated temperature directly after the milling process. It is assumed that this specimen processing leads to accelerated crack formation. A comparison of the surfaces can be seen in Figure 6.2. The tensile tests have been performed directly after thermal exposure and subsequent cool-down to room temperature.

The FTIR peak evaluation of the carbonyl groups at 1727 cm^{-1} reveals that the air specimens have undergone significant oxidation where the FTIR signal was saturated, not allowing quantification. Comparing the nitrogen atmosphere specimens with the vacuum specimens revealed that the nitrogen specimens have undergone light oxidation, assumed to be formed by residual oxygen molecules in the nitrogen gas. The resulting stress-strain curves confirm the assumption, as can be seen in Figure 7.13. However, only a minor decrease of the strain at break can be seen for the nitrogen specimen in comparison to the vacuum specimen. The increased UTS value for the nitrogen specimen cannot be explained based on the available information. These results show that the observed reduction of the strain at break and strain at UTS can be attributed to the oxidation of the surface, confirming Figure 7.6, which revealed that the minimum oxidation temperature set on is at max. 130 °C.

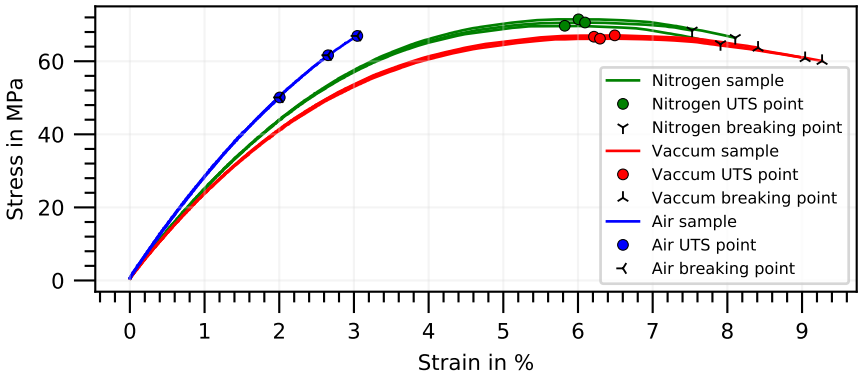

Figure 7.13: Comparison of the specimen after thermal exposure at different atmospheres after 72 h exposure time at 150 °C

7.4.3 Mechanical – FTIR data correlation

In Section 6, the peak shift observations have been used to describe the underlying physical processes during creep loading. As stated in Section 1.2, the main assumption is that the mechanical behavior is primarily driven by the material state represented by the molecular bonds and this material state can be determined using infrared spectroscopy. The results from Section 7.4.2 showing the impact of surface oxidation can be used to explain the reduced strain at break and strain at UTS values observed in Figure 7.12. At the same time, the results from the hydroxyl group analysis presented in Section 7.3.2 also indicate a

dehydration process which may reinforce the increase of brittleness. Next, the approach introduced in Section 6 to measure the intermolecular and intramolecular forces will be used to explain the UTS development of the thermally exposed specimens shown in Figure 7.12. Therefore, the peak shift analysis is performed for the spectral data acquired from the thermally exposed specimens. It is important to mention that in comparison to Section 6, all specimens are free of external loads during measurement and that the degradation lays time-wise in the past. The results of the peak-shift analysis can be seen in Figure 7.14, where on the left side, the PWN of the hydrogen peak indicates higher intermolecular forces with an increasing value, while on the right side, a decreasing PWN indicates higher intramolecular forces.

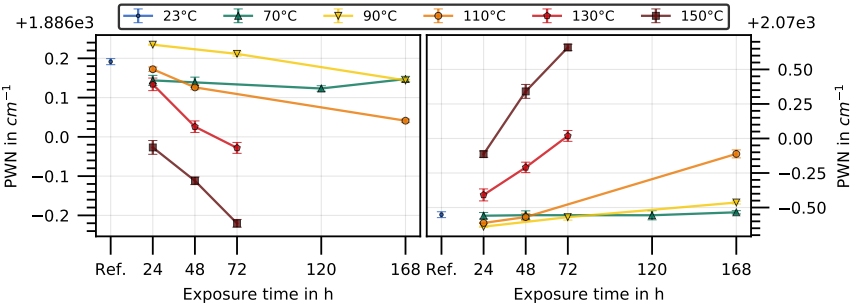

Figure 7.14: Peak wavenumber shifts of thermally degraded specimens in air atmosphere indicating intramolecular forces (left) and intermolecular forces (right)

Looking at the hydrogen PWN (Figure 7.14 left), the results indicate that, in general, with rising temperature and time, the free volume between the polymer chains increases while the intermolecular forces decrease. The thermal exposure at 70 °C (17.1 °C below Tg) is expected to lead to a reduction of the free volume. However, the hydrogen PWN value in Figure 7.14 left indicates an increase. Also, the initial decrease of the free volume for the 90 °C cannot be explained with the available data. Additional experiments performing thermal aging, as well as DSC measurements, have to be performed to explain this behavior in the future. Looking into ether PWN which is assumed to indicate the stress of ether bond and therefore, the polymeric backbone, with increasing exposure time and temperature, the stress is generally decreasing. This may be caused by an increase in chain scission events during thermal exposure. This observation could also explain the behavior of the 90 °C / 24 h specimens. It can be seen that the

backbone stress is slightly increased for this specimen. Increased intramolecular stress, on the other hand, may also influence intermolecular forces.

7.5 Thermal degradation for thick specimens

In the last sections, it was shown that the FTIR spectrum generally contains the information to describe a material state sufficient to predict material properties. Next, a machine learning-based approach will be used to create a numerical model to connect the NIR spectrum with the mechanical properties of the polymer after thermal degradation. The goal of this approach is to estimate the thermal degradation severity and predict the mechanical properties solely based on the FTIR spectrum. The section should be regarded as a proof of concept rather than an in-depth study due to the highly limited experimental configuration and small sample size. For the study, 1 mm thick dogbone specimens have been manufactured using the standard geometry and manufacturing approach. Due to the specimen thickness, the MIR is not available and the FTIR measurements were performed in the NIR. As explained in Section 3.2.2, the NIR spectra contain less information and the clear allocation of the single bands is more complicated. Therefore, deriving thermal degradation variables in the NIR spectra is not straightforward and the results from the previous sections cannot be simply transferred. However, it is assumed that the specimens show similar physical and chemical behavior, e.g., oxidation and the bulk material undergoes similar intramolecular and intermolecular changes as the thinner specimens. A clear variation of the spectrum after thermal exposure of the specimen cannot be seen by comparing the spectra alone. Rather, it is assumed that the spectral variation exists and can be unveiled using computational methods. On the one hand, lower information density in comparison to the MIR bands and a higher scatter of the data is observed and complicates the analysis. On the other hand, the benefits of using the NIR spectra are the high penetration depth (obtaining information for the bulk) and low-cost components. An indication of a change in the hydroxy group intensity can be observed at $5238\,\mathrm{cm}^{-1}$, though the overall intensity change does not allow for an easy regression approach, as shown in the MIR spectrum for the thermal degradation. As a result, the approach of further processing the data and extracting information regarding thermal degradation is motivated by these circumstances. Figure 7.15 shows two FTIR spectra in the NIR spectral range. The blue spectrum represents the bulk specimen after manufacturing, as previously introduced in Figure 7.6, while the red spectrum

was obtained after heat exposure. As for the MIR spectrum, the assignment of the spectral bands was also performed according to the literature (e.g., [40]).

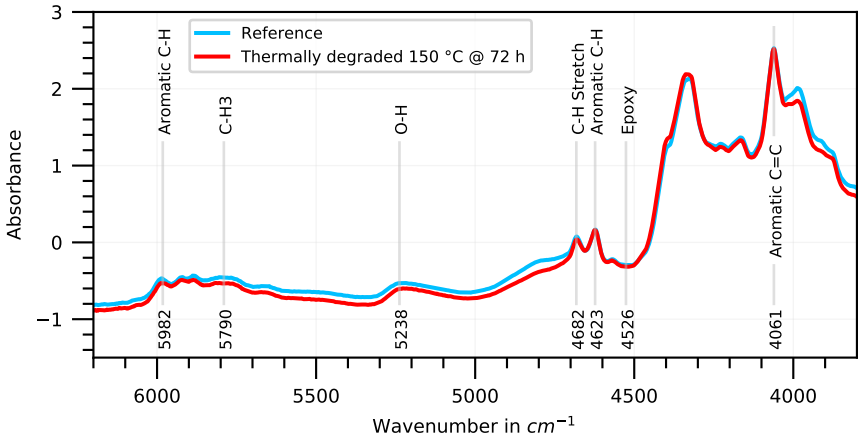

Figure 7.15: NIR spectra, comparison of reference and thermally degraded specimen

7.5.1 ANN Prediction Results

In the following section, the results of the ANN prediction are shown. The UTS, the temperature, and the exposure time can be predicted using FTIR spectroscopy and the ANN approach with high accuracy. Figure 7.16 shows that a clear correlation between the measured and predicted UTS could be established. The graphic shows the results for 60 data points of the validation set, while the training was performed on a dataset of 237 FTIR spectra. The measured UTS values have been calculated using a default specimen cross-section. While it was perceived after the study that the true cross-section was larger and an offset of approximately 20 MPa was introduced due to this inaccuracy leading to lower true UTS values, the validity of the results and the prediction approach are not affected. Even though the overall scatter for the UTS was high for the whole dataset, the prediction for the single specimens had high accuracy. A black line represents an accurate prediction where the measurement corresponds to the prediction. Actual predicted values were marked with blue dots. The vertical difference between the line and the dots represents the prediction error for every specimen. Two outliers, at 64 and 94 MPa, could be seen, showing the limits

of the model at its boundaries. The same approach to displaying the results is used for temperature and time prediction, see Figure 7.16.

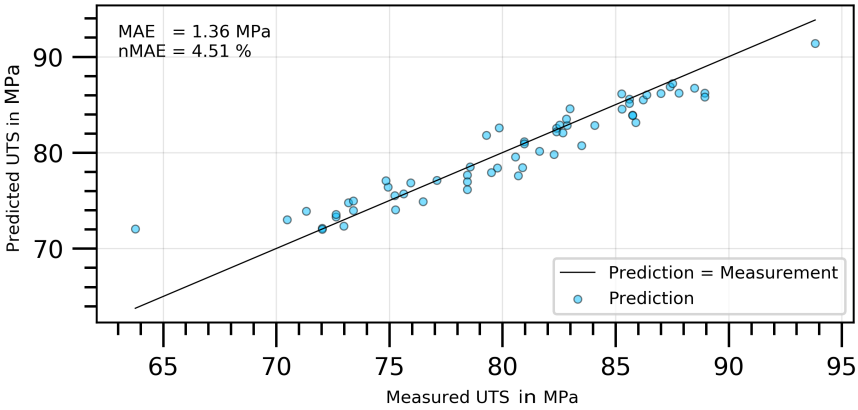

Figure 7.16: Prediction of mechanical properties using ANN - the measured and predicted UTS values

The results regarding temperature prediction showed good results normalized mean absolute error (nMAE) of 2.1 %, even though time and temperature are considered coupled in the literature. The scatter of the predicted time values is high, as short exposure times were used to show the limitations of the approach. Longer exposure times would significantly increase prediction accuracy in practice. In addition to the regression approach, classification was initially considered to predict the exposure time and temperature. Although the classification approach showed good results, it was not further considered since, in practice, a prediction of a concrete value after an unknown thermal exposure is desired.

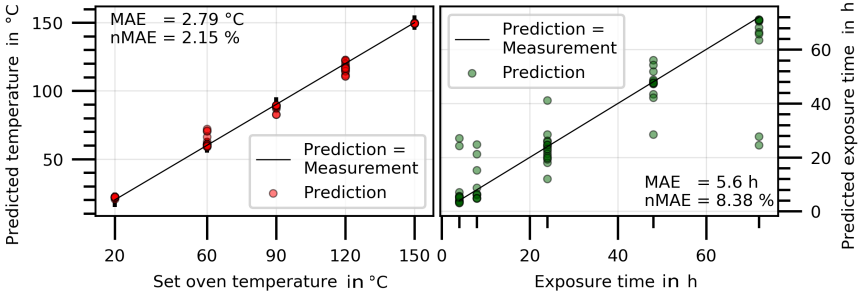

Figure 7.17: Prediction of mechanical properties using ANN - Time and Temperature prediction

As the Spectra in Figure 7.17 were already pre-processed, a comparison between the results of the ANN with and without any pre-processing steps is provided in Figure Figure 7.18. Therefore, the best prediction made for the raw spectra was compared to the prediction after pre-processing and feature extraction. The PP approach not only reduced the calculation time but also increased the accuracy of the achievable results significantly.

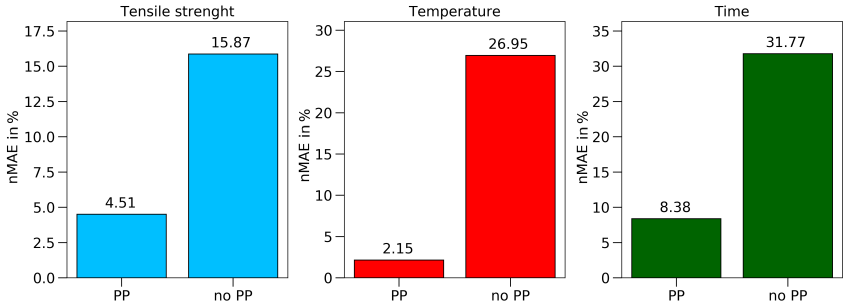

Figure 7.18: Prediction accuracy for the UTS, exposure temperature and time, along with the effect of pre-processing on ANN results

For the tensile strength, the prediction could be improved by 11 %; toward an nMAE of 4.51 %, which equals a mean absolute error of 1.35 MPa. The prediction of the set oven temperature reached an nMAE of 2.1 % and the predicted exposure time 8.3 %.

8 Summary and Conclusion

In this work, the feasibility of estimating the material state of a thermosetting polymer was evaluated using infrared spectroscopy and predictive analytics. Different external influence factors have been considered while establishing predictive models and quantifying residual mechanical properties.

As a result, it was shown that the molecular information acquired from the spectral infrared region contains suitable information to derive a material state vector describing inherent material properties. Under the assumption that sufficient data is available, it is possible to establish a direct link between the material state and residual material behavior for certain degradation factors.

Influence Factors during Manufacturing

The results of the mixing ratio evaluation show that for both epoxy systems, the determination of the mixing ratio is connected to a calibration task and that the accuracy of the model highly depends on the mixing components as well as the modeling approach. The results showed that the calibrated model could be used to predict the mix ratio. Clearly, the model accuracy can be improved if the SNR ratio is increased by optimizing the data acquisition parameters, especially by increasing the acquisition time and data binning. In general, a trade-off between effort and required accuracy has to be performed to define the correct approach.

Mechanical Degradation

A new approach to evaluating the physical processes on the molecular level was introduced by performing static, creep and cyclic mechanical experiments while recording spectroscopic data in situ. A model was proposed to explain the extensive plasticity observed in small epoxy specimens. The origin of the plasticity was found to be connected to different molecular changes occurring in tensile-loaded thin specimens. It was shown that using infrared spectroscopy and feature extraction, the intermolecular and intramolecular forces can be quantified. Applying Gaussian fitting on IR peaks yields a variable connected with the mean

molecular stress of the molecular bonds. After loading the molecular structure, a shift of the peak wavenumber value was found, which can be used to quantify the forces acting on the corresponding molecular bond. The first overtone of the ether bond was found to be useful in quantifying the intramolecular forces describing the stress of the polymeric backbone. Furthermore, the aromatic hydrogen bond also undergoes a peak wavenumber variation that was found to be connected with the intensity of intermolecular forces. As a result, a critical PWN could be defined, which indicates a point of instability, allowing the prediction of a critical material state for creep and fatigue loads.

Thermal Degradation

A quantitative analysis of thermal degradation and its spectral identification was performed. It was shown that thermal exposure leads to chain scission in the polymer bulk material, as well as oxidation of the surface under the presence of oxygen. While oxidation increases the brittleness of the epoxy resin by forming an oxide layer, specimens under vacuum condition do not show a variation in brittleness. However, a reduction of the UTS was shown to be directly connected with the exposure temperature and time. It was shown that this effect is based on the altered chemistry inside of the polymer and is caused by the chain scission process. Overall, a complex dependence between the molecular forces and degradation factors was found while the experimental setup did not allow a full resolution of the underlying influence effects. Further studies have to be conducted to evaluate the specimens after thermal exposure by the peak-shift approach. Furthermore, a novel method to predict and quantify the thermal degradation time, temperature, and residual strength of a polymer matrix using ANN and FTIR spectroscopy was presented in this study. The ANN approach is capable of predicting the residual strength of thermally degraded epoxy resin, as well as estimating the exposure time and temperature, with high accuracy. Applying a data reduction process significantly reduces the training time of the ANN and increases the accuracy of the predictions. The results also demonstrate that an average temperature deviation of about 6 % and an average deviation of 3 % for the strength prediction could be achieved using this approach.

Final Considerations

The presented work represents an initial study confirming the feasibility of deriving in-depth material properties from FTIR spectra. Nonetheless, with currently available devices, the method was only confirmed to work under strictly controlled lab environmental conditions but may evolve with the development of

customized FTIR spectrometers. The prediction of the properties is currently limited to the configuration used in this study, especially regarding the used specimen manufacturing methods, applied specimen geometry and material, as well as the used the FTIR spectrometer settings and model. In order to apply the method in practice, additional research has to be undertaken to extend the understanding. Nonetheless, the generalization of the approach represents a promising path toward a new non-destructive inspection method. In the next section (Section 9), a number of recommendations and ideas for future work are presented.

9 Outlook

This work presented the capabilities and the advantages of estimating the material state using advanced analytical methods based on FTIR spectroscopy data. Throughout the different sections and applications, several assumptions and limitations had to be applied to enable the methodology evaluation. For future applications, it is inevitable to further extend the knowledge of the impact and interaction of different influences on the reliability of the model. The ultimate goal shall remain in a holistic model capable of deriving all material properties solely based on spectral data. Advantages in technical capabilities and knowledge in three different areas have to be accomplished in order to achieve further progress.

Testing

First, the data acquisition in this work represented limited, highly focused datasets. An extension of the data acquisition process toward different specimen geometries and out-of-lab specimens or in-production parts would give access to a significantly higher sample size while covering additional, partly unknown influence factors. On the other hand, an increased and more representative sample size may also be achieved by applying a solid design of the experimental approach and mixing the single influence factors randomly. The unavailability of true stress and true strain values made it hard to evaluate local material properties in the analyzed zone. In the future, in situ combination of mechanical loading, IR measurements and digital image correlation or birefringence measurements could allow additional insight into local material processes. The extensions of the experimental setup toward compression and shear experiments could give a more complete picture of the deformation capabilities. In addition, using the-optical FTIR spectroscopy, chain orientation could be revealed, allowing a deeper insight into the molecular orientation processes occurring during mechanical loading.

Data Acquisition

Furthermore, the quantity and quality of FTIR data could be improved by increasing the spectral and spatial resolution. By reducing the scanned bandwidth to the important spectral bands, a faster data acquisition could be achieved while optimizing the spectrometer components to work in this area. A different approach to reducing signal noise and increasing spectral resolution may be accessible through additional progress in the application of quantum cascade lasers as IR light source. Focal plane array detectors, as currently used in FTIR microscopes, could give access to spatially resolved data while allowing real-time spectral scatter evaluation and in situ mapping of material properties. Even though the presented models were based on infrared spectral data, they may be extended to additional electromagnetic spectrum and acquisition methods such as Raman or VIS spectroscopy to overcome material absorbance and penetration depth limitations.

Model Improvements

In regard to the prediction of the material state and the corresponding mechanical properties and its evolution, the underlying effects could be further analyzed to understand the molecular processes. Therefore, extending the loading cycles while adding influence factors may represent an interesting research direction, especially if real-time data processing is performed. In this work, the assumption of a Gaussian distribution was made for spectroscopic data. By reevaluating this approach and the use of composite models (adding other distributions or functions) for peak modeling, the accuracy of the prediction may be improved while increasing the model complexity. In this work, the center position of the Gaussian fit was used as model input. However, the Gaussian fit also delivers the integral and the sigma value, which may be connected with additional material properties presumably representing the overall bond number and the distribution of the stress for the single molecular bonds.

Data Processing

As was shown in the last section, using ANN may lead to outstanding and unexpected results. The performance of ANN is extraordinary if unknown dependencies have to be found in huge datasets. They are, therefore, highly beneficial to narrow the research objectives and determine future research direction. However, these results may come with the downside of reduced interpretability and reliability. The models are governed and highly limited by the training data set and its containing influence factors. Therefore, to create a robust and reliable

model, the insights acquired by ANN should be transferred into knowledge and clear rules. In a second step, these rules should be used to implement classic data processing algorithms to process the data and avoid unexpected model behavior, e.g., by the emergence of new influence factors or unknown scatter sources.

Bibliography

[1] *Terms and definitions used on ageing of materials - Polymeric materials*. Norm. Sept. 2012.

[2] G. W. Ehrenstein and S. Pongratz. *Beständigkeit von Kunststoffen*. Hanser München, 2007.

[3] J. L. Koenig. *Spectroscopy of polymers*. Elsevier, 1999.

[4] L. Prado, G. Goerigk, M. L. Ponce, V. M. Garamus, H. Wittich, R. Willumeit, K. Schulte, and S. P. Nunes. "Characterization of proton-conducting organic–inorganic polymeric materials by ASAXS". In: *Journal of Polymer Science Part B: Polymer Physics* 43.21 (2005), pp. 2981–2992.

[5] V. Trappe, A. Müller, and S. Hickmann. "Infinite life of CFRP evaluated non-destructively with X-ray-refraction topography in-situ mechanical loading". In: (2016).

[6] X. M. Sui, M. Tiwari, I. Greenfeld, R. L. Khalfin, H. Meeuw, B. Fiedler, and H. D. Wagner. "Extreme scale-dependent tensile properties of epoxy fibers". In: *Express Polymer Letters* 13.11 (2019), p. 993.

[7] PRGDJ Graves and D. Gardiner. "Practical raman spectroscopy". In: *Springer* (1989).

[8] P. R. Griffiths and J. A. de Haseth. *Fourier transform infrared spectrometry*. Vol. 171. John Wiley & Sons, 2007.

[9] Divers. "FTIR Talk letters". In: *FTIR Talk letters* (2010-2019).

[10] E. Mertzel and J. L. Koenig. "Application of FT-IR and NMR to epoxy resins". In: *Epoxy Resins and Composites II*. Springer, 1986, pp. 73–112.

[11] C. Pasquini. "Near infrared spectroscopy: fundamentals, practical aspects and analytical applications". In: *Journal of the Brazilian chemical society* 14.2 (2003), pp. 198–219.

[12] R. Bhargava, S. Wang, and J. L. Koenig. “FTIR microspectroscopy of polymeric systems”. In: *Liquid Chromatography/FTIR Microspectroscopy/Microwave Assisted Synthesis*. Springer, 2003, pp. 137–191.

[13] R. Bhargava. “Infrared spectroscopic imaging: the next generation”. In: *Applied spectroscopy* 66.10 (2012), pp. 1091–1120.

[14] Y. Ozaki, A. Ikehata, and H. Shinzawa. “Near-infrared spectroscopy in biological molecules and tissues”. In: *Encyclopedia of Biophysics, GCK Roberts (ed.), Springer-Verlag, Berlin, Heidelberg* (2013), pp. 1695–1706.

[15] S. Tiwari and R. Bhargava. “Extracting knowledge from chemical imaging data using computational algorithms for digital cancer diagnosis”. In: *The Yale journal of biology and medicine* 88.2 (2015), pp. 131–143.

[16] M. J. Baker, J. Trevisan, P. Bassan, R. Bhargava, H. J. Butler, K. M. Dorling, P. R. Fielden, S. W. Fogarty, N. J. Fullwood, K. A. Heys, et al. “Using Fourier transform IR spectroscopy to analyze biological materials”. In: *Nature protocols* 9.8 (2014), p. 1771.

[17] W. Schmidt. *Optische Spektroskopie: Eine Einführung*. John Wiley & Sons, 2014.

[18] E. Dümichen, M. Javdanitehran, M. Erdmann, V. Trappe, H. Sturm, U. Braun, and G. Ziegmann. “Analyzing the network formation and curing kinetics of epoxy resins by in situ near-infrared measurements with variable heating rates”. In: *Thermochimica acta* 616 (2015), pp. 49–60.

[19] G. W. Ehrenstein, G. Riedel, and P. Trawiel. *Thermal analysis of plastics: theory and practice*. Carl Hanser Verlag GmbH Co KG, 2012.

[20] L. Monney, N. Rouge, C. Dubois, and A. Chambaudet. “Photo-chemical degradation study of an epoxy material by X-ray analysis”. In: *Polymer degradation and stability* (1998). ISSN: 01413910. DOI: 10.1016/S0141-3910(98)00023-8.

[21] M. Hesse, H. Meier, and B. Zeeh. *Spektroskopische Methoden in der organischen Chemie*. Georg Thieme Verlag, 2005.

[22] M. G. González, J. C. Cabanelas, and J. Baselga. “Applications of FTIR on epoxy resins-identification, monitoring the curing process, phase separation and water uptake”. In: *Infrared Spectroscopy-Materials Science, Engineering and Technology*. InTech, 2012.

[23] G. van Rossum and F. L. Drake. *Python 3 Reference Manual*. Scotts Valley, CA: CreateSpace, 2009. ISBN: 1441412697.

[24] F. Pérez and B. E. Granger. "IPython: a System for Interactive Scientific Computing". In: *Computing in Science and Engineering* 9.3 (2007), pp. 21–29. ISSN: 1521-9615. DOI: 10.1109/MCSE.2007.53. URL: https://ipython.org.

[25] S. van der Walt, S. C. Colbert, and G. Varoquaux. "The NumPy Array: A Structure for Efficient Numerical Computation". In: *Computing in Science Engineering* 13.2 (2011), pp. 22–30.

[26] P. Virtanen, R. Gommers, Oliphant T. E., M. Haberland, T. Reddy, D. Cournapeau, E. Burovski, P. Peterson, W. Weckesser, J. Bright, van der Walt S. J., M. Brett, J. Wilson, K. J. Millman, N. Mayorov, A. R. J. Nelson, E. Jones, R. Kern, E. Larson, C. J. Carey, Polat, Feng, Yu, Moore E. W., J. Vand erPlas, D. Laxalde, J. Perktold, R. Cimrman, I. Henriksen, E. A. Quintero, C. R. Harris, A. M. Archibald, A. H. Ribeiro, F. Pedregosa, P. van Mulbregt, and SciPy 1. 0. Contributors. "SciPy 1.0: Fundamental Algorithms for Scientific Computing in Python". In: *Nature Methods* 17 (2020), pp. 261–272. DOI: 10.1038/s41592-019-0686-2.

[27] J. D. Hunter. "Matplotlib: A 2D Graphics Environment". In: *Computing in Science Engineering* 9.3 (2007), pp. 90–95.

[28] F. Pedregosa, G. Varoquaux, A. Gramfort, V. Michel, B. Thirion, O. Grisel, M. Blondel, P. Prettenhofer, R. Weiss, V. Dubourg, J. Vanderplas, A. Passos, D. Cournapeau, M. Brucher, M. Perrot, and E. Duchesnay. "Scikit-Learn: Machine Learning in Python". In: *J. Mach. Learn. Res.* 12.null (Nov. 2011), pp. 2825–2830. ISSN: 1532-4435.

[29] The pandas development team. *pandas-dev/pandas: Pandas*. 2020. DOI: 10.5281/zenodo.3509134.

[30] A. Savitzky and M. J. E. Golay. "Smoothing and differentiation of data by simplified least squares procedures". In: *Analytical chemistry* 36.8 (1964), pp. 1627–1639.

[31] M. Newville, T. Stensitzki, D. B. Allen, M. Rawlik, A. Ingargiola, and A. Nelson. "LMFIT: Non-linear least-square minimization and curve-fitting for Python". In: *Astrophysics Source Code Library* (2016).

[32] K. Danzer, H. Hobert, C. Fischbacher, and K-U Jagemann. *Chemometrik: Grundlagen und Anwendungen*. Springer-Verlag, 2013.

[33] A. Géron. *Hands-On Machine Learning with Scikit-Learn, Keras, and TensorFlow: Concepts, Tools, and Techniques to Build Intelligent Systems*. O'Reilly Media, 2019.

[34] C. Kozyrkov. ""The simplest explanation of machine learning you'll ever read". In: *url: https://hackernoon. com/the-simplest-explanation-ofmachine-learning-youll-ever-read-bebc0700047c (visited on 2019-03-03)* (2018).

[35] C. M. Bishop et al. *Neural networks for pattern recognition*. Oxford university press, 1995.

[36] H. Schürmann. *Konstruieren mit Faser-Kunststoff-Verbunden*. Vol. 2. Springer, 2005.

[37] W. Grellmann and B. Langer. *Deformation and fracture behaviour of polymer materials*. Springer, 2017.

[38] H. H. Kausch-Blecken von Schmeling and J. G. Williams. "Polymer fracture". In: *Encyclopedia of Polymer Science and Technology* (2002), pp. 1–65.

[39] Audrius Doblies, Christian Feiler, Tim Würger, Eduard Schill, Robert H Meißner, and Bodo Fiedler. "Mechanical degradation estimation of thermosets by peak shift assessment: General approach using infrared spectroscopy". In: *Polymer* 221 (2021), p. 123585.

[40] C. G'sell and J. J. Jonas. "Yield and transient effects during the plastic deformation of solid polymers". In: *Journal of materials science* 16.7 (1981), pp. 1956–1974.

[41] A. J. Kinloch. *Fracture behaviour of polymers*. Springer Science & Business Media, 2013.

[42] G. H. Michler and F. J. Baltá-Calleja. *Nano-and micromechanics of polymers: structure modification and improvement of properties*. Carl Hanser Verlag GmbH Co KG, 2012.

[43] H. R. Brown. "A model for brittle-ductile transitions in polymers". In: *Journal of materials science* 17.2 (1982), pp. 469–476.

[44] Ch G'sell and J. J. Jonas. "Determination of the plastic behaviour of solid polymers at constant true strain rate". In: *Journal of materials science* 14.3 (1979), pp. 583–591.

[45] B. Fiedler, M. Hojo, S. Ochiai, K. Schulte, and M. Ando. "Failure behavior of an epoxy matrix under different kinds of static loading". In: *Composites science and technology* 61.11 (2001), pp. 1615–1624.

[46] O. Sindt, J. Perez, and J. F. Gerard. "Molecular architecture-mechanical behaviour relationships in epoxy networks". In: *Polymer* 37.14 (1996), pp. 2989–2997.

[47] O. A. Hasan and M. C. Boyce. "A constitutive model for the nonlinear viscoelastic viscoplastic behavior of glassy polymers". In: *Polymer Engineering & Science* 35.4 (1995), pp. 331–344.

[48] L. C. E. Struik. "Some problems in the non-linear viscoelasticity of amorphous glassy polymers". In: *Journal of Non-Crystalline Solids* 131 (1991), pp. 395–407.

[49] A. A. Griffith and John J. Gilman. "The phenomena of rupture and flow in solids". In: *Transactions of the ASM* 61 (1968), pp. 855–906.

[50] E. O. Hall. "The deformation and ageing of mild steel: III discussion of results". In: *Proceedings of the Physical Society. Section B* 64.9 (1951), p. 747.

[51] G. I. Barenblatt et al. "The mathematical theory of equilibrium cracks in brittle fracture". In: *Advances in applied mechanics* 7.1 (1962), pp. 55–129.

[52] I. M. Ward. *Structure and properties of oriented polymers*. Springer Science & Business Media, 2012.

[53] H. D. Wagner. "Stochastic concepts in the study of size effects in the mechanical strength of highly oriented polymeric materials". In: *Journal of Polymer Science Part B: Polymer Physics* 27.1 (1989), pp. 115–149.

[54] E. M. Odom and D. F. Adams. "Specimen size effect during tensile testing of an unreinforced polymer". In: *Journal of materials science* 27.7 (1992), pp. 1767–1771.

[55] C. Leopold, T. Augustin, T. Schwebler, J. Lehmann, W. V. Liebig, and B. Fiedler. "Influence of carbon nanoparticle modification on the mechanical and electrical properties of epoxy in small volumes". In: *Journal of colloid and interface science* 506 (2017), pp. 620–632.

[56] C. Leopold, W. V. Liebig, H. Wittich, and B. Fiedler. “Size effect of graphene nanoparticle modified epoxy matrix”. In: *Composites science and technology* 134 (2016), pp. 217–225.

[57] C. Hopmann and J. Marder. “Investigation of the fatigue behaviour of carbon fibre reinforced plastics due to micro-damage and effects of the micro-damage on the ply strengths in the very high cycle fatigue regime”. In: *Fatigue of Materials at Very High Numbers of Loading Cycles*. Springer, 2018, pp. 561–583.

[58] T. Hobbiebrunken, M. Hojo, T. Adachi, C. de Jong, and B. Fiedler. “Evaluation of interfacial strength in CF/epoxies using FEM and in-situ experiments”. In: *Composites Part A: Applied Science and Manufacturing* 37.12 (2006), pp. 2248–2256.

[59] L. C. E. Struik. “Physical aging in plastics and other glassy materials”. In: *Polymer Engineering & Science* 17.3 (1977), pp. 165–173.

[60] C. A. Angell, K. L. Ngai, G. B. McKenna, P. F. McMillan, and S. W. Martin. “Relaxation in glassforming liquids and amorphous solids”. In: *Journal of applied physics* 88.6 (2000), pp. 3113–3157.

[61] I. M. Hodge. “Enthalpy relaxation and recovery in amorphous materials”. In: *Journal of Non-Crystalline Solids* 169.3 (1994), pp. 211–266.

[62] S. Wu. “Control of intrinsic brittleness and toughness of polymers and blends by chemical structure: a review”. In: *Polymer international* 29.3 (1992), pp. 229–247.

[63] G. M. Odegard and A. Bandyopadhyay. “Physical aging of epoxy polymers and their composites”. In: *Journal of Polymer Science Part B: Polymer Physics* 49.24 (2011), pp. 1695–1716.

[64] J. M. Barton. “The application of differential scanning calorimetry (DSC) to the study of epoxy resin curing reactions”. In: *Epoxy resins and composites I*. Springer, 1985, pp. 111–154.

[65] D. K. Roylance and K. L. DeVries. “Determination of atomic stress distribution in oriented polypropylene by infrared spectroscopy”. In: *Journal of Polymer Science Part B: Polymer Letters* 9.6 (1971), pp. 443–447.

[66] V. I. Vettegren and Novak. “Determination of atomic stress distribution in stressed polymers by infrared spectroscopy”. In: *Journal of Polymer Science: Polymer Physics Edition* 11.11 (1973), pp. 2135–2142.

[67] V. I. Vettegren, Novak, and K. J. Friedland. “Overstressed interatomic bonds in stressed polymers”. In: *International Journal of Fracture* 11.5 (1975), pp. 789–801.

[68] R. P. Wool. “Mechanisms of frequency shifting in the infrared spectrum of stressed polymer”. In: *Journal of Polymer Science: Polymer Physics Edition* 13.9 (1975), pp. 1795–1808.

[69] R. S. Bretzlaff and R. P. Wool. “Frequency shifting and asymmetry in infrared bands of stressed polymers”. In: *Macromolecules* 16.12 (1983), pp. 1907–1917.

[70] J. T. Seitz. “The estimation of mechanical properties of polymers from molecular structure”. In: *Journal of Applied Polymer Science* 49.8 (1993), pp. 1331–1351. ISSN: 10974628.

[71] S. N. Zhurkov. “Kinetic concept of the strength of solids”. In: *International Journal of Fracture* 26.4 (1984), pp. 295–307.

[72] D. W. Ovenall. “Electron spin resonance of free radicals in epoxide resins”. In: *Journal of Polymer Science Part B: Polymer Letters* 1.1 (1963), pp. 37–40.

[73] M. Sakaguchi and J. Sohma. “ESR evidence for main-chain scission produced by mechanical fracture of polymers at low temperature”. In: *Journal of Polymer Science: Polymer Physics Edition* 13.6 (1975), pp. 1233–1245.

[74] S. Schlick. *Advanced ESR methods in polymer research*. John Wiley & Sons, 2006.

[75] Ferraro, S. S. Mitra, and C. Postmus. “The far infrared spectra of solids under high pressure (33–100 \mu)”. In: *Inorganic and Nuclear Chemistry Letters* 2.9 (1966), pp. 269–275.

[76] V. B. Kulik et al. “Quantum vibration dynamics and deformation of skeleton of polymer molecules”. In: *Polymer Science Series A* 51.8 (2009), pp. 849–857.

[77] L. Salmén and E. Bergström. “Cellulose structural arrangement in relation to spectral changes in tensile loading FTIR”. In: *Cellulose* 16.6 (2009), pp. 975–982.

[78] M. S. Sammon, M. Ončák, and M. K. Beyer. “Theoretical simulation of the infrared signature of mechanically stressed polymer solids”. In: *Beilstein journal of organic chemistry* 13.1 (2017), pp. 1710–1716.

[79] A. Doblies, B. Boll, and B. Fiedler. “Prediction of thermal exposure and mechanical behavior of epoxy resin using artificial neural networks and Fourier transform infrared spectroscopy”. In: *Polymers* 11.2 (2019), p. 363.

[80] H. Shinzawa and J. Mizukado. “Rheo-optical two-dimensional (2D) near-infrared (NIR) correlation spectroscopy for probing strain-induced molecular chain deformation of annealed and quenched Nylon 6 films”. In: *Journal of Molecular Structure* 1158 (2018), pp. 271–276.

[81] R. D.B. Fraser. “The interpretation of infrared dichroism in fibrous protein structures”. In: *The Journal of Chemical Physics* 21.9 (1953), pp. 1511–1515.

[82] T. Buffeteau and M. Pézolet. “Linear Dichroism in Infrared Spectroscopy”. In: *Handbook of Vibrational Spectroscopy* (2006).

[83] K. Holland-Moritz, I. Holland-Moritz, and K. van Werden. “Application of FTIR-spectroscopy on orientation processes in polyethylene films”. In: *Colloid and Polymer Science* 259.2 (1981), pp. 156–162.

[84] I. Noda, A. E. Dowrey, and C. Marcott. “Dynamic infrared linear dichroism of polymer films under oscillatory deformation”. In: *Journal of Polymer Science: Polymer Letters Edition* 21.2 (1983), pp. 99–103.

[85] H. W. Siesler. “Rheo-optical Fourier-transform infrared (FTIR) spectroscopy of polymers”. In: *Colloid and Polymer Science* 262.3 (1984), pp. 223–229.

[86] H. W. Siesler. “Rheo-optical Fourier transform infrared spectroscopy of polymers. 10: Strain-induced crystallization of sulfur-crosslinked natural rubber during cyclic deformation”. In: *Applied spectroscopy* 39.5 (1985), pp. 761–765.

[87] S. Lanceros-Mendez, J. F. Mano, Am Costa, and V. Hugo Schmidt. “FTIR and DSC studies of mechanically deformed \beta-PVDF films”. In: *Journal of Macromolecular Science, Part B* 40.3-4 (2001), pp. 517–527.

[88] T. Scherzer. “Molecular orientation phenomena in DGEBA/polyetherdiamine epoxies studied by rheo-optical FTIR spectroscopy”. In: *Polymer Bulletin* 35.5 (1995), pp. 621–628.

[89] T. Scherzer. “Characterization of the molecular deformation behavior of glassy epoxy resins by rheo-optical FTIR spectroscopy”. In: *Journal of Polymer Science Part B: Polymer Physics* 34.3 (1996), pp. 459–470.

[90] T. Scherzer. “FTi. r.—rheo-optical characterization of the molecular orientation behaviour of amine cured epoxy resins during cyclic deformation”. In: *Polymer* 37.26 (1996), pp. 5807–5816.

[91] Y. Kataoka and T. Kondo. “FT-IR microscopic analysis of changing cellulose crystalline structure during wood cell wall formation”. In: *Macromolecules* 31.3 (1998), pp. 760–764.

[92] R. Martin. *Ageing of Composites*. Woodhead Publishing Series in Composites Science and Engineering. Elsevier Science, 2008. ISBN: 9781845694937. URL: `https://books.google.de/books?id=W6ijAgAAQBAJ`.

[93] M. C. Celina. “Review of polymer oxidation and its relationship with materials performance and lifetime prediction”. In: *Polymer degradation and stability* 98.12 (2013), pp. 2419–2429. ISSN: 01413910.

[94] Y. Yang, G. Xian, H. Li, and L. Sui. “Thermal aging of an anhydride-cured epoxy resin”. In: *Polymer degradation and stability* 118 (2015), pp. 111–119. ISSN: 01413910.

[95] B. Mailhot, S. Morlat-Thérias, P. Bussière, and J. Gardette. “Study of the degradation of an epoxy/amine resin, 2”. In: *Macromolecular Chemistry and Physics* 206.5 (2005), pp. 585–591.

[96] S. Wiebel. “Untersuchung zur thermischen Langzeitstabilität von Epoxidharzen der elektrischen Isoliertechnik in Abhängigkeit von oxidativen Umgebungseinflüssen”. PhD thesis. Technische Universität, 2012.

[97] A. Krauklis and A. Echtermeyer. “Mechanism of yellowing: Carbonyl formation during hygrothermal aging in a common amine epoxy”. In: *Polymers* 10.9 (2018), p. 1017.

[98] *Technical data sheet - EPIKOTE resin MGS RIMR 135 and EPIKURE curing agent MGS RIMH*. 2006.

[99] J. K. Gillham, C. A. Glandt, and C. A. McPherson. “Chemistry and properties of crosslinked polymers”. In: *Labana, SS, Ed* (1977).

[100] M. J. Adamson. “Thermal expansion and swelling of cured epoxy resin used in graphite/epoxy composite materials”. In: *Journal of materials science* 15.7 (1980), pp. 1736–1745.

[101] L. W. Jelinski, J. J. Dumais, R. E. Stark, T. S. Ellis, and F. E. Karasz. “Interaction of epoxy resins with water. A quadrupole echo deuterium NMR study”. In: *Macromolecules* 16.6 (1983), pp. 1019–1021.

[102] J. Zhou and J. P. Lucas. “Hygrothermal effects of epoxy resin. Part I: the nature of water in epoxy”. In: *Polymer* 40.20 (1999), pp. 5505–5512.

[103] IBCM Rocha, S. Raijmaekers, R. P.L. Nijssen, F. P. van der Meer, and L. J. Sluys. “Hygrothermal ageing behaviour of a glass/epoxy composite used in wind turbine blades”. In: *Composite Structures* 174 (2017), pp. 110–122.

[104] Peiyi Wu and H. W. Siesler. “Water diffusion into epoxy resin: a 2D correlation ATR-FTIR investigation”. In: *Chemical physics letters* 374.1-2 (2003), pp. 74–78.

[105] A. E. Krauklis, A. I. Gagani, and A. T. Echtermeyer. “Near-infrared spectroscopic method for monitoring water content in epoxy resins and fiber-reinforced composites”. In: *Materials* 11.4 (2018), p. 586.

[106] B. Hinterstoisser and L. Salmén. “Application of dynamic 2D FTIR to cellulose”. In: *Vibrational Spectroscopy* (2000). ISSN: 09242031. DOI: 10.1016/S0924-2031(99)00063-6.

[107] C. J. Janke, E. A. Wachter, H. E. Philpot, and G. L. Powell. *Composite heat damage assessment*. 1993.

[108] A. Rein. *Advanced Fourier Transform Infrared Spectroscopy for Analyzing Damage in Aircraft Composites*. 2014.

[109] S. Eibl. “Comparison of surface and bulk analytical techniques for the distinct quantification of a moderate thermal pre-load on a carbon fibre reinforced plastic material”. In: *Polymer degradation and stability* 135 (2017), pp. 31–42. ISSN: 01413910.

[110] A. Rivaton, L. Moreau, and J. Gardette. “Photo-oxidation of phenoxy resins at long and short wavelengths—I. Identification of the photoproducts”. In: *Polymer degradation and stability* 58.3 (1997), pp. 321–332. ISSN: 01413910.

[111] V. Bellenger and J. Verdu. “Oxidative skeleton breaking in epoxy–amine networks”. In: *Journal of Applied Polymer Science* 30.1 (1985), pp. 363–374. ISSN: 10974628.